

# Cement and Concrete Composites

## Influence of sugar beetroot microsheets on the hydration kinetics of cementitious composites: Electrochemical characterization

--Manuscript Draft--

<b>Manuscript Number:</b>	CCC-D-22-01467R3
<b>Article Type:</b>	Research Paper
<b>Keywords:</b>	Cementitious Composites; sugar beetroot; microsheets; Degree of hydration; cyclic voltammetry; Electrochemical impedance spectroscopy
<b>Corresponding Author:</b>	Bo Huang, Ph.D Hunan University of Science and Technology Xiangtan, Hunan CHINA
<b>First Author:</b>	Bo Huang, Ph.D
<b>Order of Authors:</b>	Bo Huang, Ph.D Yin Chi, Ph.D Thamer Almotlaq Jianqun Wang, Ph.D Mohamed Saafi, Ph.D Junjie Ye, Ph.D Junbo Sun, Ph.D Yufei Wang Jianqiao Ye, Ph.D
<b>Abstract:</b>	<p>This paper examines the influence of novel sugar beetroot-based micro sheets (SMSs) on the hydration of cement. The SMS material was added to cement pastes in different concentrations and the hydration kinetics of the cementitious composites were studied via cyclic voltammetry (CV) and electrochemical impedance spectroscopy (EIS). The effect of SMS on the hydration development of cement, change in the pore size distribution and microstructural evolution were also quantified. The CV and EIS results revealed that the synergetic effect of the reactive SMS surface functional groups and tricalcium silicate (C3S) increased the ionic strength of the pore solution, ion diffusion rate and charge transport properties within the cementitious pastes. The CV and EIS measurements correlated well with the two main indicators of the cement hydration rate: the degree of hydration (DOH) and the calcium hydroxide (Ca(OH)<sub>2</sub>) content. The delineated hydration kinetics suggested that the SMS sheets accelerate the dissolution of C3S and increase the hydration depth by channelling water from the pore solution to the unhydrated cement core thereby amplifying the growth of the hydration phases. As a result, the mechanical properties of the SMS doped cementitious composites were improved. The proposed SMS sheets are a potential sustainable and renewable biomaterial for improving the performance and reducing the carbon footprint of cementitious materials.</p>
<b>Suggested Reviewers:</b>	<p>Shangtong Yang Senior Lecturer, University of Strathclyde shangtong.yang@strath.ac.uk Shangtong Yang research interest is focused on the understanding of basic principles that control the mechanical properties and behaviours of civil engineering materials, in particular, rock-like materials such as concrete and rock. Under a variety/combination of loads and environments, the mechanical response of these materials is still a challenging topic. I look at the fundamental questions in developing rational constitutive models and the engineering applications to creating novel solution and technology.</p> <p>Hailong Ye Assistant Professor, The University of Hong Kong hlye@hku.hk Dr. Hailong Ye is an Assistant Professor in the Department of Civil Engineering at The</p>

	<p>University of Hong Kong. He received his Ph.D. (2016) in Construction Materials from The Pennsylvania State University, USA. He worked as a Marie Curie Fellow at The University of Sheffield for a few months, before joining The University of Hong Kong in 2018. He is a Licensed Structural Engineer in China and a member of RILEM, American Concrete Institute (ACI), and American Ceramic Society (ACerS). He serves as an Associate Editor of ASCE's Journal of Materials in Civil Engineering. Dr. Ye's research interest includes Low-Carbon Cement Chemistry, Geopolymer and Alkali-Activated Concrete, Microbially Induced Concrete Corrosion (MICC), and Corrosion of Marine Concrete Structures. His research has been recognized by the 2020 Natural Science Award from the Ministry of Education of China.</p>
	<p>Rui Yu  Professor, Wuhan University of Technology  r.yu@whut.edu.cn  Rui Yu main research areas are as follows  1. Ultra-high performance fiber-reinforced composites  2. Marine functional building materials  3. Nano functional building materials  4. Construction waste recycled materials and ecological building materials</p>
	<p>Jianping Zhu  Professor, Henan Polytechnic University  jianpingzhu@hpu.edu.cn  Jianping Zhu has been engaged in the research of cement-based materials for a long time, especially in the research of solid waste resource utilization, nano-modified cement-based materials, particle size control cement-based materials, and concrete durability.</p>
	<p>Qingliang Yu  Associate professor, Eindhoven University of Technology  q.yu.1@tue.nl  Qingliang Yu research interests primarily concern cement-bound materials, from materials to structural behavior understanding, covering micro-, meso- and macro-level. His current research topics include functional building materials with air purifying, self-cleaning, or (ultra)high performance, concerning sustainability including alternative binders design like alkali-activated binder and application of industrial by-products or waste materials and durability under different exposure environment. His research follows the complete chain of knowledge from materials at molecular level to structural element, applying both experimental and modelling approaches. The current portfolio is well supported by his unique educational background from Civil Engineering to Materials Science.</p>
<p><b>Response to Reviewers:</b></p>	<p>Dear Reviewer's,  Thanks for your kind guide and time for the evaluation.  We have made corrections in accordance with the comments. Please refer to the Response to Reviewers document for details of the corrections.  Kind regards,  Bo Huang</p>

## Responses to reviewers' comments

**Journal:** Cement and Concrete Composites

**Manuscript number:** CCC-D-22-01467R2

**Title:** Influence of sugar beetroot microsheets on the hydration kinetics of cementitious composites: Electrochemical characterization

**Authors:** Bo Huang, Yin Chi, Thamer Almotlaq, Jianqun Wang, Mohamed Saafi, Junjie Ye, Junbo Sun, Yufei Wang, Jianqiao Ye

The authors would like to thank the reviewers for their valuable comments and editorial suggestions again. All the comments have been addressed in the revised manuscript. A detailed list of the point-by-point responses to the comments is given below. The basic format follows the sequence: Comments, Reply and Corrections. The revised text is highlighted in blue for easy identification.

### Responses to Reviewer #1

No.	Comments, Reply and Corrections	
1.	Comments	<i>All my comments were well addressed.</i>
	Reply	The authors would like to thank the reviewer for the positive comments and useful suggestions again.
	Corrections	No specific changes were made in the text.

### Responses to Reviewer #2

No.	Comments, Reply and Corrections	
1.	Comments	<p><i>1. Fig. 16 also indicates that the peak intensity of calcium carbonate decreased with increasing SMS dosage. The increase in the peak intensities is an indication of increased amount of the hydration phases resulting from the addition of SMS [69]. This is reflected in the increase of the mechanical properties of the cementitious composites containing SMS.</i></p> <p><i>I looked at Fig. 16 and could not quite decipher where the CaCO<sub>3</sub> decreased with the dosage. But in any case, the sentence that follows the "decrease" in the above excerpt is basically saying that since CaCO<sub>3</sub> decreased, we should be expecting a reduced amount of hydration phases and a degradation of the mechanical properties, i.e., contradicting the whole premise. Can you please respond to me here and clarify this point?</i></p>
	Reply	We thank the reviewer for highlighting the inconsistency of the discussion of the XRD results in Fig. 16. The "decrease" in the above sentence was a typo. We deleted the line that contains "decrease" in the section 3.8.2.
	Corrections	In the revised manuscript section 3.8.2, the sentence "Fig. 16 also indicates that the peak intensity of calcium carbonate decreased with increasing SMS dosage. The increase in the peak intensities is an indication of increased amount of the hydration phases resulting from the addition of SMS [69]. This is reflected in the increase of the mechanical properties of the cementitious composites containing SMS" This is now rewritten as: "The increase in the peak intensities is an indication of increased amount of the hydration phases

		resulting from the addition of SMS [71]. This is reflected in the increase of the mechanical properties of the cementitious composites containing SMS.”
2.	Comments	2. Also, in comment 6, you state: <i>This can be attributed to the large surface area of the SMS sheets which is decorated with many hydrophilic functional groups.</i>  <i>You probably may mean enhanced, but not "decorated"?</i>
	Reply	We thank the reviewer for the comment. The authors meant the SMS sheets contain many hydrophilic functional groups. As such, “This can be attributed to the large surface area of the SMS sheets which is decorated with many hydrophilic functional groups” is now rewritten as: This can be attributed to the hydrophilic functional groups on the surfaces of SMS.
	Corrections	"This can be attributed to the large surface area of the SMS sheets which is decorated with many hydrophilic functional groups." This now reads as: “This can be attributed to the hydrophilic functional groups on the surfaces of SMS.”.

## **Influence of sugar beetroot microsheets on the hydration kinetics of cementitious composites: Electrochemical characterization**

Bo Huang<sup>a,c</sup>, Yin Chi<sup>b\*</sup>, Thamer Almotlaq<sup>c,d</sup>, Jianqun Wang<sup>a</sup>, Mohamed Saafi<sup>c\*</sup>, Junjie Ye<sup>e</sup>, Junbo Sun<sup>f</sup>, Yufei Wang<sup>g</sup>, Jianqiao Ye<sup>c</sup>

<sup>a</sup>School of Civil Engineering, Hunan University of Science and Technology, Xiangtan, 411201, China

<sup>b</sup>School of Civil Engineering, Wuhan University, 430072, China

<sup>c</sup>School of Engineering, Lancaster University, Lancaster, LA1 4YR, UK

<sup>d</sup>Civil Engineering department, College of Engineering, Jouf University, Sakaka 72388, Saudi Arabia.

<sup>e</sup>Research Center for Applied Mechanics, Key Laboratory of Ministry of Education for Electronic Equipment Structure Design, Xidian University, Xi'an 710071, China

<sup>f</sup>Institute for Smart City of Chongqing University In Liyang, Chongqing University, Jiangsu, 213300, China

<sup>g</sup>School of Design and the Built Environment, Curtin University, Perth, WA, 6102, Australia

### **Abstract**

This paper examines the influence of novel sugar beetroot-based micro sheets (SMSs) on the hydration of cement. The SMS material was added to cement pastes in different concentrations and the hydration kinetics of the cementitious composites were studied via cyclic voltammetry (CV) and electrochemical impedance spectroscopy (EIS). The effect of SMS on the hydration development of cement, change in the pore size distribution and microstructural evolution were also quantified. The CV and EIS results revealed that the synergetic effect of the reactive SMS surface functional groups and tricalcium silicate (C<sub>3</sub>S) increased the ionic strength of the pore solution, ion diffusion rate and charge transport properties within the cementitious pastes. The CV and EIS measurements correlated well with the two main indicators of the cement hydration rate: the degree of hydration (DOH) and the calcium hydroxide (Ca(OH)<sub>2</sub>) content. The delineated hydration kinetics suggested that the SMS sheets accelerate the dissolution of C<sub>3</sub>S and increase the

---

\* Corresponding author. E-mail address. [m.saafi@lancaster.ac.uk](mailto:m.saafi@lancaster.ac.uk) (Mohamed Saafi)

[yin.chi@whu.edu.cn](mailto:yin.chi@whu.edu.cn) (Yin Chi)

hydration depth by channelling water from the pore solution to the unhydrated cement core thereby amplifying the growth of the hydration phases. As a result, the mechanical properties of the SMS doped cementitious composites were improved. The proposed SMS sheets are a potential sustainable and renewable biomaterial for improving the performance and reducing the carbon footprint of cementitious materials.

**Keywords:** Cementitious composites, sugar beetroot, microsheets, degree of hydration, cyclic voltammetry, electrochemical impedance spectroscopy.

## 1. Introduction

The consumption of ordinary Portland cement (OPC)-based materials is increasing at a rapid pace to meet an ever-grown demand for concrete infrastructure systems. This is of great concern as the production OPC leads to CO<sub>2</sub> emissions which is about 8% of the global CO<sub>2</sub> emissions. One potential way to lower the environmental impacts of cement is to improve the performance and the longevity of cement-based materials [1–6], as early removal and replacement of concrete infrastructure systems from service with new concrete infrastructure systems increases CO<sub>2</sub> emissions and demand for raw materials [7]. It has been shown that if the performance and longevity of cement-based materials is increased by 50%, the demand for cement, aggregates and water will be reduced by 15%, 2.9 to 7.6 Gt and 0.28 to 0.83 Gt, respectively [8]. And it will also reduce energy consumption by 10<sup>6</sup> to 2.3 x 10<sup>6</sup> TJ and CO<sub>2</sub> emissions by 0.4 to 0.7 Gt of CO<sub>2</sub>-eq [8]. This suggests that increasing the longevity of in-use of concrete infrastructure systems by enhancing the performance of OPC-based materials could be a critical means to reducing their environmental impacts.

The strength performance of OPC-based materials depends on the amount of their hydration products, especially the calcium-silicate-hydrate (C-S-H) phases, the principal binding agents in concretes [9]. Higher content of C-S-H phases increases the

engineering properties and improves the durability of OPC-based materials. This allows concrete infrastructure systems to have much longer service life with limited maintenance, thus lower carbon footprint.

Several approaches have been examined with the objective of increasing the hydration phases of cementitious composites. For example, the use of one-dimensional (1D) nanomaterials in cementitious composites have been shown to enhance the engineering properties of the cementitious nanocomposites and ultimately their longevity and sustainability. It was found that the addition of carbon nanotubes (CNTs) and carbon nanofibers (CNFs) to cementitious materials increases the strength and stiffness of the cementitious nanocomposites [10–12]. CNTs and CNFs can control the nanoscale properties of cementitious nanocomposites such as hydration, matrix cracks from shrinkage and mechanical stresses. Previous studies demonstrated that CNTs and CNFs can improve the hydration kinetics of cement pastes, leading to improved growth of the hydration products [11,13–16]. Because of their large specific surface area, 2D nanomaterials such as graphene (G), graphene oxide (GO) and boron nitride (BN) outperform CNTs and CNFs in improving the hydration kinetics of cementitious composites and creating stronger and crack resistant cementitious composites [17–19].

However, due to high costs and energy consumption, and process-derived CO<sub>2</sub> emissions from their production, G, GO, BN, CNTs and CNFs have not been used on an industrial-scale manufacturing of cement-based products.

Cellulosic nanomaterials have emerged as promising low-cost and abundant bio-derived materials that can improve the performance of cement-based materials. One-dimensional (1D) cellulose nanocrystals (CNCs) were used to fuse cementitious composites with the objective of improving the engineering properties of cementitious composites by increasing their hydration products [20–23]. However, due do their small

size and low-specific area, CNCs slightly improved the hydration kinetics of cement, resulting in a moderate enhancement of mechanical properties [24].

Electrochemical techniques such as polarization methods, cyclic voltammetry, AC impedance spectroscopy, and the new time-resolved methods are increasingly being used to characterize materials [25–29]. Recently, electrochemical impedance spectroscopy (EIS) has emerged as a powerful method for characterizing the hydration behaviour of cementitious composites, enabling a comprehensive understanding of the hydration kinetics [30]. In this method, a cementitious composite is treated as an electrochemical cell and its electrochemical impedance  $Z$  is measured by applying an AC voltage  $V$  over a wide range of frequencies, then measuring the current  $I$  across the cell. The electrochemical impedance  $Z$  is calculated as  $Z = V/I$  [31]. The impedance measurements are typically plotted in the form of Nyquist plots where their shape is used to extract crucial information about the cementitious composite characteristics during hydration such as changes in the chemical, electrical and microstructure features [32]. The impedance measurements are also used to model the cement composite using equivalent circuit (EC) elements to uncover the effect of the cement paste ingredients on the hydration kinetics [32]. The impedance measurements are often complemented by the cyclic voltammetry (CV) measurements. CV measurements are commonly used to analyze chemical reactions and ion diffusion in cells such as energy systems [33]. CV involves measuring the current while sweeping a voltage across the cell. The measured current is affected by the electron transfer between the chemical species within the cell and the electrodes, and ion diffusion and migration within the cell solution [33]. Even though, it has not yet been used in cementitious materials extensively, CV can shed light on the electrochemical processes in cementitious materials

by quantifying the dissolution of the cement particles and the change in the pore solution, and the subsequent formation of the hydration phases.

Recently, we have successfully synthesized novel microsheets from sugar beet pulp (SMS) recovered from solid waste of the sugar industry for use in cementitious materials [34]. Unlike current 2D nanomaterials, the developed SMS microsheets have larger specific area and contain a larger number of hydroxyl groups on their surfaces, thus more easily dispersed in water. The SMS microsheets are renewable and much cheaper (around \$10/kg) than existing 2D nanomaterials, thus making them suitable for large applications in the construction industry to improve the performance and reduce the carbon footprint of construction materials. Recently, we have demonstrated through computation that SMS significantly increases the engineering properties of cementitious composites. Indeed, our molecular dynamics simulations have shown that this improvement is attributed to the ability of SMS to both strengthen the hydration product particles and improve the hydration kinetics of cement [35–37].

The effect of the newly developed SMS on the hydration kinetics of OPC is quite complex and is not thoroughly understood, and the interaction mechanisms between the SMS and the OPC particles during hydration are still not experimentally established. Therefore, deep understanding of the hydration behaviour of these new SMS-cementitious composites through experimentation is deemed necessary for the design and optimization of their engineering properties. This will accelerate the adoption of these low-carbon materials in the construction industry.

In this paper, for the first time, we combine cyclic volumetric (CV) and the electrical impedance spectroscopy (EIS) techniques to uncover new hydration functions of SMS in cementitious materials and elucidate the main hydration kinetics of the SMS-cementitious composites. The interaction between the SMS sheets and the cement

particles in their fresh state was firstly determined through centrifugation tests. Then, the influence of SMS on the hydration mechanism of the cement pastes was probed using EIS and CV. An equivalent circuit model for the cementitious composites was developed to ascertain the role of the SMS sheets in the cement hydration kinetics. In addition, BET, TGA, DSC, SEM and TEM analytical tools were used to characterize the SMS sheets and quantify their effect on the formation of the hydration products and the evolution of the microstructure of the cementitious composites. And the quantified  $\text{Ca}(\text{OH})_2$  content and DOH were correlated with the two main CV and EIS parameters: capacitance and electrical impedance.

## **2. Experimental program**

### *2.1. Preparation of the SMS material*

The SMS manufacturing process is shown in Fig. 1 and discussed in detail in [34,37]. The first step of the manufacturing process involved diluting sugar beetroot pulp with a solid content of 1.0% by weight. The pH of the mixture was then raised and kept constant at 14 by adding a 0.5M sodium hydroxide (NaOH) solution. Subsequently, the amounts of hemicellulose and pectin were extracted from the mixture. The mixture was then homogenized at a temperature of 90°C for 5 hours using a stirring blade with a rotation speed of 11m/s. The homogenized solution was filtered to remove the dissolved material, resulting in an SMS paste with a solid content of 8% and an average SMS sheet size of 50 $\mu\text{m}$  x 50 $\mu\text{m}$  in lateral size and 0.25 $\mu\text{m}$  thickness. The manufacturing process consumes low power and is interfaceable with renewable electricity, enough to operate all sub-processes in the SMS making.

The environmentally friendly SMS are formed by linked  $\beta$ -1-4 glycosidic (C-O-C) bonds. The chemical functional groups on the SMS backbone tetrahydropyran ring

include hydroxymethyl group (-CH<sub>2</sub>OH), hydroxy group (-OH) and hydrocarbon methine group (-H) (Fig. 1). Compared to GO, the high content of hydroxyl and hydroxymethyl groups makes SMS more efficiently and evenly dispersed in aqueous solutions.

## *2.2. Preparation of the cement pastes*

Ordinary Portland Cement (OPC) type CEM I 52.5 N with a water-cement ratio of 0.35 was used to prepare the cement pastes. A commercially available superplasticizer (Glenium 51) was used at a concentration of 1-wt% to enhance the workability of the cement pastes. Solutions with concentrations of 0, 0.1, 0.2 and 0.3-wt% of SMS were prepared and added to the cement pastes. To keep the water/cement ratio of 0.35 constant throughout the experimental program, the required amount of mixing water was adjusted to take into consideration the water that is already available in the SMS paste. The solutions were prepared by sonicating the required amounts of SMS, water and superplasticizer for a period of 30 minutes using a tip sonicator (S-450A Branson Ultrasonics<sup>TM</sup> Sonifier<sup>TM</sup>) under 50% duty cycles. The SMS suspensions were mixed with cement for 7 minutes and the resulting cement pastes were poured into 50 mm x 50 mm x 50 mm and 40 mm × 40 mm × 160 mm plastic moulds.

The mini-slump test was performed to evaluate the influence of SMS on the workability of cementitious composites. The spread diameters formed by the pastes were measured upon lifting a mini-slump cone with top diameter, bottom diameter and height of 70 mm, 100 mm, and 60 mm, respectively [38]. During the test, the paste was carefully poured into the mould and subsequently vibrated. After removing the excess paste from the top surface, the mould was lifted vertically to allow the cement paste to cure for 24 hours, the slump diameter was then determined as the average of two measurements for each SMS dosage [39].

The cube specimens were used to quantify the compressive strength, hydration and microstructure evolution of the cementitious composites using TGA/DSC, SEM, EDS and BET analytical tools. The prisms were used to investigate the flexural strength and hydration mechanism of the SMS-modified cementitious composites using CV and EIS. Stainless steel electrodes were inserted into the prisms with 120 mm apart to enable CV and EIS measurements. The prisms and the cubes were left to cure for 24 hours at room temperature and then cured in water for 7, 14 and 28 days at a temperature of 22°C.

### *2.3. Centrifugation test of cementitious composites*

We hypothesize that the hydration kinetics of the cementitious composites are controlled by the synergetic interaction between the cement particles and the SMS sheets. And this synergetic interaction is governed by the amount of SMS sheets adsorbed (a-SMS) onto the surface of the cement particles. As such, centrifugation tests were carried out following [40] to determine the concentration of a-SMS using a MSE Mistral 2000 centrifuge. Cement pastes with a mass of 200g containing SMS at concentrations of 0, 0.1, 0.2 and 0.3-wt% were centrifuged after mixing. The pastes were placed in centrifugal bottles and centrifuged at 3000 rpm for 20 minutes. Subsequently, the centrifuged supernatants were collected and filtered through Cole-Parmer Sterile Cell strainers (40 µm) to remove the cement particles. The filtrates were then oven dried at 45°C for 48 hours to evaporate the water. The dried filtrates obtained from the plain cement pastes contained cement supernatant salt and alkali that are available in the pore solution [41]. And the dried filtrates obtained from the SMS infused cement pastes contained free SMS (f-SMS), and cement supernatant salt and alkali that are in the pore solution. The amount of f-SMS was obtained by subtracting the weight of the dried filtrates obtained from the plain paste from the weight of the dried filtrate obtained from the paste infused with SMS.

The amount of a-SMS was obtained by subtracting the weight of f-SMS from the weight of SMS added to the paste as outlined in [40].

#### *2.4. Electrochemical characterization of the cementitious composites*

The electrochemical behaviour of the cement pastes was investigated with cyclic voltammetry (CV) and electrochemical impedance spectroscopy (EIS) to elucidate the influence of SMS on the evolution of the hydration kinetics of the cementitious composites at 7, 14 and 28 days, using the cement pastes as electrochemical cells. Potentiostat (Gamry Interface 1000) was employed to obtain the CV characteristics of the cementitious composites using the two-probe method as shown in Fig. 2. During this test, an electrical current was passed through the cementitious composite as the voltage is swept between -0.5 V and 0.5 V using a scan rate of 0.2V/s for 10 cycles. Gamry software<sup>TM</sup> was used to produce current vs voltage spectra to extract qualitative hydration kinetics of the cementitious composites.

The EIS measurements were carried out using frequencies between 0.1 Hz and 1 MHz and a sinusoidal voltage of 10 mV. Gamry software<sup>TM</sup> was employed to analyse the EIS results and obtain the equivalent circuit for the cementitious composites.

#### *2.5. Thermal analysis of cementitious composites*

Thermal analysis of SMS and cement pastes was carried out via the thermogravimetric analysis (TGA) and differential scanning calorimetry (DSC) analysis methods using STA 449 F3 Jupiter instrument. This was done to characterize the thermal behaviour of the SMS sheets and cement pastes, and quantify the degree of hydration (DOH) and the change in the calcium hydroxide ( $\text{Ca}(\text{OH})_2$ ) content in the cementitious composites. Air dried SMS samples were transferred into  $\text{Al}_2\text{O}_3$  crucibles for heating. During heating, the apparatus chamber temperature was gradually increased from 20°C to 1100°C at a rate of 10°C/min. Cementitious samples obtained by crushing cement

cubes were grounded into powder to carry out the thermal analysis of the cementitious composites at 7, 14 and 28 days. The powdered cementitious samples were placed in  $\text{Al}_2\text{O}_3$  crucibles for heating. During heating, the chamber temperature was first raised from 20°C to 140°C at a heating rate of 10°C/ min. Then, the temperature was held at 140°C for 30 minutes to remove evaporable water [42]. Finally, the samples were subjected to heat from 140°C to 1100°C at a heating rate of 10°C/min. The TGA and DSC experiments were conducted under nitrogen with a flow rate of 25.00 ml/min and were repeated three times.

#### *2.6. Microstructure characterization of the cementitious composites*

The morphology of the SMS sheets and SMS-infused cement pastes was examined using scanning electron microscopy (SEM) (JEOL JSM-7800F) fitted with X-Max50 Silicon Drift Detector (SDD) of an area of 50 mm<sup>2</sup>. After coating with gold, SEM micro images of the air-dried SMS sheets and the fractured surface of the cement samples (prepared at 7, 14 and 28 days) were produced at a voltage of 2-15 kV and room temperature. JEM-1010 transmission electron microscope (TEM) was used to determine the morphology of the SMS sheets. A 0.2-wt% SMS suspension was first diluted and ultrasonicated for 30 minutes. The solution was then deposited onto carbon-coated TEM grids. The excess liquid was removed with a filter paper and the samples were air-dried at room temperature. The TEM images were produced at an accelerating voltage of 80 kV voltage.

XRD analysis was performed using an Agilent SuperNova single-crystal X-ray diffractometer. Cementitious composite samples containing SMS were prepared in a powdered form at 7 and 28 days to facilitate the XRD examination. The XRD patterns were obtained by scanning from 5° to 65° (2 $\theta$ ) with Cu K $\alpha$  radiation ( $\lambda = 1.5418\text{\AA}$ ) at a scanning rate of 2°/minute, under ambient conditions. The X-ray diffractometer operated

at a voltage of 40kV using a filament current of 40mA and a step size of 0.02°. The pore size, pore volume and specific surface area of the SMS sheets and cementitious composites were quantified by the Brunauer–Emmet–Teller (BET) method using a nitrogen adsorption instrument (MICROACTIVE 3FLEX 3500, Micromeritics, Germany). Prior to testing, The SMS samples were dehydrated in the vacuum and dried at 40°C for 120 minutes under a pressure  $10^{-6}$  Pa and the cementitious composite powder samples (sieved less than 1 mm) were dehydrated in the vacuum and dried at 100°C for 180 minutes under a pressure of  $10^{-6}$  Pa.

### *2.7. Mechanical characterization of the cementitious composites*

The influence of SMS on the compressive strength of the cementitious composites was evaluated using an universal testing machine (UTM) (Instron 8802J5219, 250KN) according to ASTM C 109 [43], at a loading rate of 0.5 MPa/s. The compressive strength of the cubes (50 mm x 50 mm x 50 mm) were determined at 7, 14 and 28 days. The prisms were tested on an ASTM Zwick Roell Z020 machine (C090204019, 20KN, Germany). The flexural strength of the cementitious composites was evaluated using a four-point bending test at 7, 14, and 28 days in accordance with ASTM C78 [44]. Prisms (40 mm x 40 mm x 160 mm) were tested using a displacement control at a constant loading rate of 0.01 mm/min.

## **3. Results and discussion**

### *3.1. Morphology, thermal behaviour and pore structure of SMS*

Fig. 3a-b shows SEM images of the SMS sheets. As can be seen, the morphology of the SMS sheets consists of rippled and wrinkled surface textures. Fig. 3b shows a typical SEM image of the SMS sample with a total thickness of about 0.25 mm. From this figure, we can see that the sample is composed of stacked and overlapped sheets. The

SMS sheets have a thickness of about 0.25  $\mu\text{m}$  (Fig.3b). The TEM images in Fig. 3c-d indicate that the SMS are consisting of randomly oriented and stacked nanofibers with diameters in the 5-8 nm range. The average lateral size of the SMS sheet is about 50  $\mu\text{m}$ .

The thermal stability of the SMS sheets is an important parameter as it indicates whether the SMS sheets can resist the action of heat generated during cement hydration. The thermal behaviour of the SMS sheets is shown in Fig. 3e. From this figure we can see that the thermal decomposition process of SMS is mainly divided into two stages: slow pyrolysis in the temperature range of 20°C to 200°C and rapid pyrolysis in the temperature range of 200°C to 600°C. The slow pyrolysis is the mass loss of the hydrophilic bound water by evaporation whereas, the rapid pyrolysis is the sharp mass loss of the functional groups after SMS dehydration. This is due to the thermal degradation of both the functional group of SMS in the temperature range of 200°C to 380°C and the tetrahydropyran ring backbone structure of SMS in the temperature range of 440°C to 580°C. The DTG peaks indicate that the maximum temperature depolymerization of the SMS functional groups is 329°C and the depolymerization temperature of the tetrahydropyran ring of SMS is around 518°C. The mass loss of SMS remains unchanged between 580°C and 1100°C with a residual mass weight of 20%.

Fig. 3f shows the DSC thermogram and its derivative for the SMS sheets in the temperature range of 20°C to 1000°C. From the derivative of the DSC curve, we can see that the first endothermic broad peak between 20°C and 200°C corresponds to the rearrangement of the molecular chains of SMS caused by the evaporation of bound water. The second endothermic peak between 200°C and 380°C is attributed to the colloidal bond cleavage. The third endothermic transition between 440°C and 580°C corresponds to the depolymerization of cellulose based SMS. The occurrence of the endothermic hump and the first peak phenomena are similar to amorphous cellulose [45]. It is worth noting

that conventional cellulose typically completes its depolymerization over a temperature range of 200°C to 400°C [46,47], whereas the depolymerization of the tetrahydropyran ring backbone of the SMS material is completed over a temperature range of 200-580°C. This indicates, the SMS material has higher thermal resistance than conventional cellulose [46] and can resist the cement hydration temperature which is about 70°C.

The N<sub>2</sub> adsorption-desorption isotherms of the SMS sheets are shown in Fig. 4a. This figure shows that the SMS sheets have a BET specific surface area of 68.35 m<sup>2</sup>/g. The pore size distribution and total pore volume of SMS calculated according to BJH theory are shown in Fig. 4b. As can be seen, the average pore diameter and the pore volume of SMS are 8.19 nm and 0.14 cm<sup>3</sup>/g, respectively. Fig. 4b indicates that the pore size distribution of SMS is a bimodal pore size distribution in the 0-10 nm range with a small number of pores in the 40-80nm range. It is worth mentioning that in comparison to SMS, GO exhibits lower specific surface area [48]. This means SMS outperforms GO for boosting the hydration of cement particles due their higher reactive surface area.

### *3.2. Interaction of SMS sheets with cement particles*

Fig. 5a illustrates the change in the workability as a function of SMS dosage. As shown, the addition of 0.1, 0.2 and 0.3-wt% SMS did not affect the workability of the cement pastes. However, the workability decreased significantly at SMS dosages higher than 0.3-wt%. The addition of 0.40-wt%, 0.50-wt%, and 0.60-wt% SMS decreased the diameter of the pastes by 86.59%, 90.75%, and 96.05%, respectively. This can be attributed to the high specific surface area of SMS and its dominant hydrophilic functional groups which tend to absorb and consume most of the free water in the cement pastes. This results in increased friction between the cement particles which in return decreases the workability of the cement pastes [49].

The effectiveness of the SMS sheets in promoting the dissolution of  $C_3S$  compound during hydration is governed by the direct chemical interaction of  $C_3S$  with the SMS sheets adhered to the surface of the cement particles. The higher the amount of the adhered SMS sheets, the higher the surface hydroxylation rate of  $C_3S$ . As such, the experimental results obtained from the centrifugation experiments were used to determine the amount of a-SMS adhered to the surface of the cement particles. Fig. 5b shows the change in the mass of a-SMS per gram of cement as a function of SMS concentration, whereas Fig. 5c shows the change in the percentage of a-SMS (i.e.,  $a\text{-SMS}/(a\text{-SMS}+f\text{-SMS})$ ) as a function of SMS concentration. As shown in Fig. 5c, the mass of a-SMS is directly proportional to the SMS concentration, where about 92% of SMS are adhered to the surface of the cement particles. The interaction mechanism of SMS with a cement particle is illustrated in Fig. 5d. As depicted, the large surface area and the chemical functional groups enable the SMS sheets to cling to the surface of the cement particle. The large negatively hydroxymethyl ( $-\text{CH}_2\text{OH}$ ) hydroxyl ( $-\text{OH}$ ) groups on the surface of SMS are attracted to the main positively charged  $\text{Ca}^{2+}$ , leading to an electrostatic self-assembly mechanism and the cement particles become wrapped around by the SMS sheets. Here, we believe that the f-SMS sheets (8% of total SMS) remain in the pore solution. The following sections elucidate the effect of the SMS sheets on the hydration kinetics of the cementitious composites.

### *3.3. Thermal analysis of the cementitious composites*

The influence of SMS on the hydration of the cement pastes can be quantified by simply analysing the heat flow and heat of fusion obtained from the DSC measurements. Fig. 6a depicts the effect of SMS on the heat flow first peak at 7 days. The first peak which is known as the dissolution peak is associated with the dissolution of calcium silicate phases and the initial precipitation of ettringite [50]. As shown, the intensity of

the dissolution peak increases as the SMS concentration increases. This can be attributed to the fact that the SMS sheets with high specific area accelerate the hydration of cement and provide additional surface for nucleation and growth of the hydration phases [51]. As such, the more SMS is used, the more heat is generated. Fig. 6a also shows that the dissolution peak shifts to the left due to the addition of SMS. This means that SMS increases the dissolution rate of the cement phases. This can be confirmed by the change in the latent heat of fusion of the cementitious composites as shown in Fig. 6b. As can be seen, the latent heat fusion of the cementitious composites increases with both curing age and SMS concentration due to the increase of the hydration products.

The influence of SMS on the formation of the hydration phases can also be quantified from the thermal degradation of the hydrated cement pastes. Fig. 7a-c displays the effect of SMS on the thermal decomposition of the cementitious composites at 7, 14 and 28 days where amount of the mass loss gradually increases with SMS concentration. Fig. 7a-c show that the thermal decomposition of the cement pastes goes through three main weight loss stages. The weight loss of the cement pastes due to the gradual loss of the bound water takes place in the first stage, between 140 and 300°C. In the second stage, the thermal dehydration of  $\text{Ca(OH)}_2$  occurs in the temperature range 420 to 480°C. Finally, in the third stage, the decomposition of calcium carbonate ( $\text{CaCO}_3$ ) takes place between 600 and 780 °C [40,52]. As can be seen in Fig. 7c, the final weight loss of the cement pastes at 28 days increases with SMS concentration due to more evaporation of the chemically bound water (CBW) from the thermally decomposed hydration products.

Fig. 7d-f show the derivative thermogravimetry (DTG) curves of the cement pastes at 7, 14 and 28 days. The DTG peaks in this figure indicate that the cementitious composites lost their CBW or decomposed at a specific temperature range, regardless the SMS content. The range of pyrolysis peaks shown in Fig. 7d-f confirm that the weight

loss of C-S-H (140-300°C), Ca(OH)<sub>2</sub> (420-480°C) and Ca(CO<sub>3</sub>) (600-780°C) phases occurs in different temperature ranges. The increase in the intensity of the DTG peaks due to the addition of SMS is an indicative of more hydration products being decomposed. Furthermore, the decomposition peak of Ca(CO<sub>3</sub>) phase gradually shifts towards the left (decomposition temperature decreased around 10°C) when the SMS content increases. This is due to the decomposition of SMS/Ca(CO<sub>3</sub>) composites which takes place slightly prior to the plain Ca(CO<sub>3</sub>) phase. The DTG results further demonstrate that the addition of SMS amplifies the formation of the hydration phases.

The thermal mass loss of the cementitious composites is related to DOH. Hence, the DOH was calculated according to the method described in [42].

$$DOH(TGA) = \frac{m(cbw)}{m(remain)} \cdot 0.23 \quad (1)$$

Where  $m(cbw)$  is the mass of chemically bound water and  $m(remain)$  is the mass of samples remaining in the crucible.

Fig. 7g shows the calculated DOH at 7, 14 and 28 days. As shown, the DOH increases with SMS content. At a SMS content of 0.3-wt%, the DOH increased by 3.5%, 6.1% and 5.6% at 7, 14 and 28 days, respectively. Fig. 7h shows the effect of SMS on the amount of Ca(OH)<sub>2</sub>. The amount of Ca(OH)<sub>2</sub> in the cementitious composites was calculated according to [34]. As can be seen, the trend of Ca(OH)<sub>2</sub> increasing with SMS concentration is similar to that of DOH. At a SMS content of 0.3 wt% increased the amount of Ca(OH)<sub>2</sub> by 5.04%, 10.29% and 13.45% at 7, 14 and 28 days, respectively. The increase of Ca(OH)<sub>2</sub> is indicative of the increase of the other hydration products such as C-S-H as a result of the addition of SMS.

### 3.4. Electrochemical response of SMS cementitious composites using voltammetry

The hydration kinetics behind the observed increase in DOH and  $\text{Ca(OH)}_2$  are uncovered by examining the electrochemical response of the cementitious composites. As such, the influence of the SMS sheets on the electrochemical behaviour of the cement pastes during hydration was investigated using CV where the electrochemical cement paste cells were charged and discharged between -0.5 V and 0.5 V. Fig. 8a-c show the CV curves at different SMS concentrations and curing ages. CV plots the amount of the electrical current flowing through the electrochemical cement cell when the voltage is varied between -0.5 V to 0.5 V. As shown, the CV curves exhibit elliptical and symmetrical shapes, indicating that the cementitious composites are behaving like electric capacitors [53]. From the CV curves, the peak current is estimated at a potential of 0.5 V and plotted against SMS concentration at different curing ages as shown in Fig. 8d. As it can be observed, the intensity of the current flowing through the cement pastes during hydration increases with SMS concentration and decreases with increasing curing age. This means the SMS sheets facilitate the movement of electrons towards the electrodes while the curing age diminishes the movement of electrons towards the electrodes. This electrochemical reaction mechanism can be ascertained by examining the influence of the SMS sheets on the capacitance of the electrochemical cement pastes.

The capacitance  $C$  of the electrochemical cement paste cells was calculated using the following equation [54]:

$$C = \frac{\int IdV}{2\nu\Delta V} \quad (2)$$

Where  $\int IdV$  is the integrated area of the CV curve,  $\Delta V$  is the potential voltage window and  $\nu$  is the scan rate (V/s). The influence of SMS on the capacitance of the cement pastes at 7, 14 and 28 days is shown in Fig. 9a. As illustrated, at a specific curing age, the

capacitance of the cementitious composites increases with increasing SMS concentration. This increase however is predominant in the first 7 days of hydration. The a-SMS sheets increases the ionic strength (i.e., increased ion concentration) of the pore solution, as a consequence of their direct interaction with  $C_3S$ . The chemical functional groups such as hydroxymethyl ( $-CH_2OH$ ), hydroxy ( $-OH$ ) and hydrocarbon methine group ( $-H$ ) allow for dissolution catalysis to occur due to the interaction of the a-SMS sheets with the highly reactive  $C_3S$ . This increases the density of ions, mainly  $Ca^{2+}$  and  $OH^-$ , which in return increases the ionic strength of the pore solution. This increase could also be attributed in part to the accumulation of the released ions (i.e.,  $Ca^{2+}$ ,  $OH^-$ ) into the porous a-SMS sheets. As the hydration progresses the ions in the pore solution are consumed and amount of the hydration phases are increased. This dampens the diffusion and electric mobility of ions which results in reduction of the capacitance of the cement pastes when the curing age increases.

The influence of DOH and  $Ca(OH)_2$  on the capacitance of the cementitious composites is shown in Fig. 9b-c at the three SMS concentrations. The increase in DOH and  $Ca(OH)_2$  is a good indicator of the evolution of the other hydration phases such as C-S-H products. As shown, the capacitance is proportional to both DOH and  $Ca(OH)_2$ . The rate of change of the capacitance with respect to DOH and  $Ca(OH)_2$  is more predominant at 7 days due to higher ionic strength of the cementitious composites. The lower rate of change of the capacitance at 14 and 28 days of curing is due to lower ionic conductivity of the cementitious composites due to the consumption of ions in the pore solution. The positive change in the capacitance of the cement pastes reflects the increase in the hydration phases resulting from the inclusion of SMS. As such, the cyclic voltammetry method presents a good tool to understand and monitor the hydration of cementitious composites containing reactive additives.

### 3.5. Electrochemical response of SMS cementitious composites using EIS

EIS characterization was used to complement the CV analysis of the hydration kinetics of the cementitious composites. Fig. 10 shows the Nyquist plots for the cementitious composites at 7, 14 and 28 days. As illustrated, each Nyquist plot is composed of a depressed capacitive arc in the high frequency region and somewhat a straight line representing the Warburg impedance in the low frequency region. The depressed capacitive arc represents the charge transfer at the electrode-ionic solution interface and the straight line represents the diffusion of ions into the electrodes. It is worth noting that in the middle-frequency range, the impedance of the cementitious composites somewhat decreases with the curing age. This is probably due to the effect of the porosity of the hydration phases. Previous studies have shown that Nyquist plots in the medium-frequency region describe the effect of porosity of materials on the ionic conductivity [55]. C-S-H phases are porous and considered as ionic materials due to their good ionic conductivity [56]. Hence, we hypothesize that the observed change in the impedance in the medium-frequency range is due to the fact that as the hydration continues, more C-S-H phases are produced thereby facilitating ion diffusion through their pores which in return decreases the electrical resistance of the matrix.

The EIS data was further analysed to delineate effect of SMS on the change in the hydration products of the cementitious composites. This was done by examining the change in the bulk resistance and dielectric constant of the cementitious composites. The bulk electrical resistance was calculated from the bode plot of the impedance modulus  $\log|Z|$  and phase as depicted in Fig. 11a. In this figure, a cementitious composite with 0.1wt% SMS is used as an example to show how the bulk electrical resistance was calculated. As shown in Fig. 11a, the blue dashed rectangles show the phase plateauing near zero in the high frequency range of  $5 \times 10^3$  to  $5 \times 10^4$  Hz and the  $\log|Z|$  values in this

frequency range where the phase is plateauing near zero. In this frequency range, the cementitious composite exhibits a resistive behaviour, and its bulk electrical resistance can be calculated from the average  $\log|Z|$  values as  $R (\Omega) = 10^{\log|Z|}$ .

The bulk resistance values are given in Fig. 11b at 7, 14 and 28 days for different SMS concentrations. This figure indicates that there is a trend of increasing bulk resistance with increasing SMS concentration due to enhanced growth of the hydration products. This can be demonstrated in the plot of the bulk electrical resistance versus the degree of hydration (Fig. 11c), obtained from the thermal analysis of the cementitious composites. Fig. 11c shows that the bulk electrical resistance increases with increasing DOH. This is because the formation of the hydration phases consumes the highly conductive ions in the pore solution thereby increasing the bulk electrical resistance of the cementitious composites [57]. This implies that EIS is a useful tool for both interpreting the hydration processes of cement and real time monitoring of DOH.

The change in the dielectric constant ( $\epsilon'$ ) of the cementitious composites at 28 days is shown in Fig. 11d. The dielectric constant ( $\epsilon'$ ) was calculated using the following equation:

$$\epsilon' = \frac{dZ''}{2\pi Z^2 \epsilon_0 A} \quad (3)$$

where  $d$  is the distance between the electrodes,  $Z''$  is the imaginary impedance,  $Z$  is the total impedance,  $\epsilon_0$  is the vacuum dielectric constant and  $A$  is the contact area of the electrodes. Fig. 11d shows that the dielectric constant of cementitious composites decreases with frequency. This is due to the reduction of space charge polarization effect. During the hydration of the plain cement paste, the primary  $\text{Ca}^{2+}$  and  $\text{OH}^-$  ions are leached from  $\text{C}_3\text{S}$ . These unbound charged ions polarize in response to the applied electric field

which is responsible for the measured dielectric constant of the cement paste. As the hydration kinetics progress,  $\text{Ca}(\text{OH})_2$ , C-S-H and ettringite hydration phases begin to form which in return hinders the polarization of the charged ions thereby reducing the initial dielectric constant [58,59]. Fig. 11d also shows that at a fixed frequency, the dielectric constant of the cementitious composites decreases with increasing SMS concentration. This decrease is attributed to the effect of SMS on the hydration kinetics of cement. The addition of SMS increases the release of the primary  $\text{Ca}^{2+}$  and  $\text{OH}^-$  ions into the pore solution, resulting in higher ionic conductivity (i.e., higher ionic strength of the pore solution). This amplifies the growth of the hydration phases. These hydration phases along with the porous SMS sheets hamper the polarization of the charged ions, resulting in a further decrease in the dielectric constant. This means, the more SMS sheets in the cement paste, the lower the dielectric constant, as shown in Fig. 11d.

### *3.6. Equivalent circuit model for the SMS cementitious composites*

To further understand the hydration process of the cementitious composites and delineate the main mechanisms by which the SMS sheets accelerate the hydration rate of cement, an equivalent circuit (EC) model was developed and the effect of the addition of SMS on its electrical components was characterized. The two in-series-components of the EC model for the cementitious composites are shown in Fig. 12a. Bode plots showing the fit of the EC model to the measured impedances at 28 days are given in Fig. 12b-e. This figure indicates that the EC model fits adequately the measured impedances.

In the EC model, the cement paste is represented by its pore solution resistance ( $R_s$ ), double layer capacitance ( $C_{dl}$ ), charge transfer resistance ( $R_{ct}$ ) and Warburg impedance ( $Z_w$ ) and the electrodes are represented by their capacitance ( $C_e$ ) and resistance ( $R_e$ ).

The Warburg element ( $Z_W$ ), represents the ion diffusion in the cement paste. The Warburg element is generally described by its parameters in the following equivalent impedance equation.

$$Z_W = \sigma \omega^{-\frac{1}{2}}(1 - j) \quad (4)$$

$$\omega = 2\pi f \quad (5)$$

where  $\sigma$  is a Warburg diffusion coefficient and  $f$  is the operating frequency.

The values of the EC components were determined for each SMS concentration and curing age by fitting the experimental impedances using Gamry Echem Analyst program version 6.25. The fitted values of the EC model components and their errors are given in Table 1.

The total impedance  $Z$  of the equivalent circuit model shown in Fig. 12a can be expressed as:

$$Z = R_s + \frac{R_{ct} + \sigma \omega^{-\frac{1}{2}}(1 - j)}{1 + j\omega R_{ct} C_{dl} + j\omega Z_W C_{dl}} + \frac{R_e}{1 + j\omega R_e C_e} \quad (6)$$

The real part  $Z'$  is given by:

$$Z' = R_s + \frac{R_{ct} + \sigma \omega^{-\frac{1}{2}}}{\left(1 + \omega^{\frac{1}{2}} \sigma C_{dl}\right)^2 + \omega^2 C_{dl}^2 \left(R_{ct} + \sigma \omega^{-\frac{1}{2}}\right)^2} + \frac{R_e}{1 + (\omega R_e C_e)^2} \quad (7)$$

The influence of SMS on the hydration of the cement pastes can be elucidated by examining the change in the main cement paste parameters  $R_s$ ,  $R_{ct}$ ,  $C_{dl}$  and  $Z_W$  of the real parts of the impedance (Eqs. 7). Fig. 13a shows the effect of SMS on the resistance of the pore solution ( $R_s$ ) at different curing ages. As shown, the resistance of the pore solution increases with increasing SMS concentration. This can be attributed to the fact that the

ions and the free water are consumed immediately after the dissolution of the cement particles to produce hydration products which in return increases the resistance of the pore solution. Due to their high electrical resistance and surface area, the SMS sheets fill the capillary pores in the cement pastes thereby increasing their overall electrical resistance. Fig. 13a also shows that the electrical resistance of the pore solution increases with curing age due to the formation of the hydration gels in the capillary pores.

The influence of SMS on the charge transfer resistance ( $R_{ct}$ ) of the cement pastes at the at 7, 14 and 28 days is depicted in Fig. 13b. The charge transfer resistance represents the resistance against the process of electron movement between the cement paste and the electrodes resulting from the electrochemical reaction during hydration. The charge transfer in materials can be described by the following equation [60]:

$$R_{ct} = \frac{RT}{n^2 F^2 A C_0 K_{et}} \quad (8)$$

where  $R$  is gas constant,  $T$  is temperature,  $n$  is the number of electrons involved in the charge transfer process,  $F$  is Faraday's constant,  $A$  is the electrode surface area,  $C_0$  is the concentration of ions at the electrode surface and  $K_{et}$  is the electron transfer rate.

As shown in Fig. 13b, the overall trend of the charge transfer resistance decreasing with increasing SMS concentration and increasing with curing age supports the cyclic CV results. As previously highlighted, the interaction of the a-SMS sheets with  $C_3S$  increases the concentration of ions which results in higher number of electrons moving between the cement paste and the electrodes with a higher electron transfer rate. This reduces the charge transfer resistance. However, the charge transfer resistance somewhat increases with increasing curing age due to the formation of the hydration phases which reduces the diffusion of ions in the cement paste as shown in Fig. 13c.

Fig. 13c depicts the change in the Warburg impedance ( $Z_w$ ) as a function of SMS concentration. The Warburg impedance represents the bulk resistance to the ionic mass

transfer (i.e., diffusion mechanism of ions) in the cement paste. The Warburg impedance is associated with the Warburg coefficient  $\sigma$  (see Eq. 4), which represents the diffusion of ions in the cement paste. The higher the value of  $\sigma$ , the less the diffusion of ions in the cement paste. The Warburg coefficient  $\sigma$  is given by the following equation [61]:

$$\sigma = \frac{RT}{\sqrt{2}n^2F^2AC_0D^{1/2}} \quad (9)$$

Where  $D$  is the diffusion coefficient of ions in the cement paste.

The Warburg coefficient  $\sigma$  can be determined from the experimental real impedance data. Fig. 13d plots the experimental real impedance against the angular frequency ( $\omega^{1/2}$ ) (known as Warburg plot) for different SMS concentrations. The slope of the Warburg plot presents the Warburg coefficient  $\sigma$ . The effect of SMS concentration on the Warburg coefficient  $\sigma$  is shown in Fig. 13e. As can be seen from this figure, the Warburg coefficient  $\sigma$  decreases with increasing SMS concentration. This implies that the inclusion of SMS increases the diffusion coefficient of ions ( $D$  in Eq. (9)) during hydration. The C-S-H nanopores typically form the dominant pathways for ion diffusion and water transport in cementitious materials [62,63]. Higher ionic diffusion coefficients are typically associated with higher growth of C-S-H phases. Diffusion coefficient  $D$  of ions is typically larger in cement pastes with higher of C-S-H products than that in cement pastes with lower of C-S-H products [64]. Fig. 13e also shows that the Warburg coefficient  $\sigma$  increases with increasing curing age. As the hydration of the cement pastes progresses, water and ions in the pore solution are depleted and the amount of hydration phases is increased, resulting in less diffusion of ions.

Fig. 13f shows the effect of SMS concentration on the double-layer capacitance ( $C_{dl}$ ) of the electrode/cement paste interface at different curing ages. As depicted in Fig.

13f, at 7 days of curing, the double-layer capacitance increases with SMS concentration. The addition of SMS increases the accumulation of ions at the electrode-cement interface due to rapid dissolution of  $C_3S$ . This increases the double-layer capacitance of the cementitious composites.

The CV and EIS results support the notion that the hydration of cement is controlled by the kinetics of a-SMS/ $C_3S$  interfacial chemical interactions. The f-SMS sheets in the pore solution also contribute to the rapid dissolution of  $C_3S$ . The findings of the CV and EIS tests were leveraged to uncover the main hydration kinetics of the cementitious composites, taking into consideration the SMS surface functional groups that are the driving forces for the dissolution of  $C_3S$  and the growth of the hydration phases.

### *3.7. Elucidation of the hydration kinetics of cementitious composites*

The centrifugation, EIS and CV results were used to identify the main chemical processes involved in the hydration of the cementitious composites and delineate the role of the SMS surface functional groups in the dissolution of  $C_3S$ . The EIS and CV results revealed that the change in the electrochemical properties of the cementitious composites during hydration is governed by the ionic strength of the pore solution. This ionic strength is highly dependent on the concentration and the electric mobility (i.e., diffusion) of ions produced during the dissolution of  $C_3S$  and increases with SMS content.

The centrifugation test results revealed that most of SMS sheets tend to deposit on the surface of the cement particles (i.e., a-SMS sheets) (Fig. 14a) and a small amount of SMS sheets remain in the pore solution (i.e., f-SMS sheets). As such, we hypothesize that the dissolution kinetics of the cement particles are driven by both the a-SMS and f-SMS sheets. Based on this, we believe that the SMS material has unique two hydration functions in cementitious materials that had not been seen with other nanomaterials.

Fig. 14 describes these two hydration functions. The first function is the rapid hydroxylation of  $C_3S$  and the subsequent formation of the hydration phases as shown in Fig. 14b. In this case, the inner a-SMS layers directly in contact with the cement particle (Fig. 14b) undergo interfacial chemical reactions with  $C_3S$  in the presence of water. During this chemical process, the highly reactive  $C_3S$  breaks the inter- and intramolecular H-bonds between the hydroxyl/hydroxymethyl ( $-OH/-CH_2-OH$ ) functional groups of SMS which leads to deprotonation and the subsequent dissolution of the inner a-SMS layers (Fig. 14b). Consequently, a proton-rich environment is produced, and a fast proton exchange rate is enabled which results in a fast dissolution rate of  $C_3S$  (Fig. 14b). This process increases the ionic strength of the pore solution due to increased concentration of  $Ca^{2+}$  and  $OH^-$  ions which in return amplifies the formation of the hydration phases. The disruption of the inter- and intramolecular H-bonds between the hydroxyl/hydroxymethyl functional groups of the SMS layers also produces methanol ( $CH_3OH$ ) and ethanol ( $CH_2H_5OH$ ) organic chemical compounds (Fig. 14c) in the pore solution which boosts the mobility of protons. This further accelerates the hydroxylation of  $C_3S$  and increases the ionic strength of the pore solution, thereby intensifying the formation of the hydration phases.

The second function is channeling water molecules from the pore solution to the unhydrated cement core. The outer undissolved a-SMS layers (Fig. 14c-d) remain embedded in the hydration phases and facilitate the transport of water from the pore solution to the unhydrated  $C_3S$ . Unlike existing nanomaterials, the large specific surface area the number of functional groups allow SMS to diffuse water deep into the unhydrated  $C_3S$  core thereby increasing the hydration depth of the cement particle (Fig. 14d). Similar to the inner a-SMS layers, the f-SMS sheets in the pore solution chemically interact with  $Ca^{2+}$  and  $OH^-$  ions and undergo deprotonation due to the breakage of H-bonds between

their functional groups (Fig. 14b). This increases the density of protons involved in the ion exchange mechanism which accelerates the dissolution of  $C_3S$  and the subsequent release of  $Ca^{2+}$  and  $OH^-$  ions into the pore solution. This further amplifies the formation of the hydration phases.

### *3.8. Effect of SMS on the microstructure of the cementitious composites*

#### *3.8.1. Pore structure of SMS-cementitious composites*

The CV and EIS results elucidated the origin of the chemical reactions responsible for the enhanced hydration of cement when the SMS sheets are present. The effect of SMS on the microstructure of the cementitious composites was examined to confirm the CV and EIS experimental results. Fig. 15a shows the BET adsorption isotherms for the cementitious composites at 28 days. As shown in this figure, the isotherms are IUPAC classification type IV isotherms with H3 hysteresis loop. This indicates that the cementitious composites are marked by a very wide pore size distribution and contain mesopores [65,66]. Fig. 15a also shows that the hysteresis curves are quite narrow, and the adsorption and desorption branches are almost vertical and nearly parallel when the relative pressure is above 0.96, indicating the presence of slit-shaped pores in the cementitious composites [67].

The BET specific surface area (SSA) of the cementitious composites is given in Fig. 15b. As depicted, the SSA of the cementitious composites increases with increasing SMS concentration, and a maximum increase of 56.38% was obtained at a SMS concentration of 0.3 wt%. This demonstrates that the SMS increases the SSA of the hydration phases which is in line with previous studies on cementitious composites containing carbonaceous 2D nanomaterials such as GO and graphene [17,68,69].

The cumulative pore volume and its derivative (i.e., pore size distribution) as a function of the pore size are plotted in Fig. 15c-d. These figures show that the pore volume

increases with increasing SMS concentration. This is attributed to an increased amount of the C-S-H hydration products [70]. Fig. 15d indicates that the bulk of the pores is centred 5-8 nm.

### 3.8.2. Evolution of the microstructure of SMS-cementitious composites

The XRD patterns of the cementitious composites with SMS at 7 and 28 days are depicted in Fig. 16. As shown, all cementitious composites exhibited the same hydration products. However, the intensity of the crystal diffraction peaks were influenced by SMS. From Fig. 16, we can see that at 7 and 28 days, the intensity of the ettringite, calcium hydroxide, and calcium carbonate peaks increased with increasing SMS concentration. This is more apparent at 28 days. [The increase in the peak intensities is an indication of increased amount of the hydration phases resulting from the addition of SMS \[71\]. This is reflected in the increase of the mechanical properties of the cementitious composites containing SMS.](#)

The evolution of the microstructure of the cementitious composites at 14 days is shown in Fig. 17. The microstructure of the plain cement matrix (Fig. 17a) is of highly heterogenous nature and is marked by a high content of  $\text{Ca(OH)}_2$  particles with different sizes, pores, and unreacted cement particles. The addition of SMS renders the microstructure of the cementitious composites denser and somewhat homogenous. The microstructure of the cement matrix with 0.1-wt% contains stacked  $\text{Ca(OH)}_2$  particles intermixed with C-S-H gel (Fig. 17b). At higher SMS concentrations, the microstructure of the cementitious composites shows a compact microstructure with smaller  $\text{Ca(OH)}_2$  particles embedded in C-S-H gels as shown in Fig. 17c-d.

The effect of SMS on the microstructure of the cementitious composites at 28 days is shown in Fig. 18. As shown, the plain cementitious composite is mainly composed of agglomerated  $\text{Ca(OH)}_2$  particles. The cementitious composites containing SMS show

better packing density due to the increased  $\text{Ca(OH)}_2$  and C-S-H hydration phases. Ettringite needles embedded in C-S-H are observed in the cementitious composite containing 0.30 wt%. The observed changes in the microstructure of the cementitious composites further confirm the results of CV and EIS characterization, that the addition of SMS leads to larger amount of hydration phases and better microstructural packing.

### *3.9. Effect of SMS on the compressive and flexural strength of the cementitious composites*

Fig. 19a depicts the effect of SMS on the compressive strength of the cementitious composites at 7, 14 and 28 days. As shown, the compressive strength of all cementitious composites increases with curing age. It can also be seen that the addition of SMS resulted in a slight increase in the compressive strength. For a given curing age, the compressive strength somewhat plateaued between 0.1 and 0.3-wt% SMS, leading to an increase of 4.89%, 3.93%, and 8.33% at 7, 14 and 28 days, respectively. These low compressive strength gains are in line with other studies that showed GO is more effective in improving the flexural strength of cementitious composites than the compressive strength [72,73]. It was found that the crack-bridging mechanism induced by GO increased the flexural strength more than the compressive strength [74].

Fig. 19b depicts the variation of the flexural strength of the cementitious composites as a function of SMS concentration at 7, 14, and 28 days. As shown, the 0.20-wt% concentration produced the highest flexural strength. At this concentration, the flexural strength is improved by 13.16%, 34.63% and 31.56 at 7, 14 and 28 days, respectively. This enhancement in the flexural strength is attributed to the improved hydration kinetics which resulted in more hydration products. The improvement of the flexural strength of the cementitious composites is attributed to the higher hydration degree and the reinforcing and crack-bridging effect provided by the SMSs. Owing to their hydroxyl groups, the SMSs can easily intercalate into the hydration products thus

linking them together to form a denser and packed microstructure. The enhanced SMS-matrix adhesion/interlocking characteristics resulting from the wrinkled SMS sheets also improve the flexural strength of the cementitious composites.

At 0.3-wt% concentration, the effect of SMS on the flexural strength is diminished. This is probably due to the formation of weak zones in the cement matrix created by the agglomeration of the SMS sheets [34]. In addition, recent studies have shown that when microsheets are used in cementitious materials in high concentrations, their high surface area and hydroxyl groups facilitate the agglomeration of the cement particles and the formation of a flocculation structure within the matrix [35,36]. These effects inhibit the efficiency of microsheets in enhancing the performance of cementitious materials.

#### **4. Conclusion**

This research investigated the influence of new SMS sheets on the hydration kinetics of cement using a combination of CV and EIS coupled with analytical characterization tools. The low cost and environmentally friendly SMS material was derived from beet pulp, a by-product of sugar manufacturing. The results revealed that the large specific area and the number of reactive functional groups enable the SMS sheets to perform two hydration functions in cementitious materials that had not been observed before. The first function is the rapid hydroxylation of  $C_3S$  resulting from the dissolution of the SMS inner layers. The second function is the transport of water molecules from the pore solution to the unhydrated cement cores through the SMS layers that remained embedded in the hydration phases. These two hydration functions amplified the degree of hydration of cement and increased the amount of the hydration phases. Furthermore, The CV capacitance and the EIS electrical resistance of the cementitious composites correlated well with the change in the  $Ca(OH)_2$  content and DOH. As a result, the combined CV and EIS can be used to understand complex hydration kinetics of

cementitious materials infused with nano additives and monitor the evolution of their hydration phases.

The workability of the cement pastes was not affected by the addition of SMS when the dosage is between 0.1 and 0.3-wt%. The workability, however, decreased significantly at higher SMS dosages. The maximum percentage decrease was 96.05% at a SMS dosage of 0.6-wt%. [This can be attributed to the hydrophilic functional groups on the surfaces of SMS.](#) This reduces the free water in the cement paste which in return reduces its workability. The more SMS is added, the more the free water is reduced.

The mechanical properties of the cementitious composites were improved by the incorporation of SMS. However, this improvement is more pronounced in the flexural strength, indicating that SMS is more effective in improving the flexural strength than the compressive strength. At 28 days, the three SMS dosages produced somewhat similar compressive strength increases, around 8.33%, whereas 0.2-wt% produced the highest flexural strength increase of 31.56%. This is attributed to the higher degree of hydration and the improved strengthening effect resulting from the good SMS/matrix chemical bonding and mechanical interlocking, and crack-bridging mechanisms. The characteristics of the SMS-cementitious composites presented in this paper will help design concretes with improved engineering properties and lower carbon footprint for sustainable construction of infrastructure.

### **Acknowledgments**

This research work is financially supported by the Scientific Research Found of Hunan Provincial Education Department of China (22B0473), the European Commission Horizon 2020 Marie Skłodowska-Curie Research Grant (B-SMART 799658).

## Reference

- [1] G. Habert, D. Arribe, T. Dehove, L. Espinasse, R. Le Roy, Reducing environmental impact by increasing the strength of concrete: Quantification of the improvement to concrete bridges, *J. Clean. Prod.* 35 (2012) 250–262. <https://doi.org/10.1016/j.jclepro.2012.05.028>.
- [2] X. Wang, M.-Z. Guo, T.-C. Ling, Review on CO<sub>2</sub> curing of non-hydraulic calcium silicates cements: Mechanism, carbonation and performance, *Cem. Concr. Compos.* 133 (2022) 104641. <https://doi.org/10.1016/j.cemconcomp.2022.104641>.
- [3] S. Fang, L. Li, Z. Luo, Z. Fang, D. Huang, F. Liu, H. Wang, Z. Xiong, Novel FRP interlocking multi-spiral reinforced-seawater sea-sand concrete square columns with longitudinal hybrid FRP–steel bars: Monotonic and cyclic axial compressive behaviours, *Compos. Struct.* 305 (2023) 116487.
- [4] C. Zhou, J. Wang, X. Shao, L. Li, J. Sun, X. Wang, The feasibility of using ultra-high performance concrete (UHPC) to strengthen RC beams in torsion, *J. Mater. Res. Technol.* 24 (2023) 9961–9983. <https://doi.org/10.1016/j.jmrt.2023.05.185>.
- [5] Z. Xiong, L. Lin, S. Qiao, L. Li, Y. Li, S. He, Z. Li, F. Liu, Y. Chen, Axial performance of seawater sea-sand concrete columns reinforced with basalt fibre-reinforced polymer bars under concentric compressive load, *J. Build. Eng.* 47 (2022) 103828. <https://doi.org/10.1016/j.jobbe.2021.103828>.
- [6] C. Zhou, J. Wang, W. Jia, Z. Fang, Torsional behavior of ultra-high performance concrete (UHPC) rectangular beams without steel reinforcement: Experimental investigation and theoretical analysis, *Compos. Struct.* 299 (2022) 116022. <https://doi.org/10.1016/j.compstruct.2022.116022>.
- [7] K.A. Ali, M.I. Ahmad, Y. Yusup, Issues, impacts, and mitigations of carbon dioxide emissions in the building sector, *Sustain.* 12 (2020). <https://doi.org/10.3390/SU12187427>.
- [8] S.A. Miller, The role of cement service-life on the efficient use of resources, *Environ. Res. Lett.* 15 (2020). <https://doi.org/10.1088/1748-9326/ab639d>.
- [9] Z. Xiong, W. Wei, S. He, F. Liu, H. Luo, L. Li, Dynamic bond behaviour of fibre-wrapped basalt fibre-reinforced polymer bars embedded in sea sand and recycled aggregate concrete under high-strain rate pull-out tests, *Constr. Build. Mater.* 276 (2021) 122195. <https://doi.org/10.1016/j.conbuildmat.2020.122195>.
- [10] F. Torabian Isfahani, W. Li, E. Redaelli, Dispersion of multi-walled carbon nanotubes and its effects on the properties of cement composites, *Cem. Concr. Compos.* 74 (2016) 154–163. <https://doi.org/10.1016/j.cemconcomp.2016.09.007>.
- [11] W. Meng, K.H. Khayat, Effect of graphite nanoplatelets and carbon nanofibers on rheology, hydration, shrinkage, mechanical properties, and microstructure of UHPC, *Cem. Concr. Res.* 105 (2018) 64–71. <https://doi.org/10.1016/j.cemconres.2018.01.001>.
- [12] Z.S. Metaxa, M.S. Konsta-Gdoutos, S.P. Shah, Carbon nanofiber cementitious composites: Effect of debulking procedure on dispersion and reinforcing

- efficiency, *Cem. Concr. Compos.* 36 (2013) 25–32.  
<https://doi.org/10.1016/j.cemconcomp.2012.10.009>.
- [13] M. Tafesse, H.-K. Kim, The role of carbon nanotube on hydration kinetics and shrinkage of cement composite, *Compos. Part B Eng.* 169 (2019) 55–64.
- [14] Y. Sargam, K. Wang, Hydration kinetics and activation energy of cement pastes containing various nanoparticles, *Compos. Part B Eng.* 216 (2021) 108836.  
<https://doi.org/10.1016/j.compositesb.2021.108836>.
- [15] A.J.N. MacLeod, F.G. Collins, W. Duan, Effects of carbon nanotubes on the early-age hydration kinetics of Portland cement using isothermal calorimetry, *Cem. Concr. Compos.* 119 (2021) 103994.  
<https://doi.org/10.1016/j.cemconcomp.2021.103994>.
- [16] M.I. Haque, W. Ashraf, R.I. Khan, S. Shah, A comparative investigation on the effects of nanocellulose from bacteria and plant-based sources for cementitious composites, *Cem. Concr. Compos.* 125 (2022) 104316.  
<https://doi.org/10.1016/j.cemconcomp.2021.104316>.
- [17] Z. Pan, L. He, L. Qiu, A.H. Korayem, G. Li, J.W. Zhu, F. Collins, D. Li, W.H. Duan, M.C. Wang, Mechanical properties and microstructure of a graphene oxide-cement composite, *Cem. Concr. Compos.* 58 (2015) 140–147.  
<https://doi.org/10.1016/j.cemconcomp.2015.02.001>.
- [18] M. Krystek, D. Pakulski, V. Patroniak, M. Górski, L. Szojda, A. Ciesielski, P. Samorì, High-Performance Graphene-Based Cementitious Composites, *Adv. Sci.* (2019). <https://doi.org/10.1002/advs.201801195>.
- [19] M.A. Rafiee, T.N. Narayanan, D.P. Hashim, N. Sakhavand, R. Shahsavari, R. Vajtai, P.M. Ajayan, Hexagonal boron nitride and graphite oxide reinforced multifunctional porous cement composites, *Adv. Funct. Mater.* 23 (2013) 5624–5630. <https://doi.org/10.1002/adfm.201203866>.
- [20] T. Fu, F. Montes, P. Suraneni, J. Youngblood, J. Weiss, The influence of cellulose nanocrystals on the hydration and flexural strength of Portland cement pastes, *Polymers (Basel)*. 9 (2017). <https://doi.org/10.3390/polym9090424>.
- [21] S.A. Ghahari, L.N. Assi, A. Alsalman, K.E. Alyamaç, Fracture properties evaluation of cellulose nanocrystals cement paste, *Materials (Basel)*. 13 (2020). <https://doi.org/10.3390/ma13112507>.
- [22] Y. Cao, P. Zavattieri, J. Youngblood, R. Moon, J. Weiss, The relationship between cellulose nanocrystal dispersion and strength, *Constr. Build. Mater.* 119 (2016) 71–79. <https://doi.org/10.1016/j.conbuildmat.2016.03.077>.
- [23] E.G. Deze, E. Cuenca, A.M.L. Násner, M. Iakovlev, S. Sideri, A. Sapolidis, R.P. Borg, L. Ferrara, Nanocellulose enriched mortars: Evaluation of nanocellulose properties affecting microstructure, strength and development of mixing protocols, *Mater. Today Proc.* 54 (2021) 50–56.  
<https://doi.org/10.1016/j.matpr.2021.09.511>.
- [24] G. Long, Y. Li, C. Ma, Y. Xie, Y. Shi, Hydration kinetics of cement incorporating different nanoparticles at elevated temperatures, *Thermochim. Acta.* 664 (2018) 108–117. <https://doi.org/10.1016/j.tca.2018.04.017>.

- [25] K. Mei, Z. He, B. Yi, X. Lin, J. Wang, H. Wang, J. Liu, Study on electrochemical characteristics of reinforced concrete corrosion under the action of carbonation and chloride, *Case Stud. Constr. Mater.* 17 (2022) e01351. <https://doi.org/10.1016/j.cscm.2022.e01351>.
- [26] A. Kruk, D. Madej, A new approach to time-resolved electrochemical impedance spectroscopy using the Impedance Camera to track fast hydration processes in cement-based materials, *Meas. J. Int. Meas. Confed.* 205 (2022) 112199. <https://doi.org/10.1016/j.measurement.2022.112199>.
- [27] X.R. Nóvoa, Electrochemical aspects of the steel- concrete system. A review, *J. Solid State Electrochem.* 20 (2016) 2113–2125. <https://doi.org/10.1007/s10008-016-3238-z>.
- [28] R. Wang, F. He, C. Shi, D. Zhang, C. Chen, L. Dai, AC impedance spectroscopy of cement - based materials: measurement and interpretation, *Cem. Concr. Compos.* 131 (2022) 104591. <https://doi.org/10.1016/j.cemconcomp.2022.104591>.
- [29] B. Huang, J. Wang, G. Piukovics, N. Zabihi, J. Ye, M. Saafi, J. Ye, Hybrid cement composite-based sensor for in-situ chloride monitoring in concrete structures, *Sensors Actuators B Chem.* 385 (2023) 133638. <https://doi.org/10.1016/j.snb.2023.133638>.
- [30] Q. Liu, H. Tang, L. Chi, K. Chen, L. Zhang, C. Lu, Evolution of Electrochemical Impedance Spectra Characteristics of Cementitious Materials after Capturing Carbon Dioxide, *Sustainability.* 15 (2023) 2460.
- [31] S. Wang, J. Zhang, O. Gharbi, V. Vivier, M. Gao, M.E. Orazem, Electrochemical impedance spectroscopy, *Nat. Rev. Methods Prim.* 1 (2021). <https://doi.org/10.1038/s43586-021-00039-w>.
- [32] X. Hu, C. Shi, X. Liu, J. Zhang, G. De Schutter, A review on microstructural characterization of cement-based materials by AC impedance spectroscopy, *Cem. Concr. Compos.* 100 (2019) 1–14.
- [33] N. Elgrishi, K.J. Rountree, B.D. McCarthy, E.S. Rountree, T.T. Eisenhart, J.L. Dempsey, A Practical Beginner's Guide to Cyclic Voltammetry, *J. Chem. Educ.* 95 (2018) 197–206. <https://doi.org/10.1021/acs.jchemed.7b00361>.
- [34] H. Hasan, B. Huang, M. Saafi, J. Sun, Y. Chi, E. Whale, D. Hepworth, J. Ye, Novel engineered high performance sugar beetroot 2D nanoplatelet-cementitious composites, *Constr. Build. Mater.* 202 (2019) 546–562. <https://doi.org/10.1016/j.conbuildmat.2019.01.019>.
- [35] Y. Chi, B. Huang, M. Saafi, J. Ye, C. Lambert, Carrot-based covalently bonded saccharides as a new 2D material for healing defective calcium-silicate-hydrate in cement: Integrating atomistic computational simulation with experimental studies, *Compos. Part B Eng.* 199 (2020) 108235.
- [36] Y. Chi, B. Huang, M. Saafi, N. Fullwood, C. Lambert, E. Whale, D. Hepworth, J. Ye, 2D bio-based nanomaterial as a green route to amplify the formation of hydrate phases of cement composites: Atomistic simulations and analytical characterization, *Constr. Build. Mater.* 299 (2021) 123867. <https://doi.org/10.1016/j.conbuildmat.2021.123867>.

- [37] D. Hepworth, E. Whale, Cellulose platelet compositions, methods of preparing cellulose platelet compositions and products comprising same, US 9,834,664 B2, 2017.
- [38] P. Payakaniti, S. Pinitsoontorn, P. Thongbai, V. Amornkitbamrung, P. Chindaprasirt, Electrical conductivity and compressive strength of carbon fiber reinforced fly ash geopolymeric composites, *Constr. Build. Mater.* 135 (2017) 164–176.
- [39] İ. Şanal, N.Ö. Zihnioğlu, A. Hosseini, Particle image velocimetry (PIV) to evaluate fresh and hardened state properties of self compacting fiber-reinforced cementitious composites (SC-FRCCs), *Constr. Build. Mater.* 78 (2015) 450–463.
- [40] Y. Cao, N. Tian, D. Bahr, P.D. Zavattieri, J. Youngblood, R.J. Moon, J. Weiss, The influence of cellulose nanocrystals on the microstructure of cement paste, *Cem. Concr. Compos.* 74 (2016) 164–173. <https://doi.org/10.1016/j.cemconcomp.2016.09.008>.
- [41] F. Rajabipour, G. Sant, J. Weiss, Interactions between shrinkage reducing admixtures (SRA) and cement paste's pore solution, *Cem. Concr. Res.* 38 (2008) 606–615. <https://doi.org/10.1016/j.cemconres.2007.12.005>.
- [42] I. Pane, W. Hansen, Investigation of blended cement hydration by isothermal calorimetry and thermal analysis, *Cem. Concr. Res.* 35 (2005) 1155–1164. <https://doi.org/10.1016/j.cemconres.2004.10.027>.
- [43] A. ASTM, Standard test method for compressive strength of hydraulic cement mortars (using 2-in. or [50-mm] cube specimens), *Annu. B. ASTM Stand. B. ASTM Stand.* 4 (2013) 1–9.
- [44] C. ASTM, Standard test method for flexural strength of concrete (using simple beam with third-point loading), in: *Am. Soc. Test. Mater.*, 2010: pp. 12959–19428.
- [45] D. Ciolacu, F. Ciolacu, V.I. Popa, Amorphous cellulose—structure and characterization, *Cellul. Chem. Technol.* 45 (2011) 13.
- [46] H. Yang, R. Yan, H. Chen, D.H. Lee, C. Zheng, Characteristics of hemicellulose, cellulose and lignin pyrolysis, *Fuel.* 86 (2007) 1781–1788. <https://doi.org/10.1016/j.fuel.2006.12.013>.
- [47] H.M. Ng, L.T. Sin, T.T. Tee, S.T. Bee, D. Hui, C.Y. Low, A.R. Rahmat, Extraction of cellulose nanocrystals from plant sources for application as reinforcing agent in polymers, *Compos. Part B Eng.* 75 (2015) 176–200. <https://doi.org/10.1016/j.compositesb.2015.01.008>.
- [48] C.A. Guerrero-Fajardo, L. Giraldo, J.C. Moreno-Piraján, Preparation and characterization of graphene oxide for Pb(II) and Zn(II) ions adsorption from aqueous solution: Experimental, thermodynamic and kinetic study, *Nanomaterials.* 10 (2020). <https://doi.org/10.3390/nano10061022>.
- [49] A.I. Al-Hadithi, N.N. Hilal, The possibility of enhancing some properties of self-compacting concrete by adding waste plastic fibers, *J. Build. Eng.* 8 (2016) 20–28. <https://doi.org/10.1016/j.jobbe.2016.06.011>.

- [50] A. Alzaza, K. Ohenoja, V. Isteri, T. Hanein, D. Geddes, M. Poikelispää, M. Illikainen, Blending eco-efficient calcium sulfoaluminate belite ferrite cement to enhance the physico-mechanical properties of Portland cement paste cured in refrigerated and natural winter conditions, *Cem. Concr. Compos.* 129 (2022). <https://doi.org/10.1016/j.cemconcomp.2022.104469>.
- [51] F. Wang, X. Kong, L. Jiang, D. Wang, The acceleration mechanism of nano-C-S-H particles on OPC hydration, *Constr. Build. Mater.* 249 (2020) 118734. <https://doi.org/10.1016/j.conbuildmat.2020.118734>.
- [52] L. Yan, B. Kasal, L. Huang, A review of recent research on the use of cellulosic fibres, their fibre fabric reinforced cementitious, geo-polymer and polymer composites in civil engineering, *Compos. Part B Eng.* 92 (2016) 94–132. <https://doi.org/10.1016/j.compositesb.2016.02.002>.
- [53] J. Tao, N. Liu, L. Li, J. Su, Y. Gao, Hierarchical nanostructures of polypyrrole@MnO<sub>2</sub> composite electrodes for high performance solid-state asymmetric supercapacitors, *Nanoscale.* 6 (2014) 2922–2928. <https://doi.org/10.1039/c3nr05845j>.
- [54] R.F. Harrington, Introduction to electromagnetic engineering, Courier Corporation, 2003.
- [55] A. Shodiev, M. Chouchane, M. Gaberscek, O. Arcelus, J. Xu, H. Oularbi, J. Yu, J. Li, M. Morcrette, A.A. Franco, Deconvoluting the benefits of porosity distribution in layered electrodes on the electrochemical performance of Li-ion batteries, *Energy Storage Mater.* 47 (2022) 462–471. <https://doi.org/10.1016/j.ensm.2022.01.058>.
- [56] M. Nagao, K. Kobayashi, Y. Jin, I. Maruyama, T. Hibino, Ionic conductive and photocatalytic properties of cementitious materials: Calcium silicate hydrate and calcium aluminoferrite, *J. Mater. Chem. A.* 8 (2020) 15157–15166. <https://doi.org/10.1039/d0ta04866f>.
- [57] K.A. Snyder, X. Feng, B.D. Keen, T.O. Mason, Estimating the electrical conductivity of cement paste pore solutions from OH<sup>-</sup>, K<sup>+</sup> and Na<sup>+</sup> concentrations, *Cem. Concr. Res.* 33 (2003) 793–798. [https://doi.org/10.1016/S0008-8846\(02\)01068-2](https://doi.org/10.1016/S0008-8846(02)01068-2).
- [58] X. Xi, M. Ozturk, D.D.L. Chung, DC electric polarization of cured cement paste being unexpectedly hindered by free water, *J. Am. Ceram. Soc.* 105 (2022) 1074–1082. <https://doi.org/10.1111/jace.18121>.
- [59] S. Wen, D.D.L. Chung, Effect of admixtures on the dielectric constant of cement paste, *Cem. Concr. Res.* 31 (2001) 673–677. [https://doi.org/10.1016/S0008-8846\(01\)00475-6](https://doi.org/10.1016/S0008-8846(01)00475-6).
- [60] P. Krishnaveni, V. Ganesh, Electron transfer studies of a conventional redox probe in human sweat and saliva bio-mimicking conditions, *Sci. Rep.* 11 (2021) 1–13. <https://doi.org/10.1038/s41598-021-86866-z>.
- [61] E.P. Randviir, C.E. Banks, Electrochemical impedance spectroscopy: An overview of bioanalytical applications, *Anal. Methods.* 5 (2013) 1098–1115. <https://doi.org/10.1039/c3ay26476a>.

- [62] Y. Yang, R.A. Patel, S. V. Churakov, N.I. Prasianakis, G. Kosakowski, M. Wang, Multiscale modeling of ion diffusion in cement paste: electrical double layer effects, *Cem. Concr. Compos.* 96 (2019) 55–65. <https://doi.org/10.1016/j.cemconcomp.2018.11.008>.
- [63] D. Lau, W. Jian, Z. Yu, D. Hui, Nano-engineering of construction materials using molecular dynamics simulations: Prospects and challenges, *Compos. Part B Eng.* 143 (2018) 282–291. <https://doi.org/10.1016/j.compositesb.2018.01.014>.
- [64] H. Deng, Z. He, Interactions of sodium chloride solution and calcium silicate hydrate with different calcium to silicon ratios: A molecular dynamics study, *Constr. Build. Mater.* 268 (2021) 121067. <https://doi.org/10.1016/j.conbuildmat.2020.121067>.
- [65] W. Wang, P. Liu, M. Zhang, J. Hu, F. Xing, The Pore Structure of Phosphoaluminate Cement, *Open J. Compos. Mater.* 02 (2012) 104–112. <https://doi.org/10.4236/ojcm.2012.23012>.
- [66] J. Qin, F. Dai, H. Ma, X. Dai, Z. Li, X. Jia, J. Qian, Development and characterization of magnesium phosphate cement based ultra-high performance concrete, *Compos. Part B Eng.* 234 (2022) 109694. <https://doi.org/10.1016/j.compositesb.2022.109694>.
- [67] S. Wacharasindhu, S. Likitmaskul, L. Punnakanta, K. Chaichanwatanakul, K. Angsusingha, C. Tuchinda, REPORTING PHYSISORPTION DATA FOR GAS/SOLID SYSTEMS with Special Reference to the Determination of Surface Area and Porosity, *J. Med. Assoc. Thail.* 81 (1998) 420–430.
- [68] A. Anwar, B.S. Mohammed, M.A. Wahab, M.S. Liew, Enhanced properties of cementitious composite tailored with graphene oxide nanomaterial - A review, *Dev. Built Environ.* 1 (2020) 100002. <https://doi.org/10.1016/j.dibe.2019.100002>.
- [69] J. Tang, T. Yang, C. Yu, D. Hou, J. Liu, Precipitated calcium hydroxide morphology in nanoparticle suspensions: An experimental and molecular dynamics study, *Cem. Concr. Compos.* 94 (2018) 201–214. <https://doi.org/10.1016/j.cemconcomp.2018.09.004>.
- [70] I. Ismail, S.A. Bernal, J.L. Provis, S. Hamdan, J.S.J. Van Deventer, Drying-induced changes in the structure of alkali-activated pastes, *J. Mater. Sci.* 48 (2013) 3566–3577. <https://doi.org/10.1007/s10853-013-7152-9>.
- [71] D. Jansen, F. Goetz-Neunhoeffler, C. Stabler, J. Neubauer, A remastered external standard method applied to the quantification of early OPC hydration, *Cem. Concr. Res.* 41 (2011) 602–608. <https://doi.org/10.1016/j.cemconres.2011.03.004>.
- [72] S. Lv, Y. Ma, C. Qiu, T. Sun, J. Liu, Q. Zhou, Effect of graphene oxide nanosheets of microstructure and mechanical properties of cement composites, *Constr. Build. Mater.* 49 (2013) 121–127. <https://doi.org/10.1016/j.conbuildmat.2013.08.022>.
- [73] Q. Luo, Y.Y. Wu, W. Qiu, H. Huang, S. Pei, P. Lambert, D. Hui, Improving flexural strength of UHPC with sustainably synthesized graphene oxide, *Nanotechnol. Rev.* 10 (2021) 754–767. <https://doi.org/10.1515/ntrev-2021-0050>.

- [74] D. Hou, Z. Lu, X. Li, H. Ma, Z. Li, Reactive molecular dynamics and experimental study of graphene-cement composites: Structure, dynamics and reinforcement mechanisms, *Carbon N. Y.* 115 (2017) 188–208.

## Figure Captions

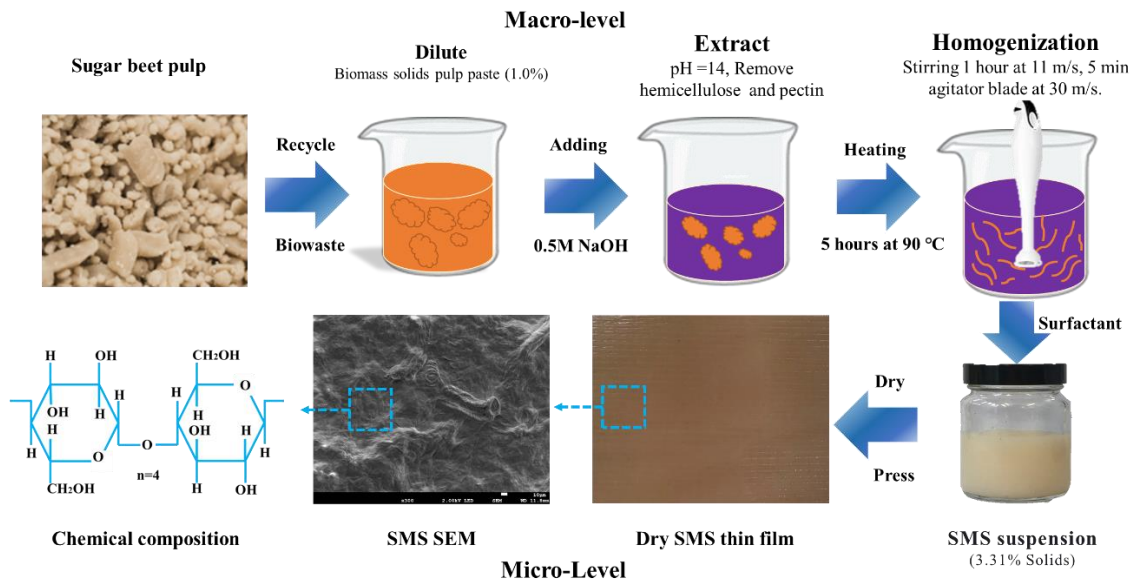


**Fig. 1.** Manufacturing process of the SMS sheets.

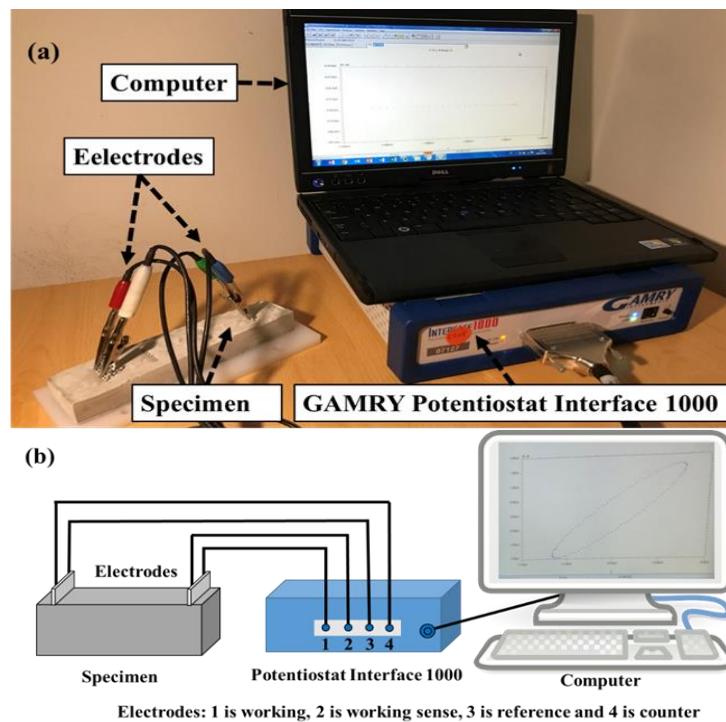


**Fig. 2.** Cyclic voltammetry and electrochemical impedance spectroscopy characterization.

(a) experiment setup, (b) schematic view of the setup.

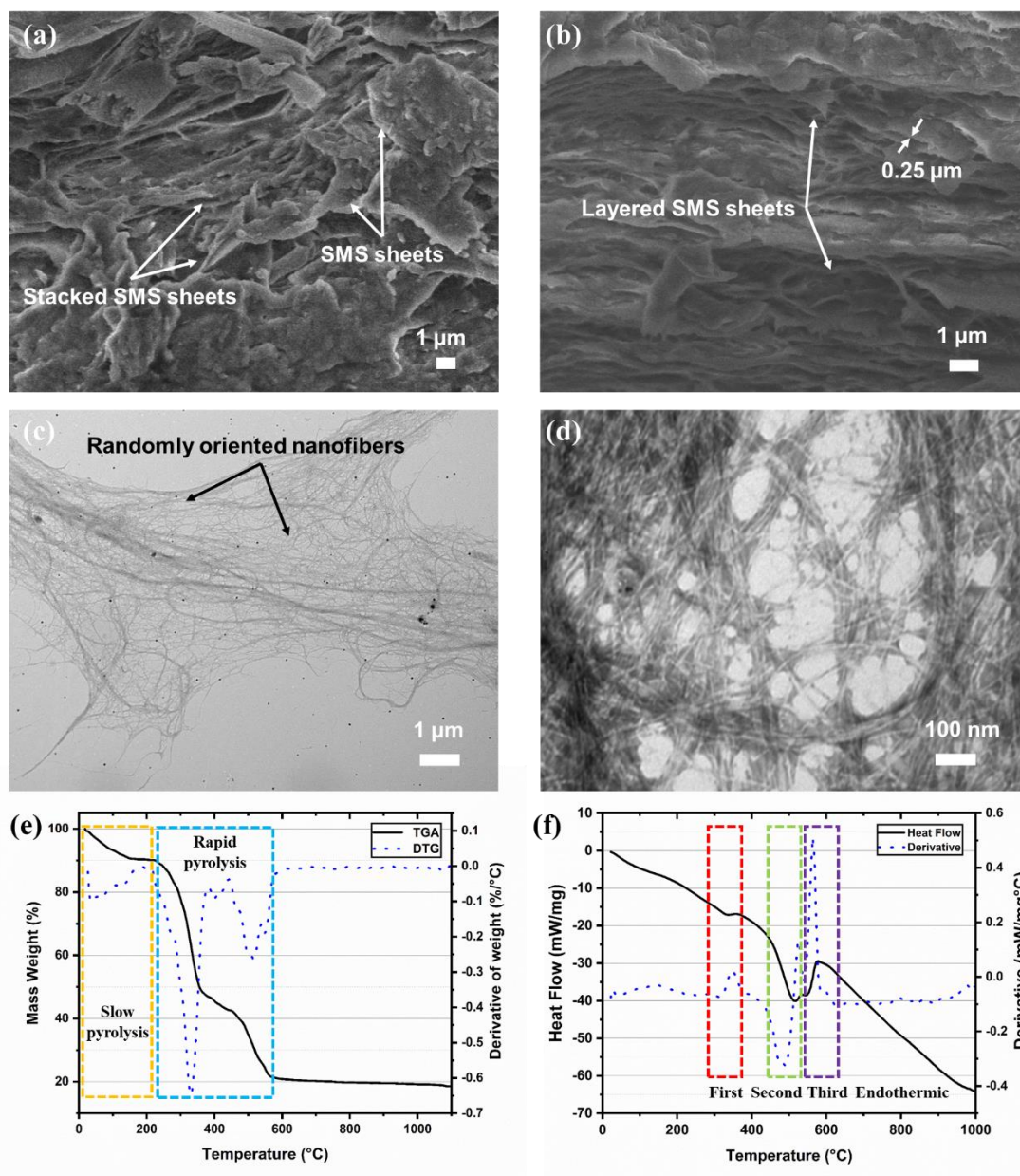


**Fig. 3.** Morphology and thermal properties of the SMS sheets. (a) surface morphology, (b) cross-section morphology, (c-d) TEM images, (e) TGA curve and its derivative, (f) DSC curve and its derivative.

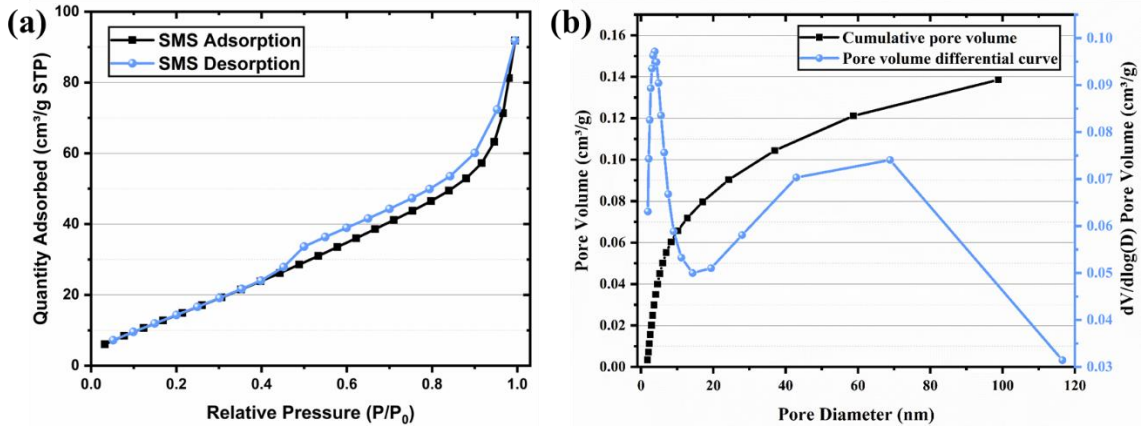


**Fig. 4.** Pore structure of SMS. (a) nitrogen sorption isotherm curves, (b) cumulative pore volume and pore distribution.

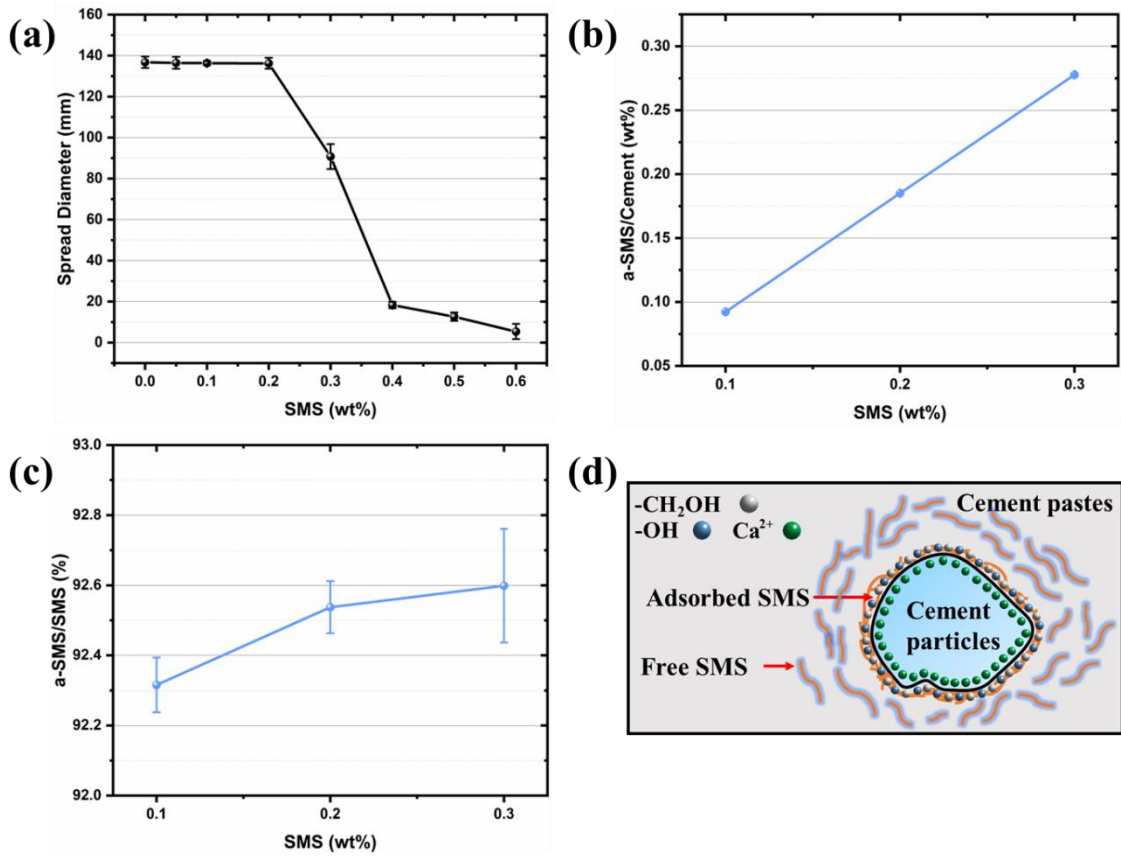


**Fig. 5.** Interaction of SMS with cement particles. (a) Mini-slump workability results, (b) per gram mass of a-SMS percentage out of cement, (c) per gram mass of a-SMS percentage out of SMS, (d) schematic of a-SMS and f-SMS in cement paste.

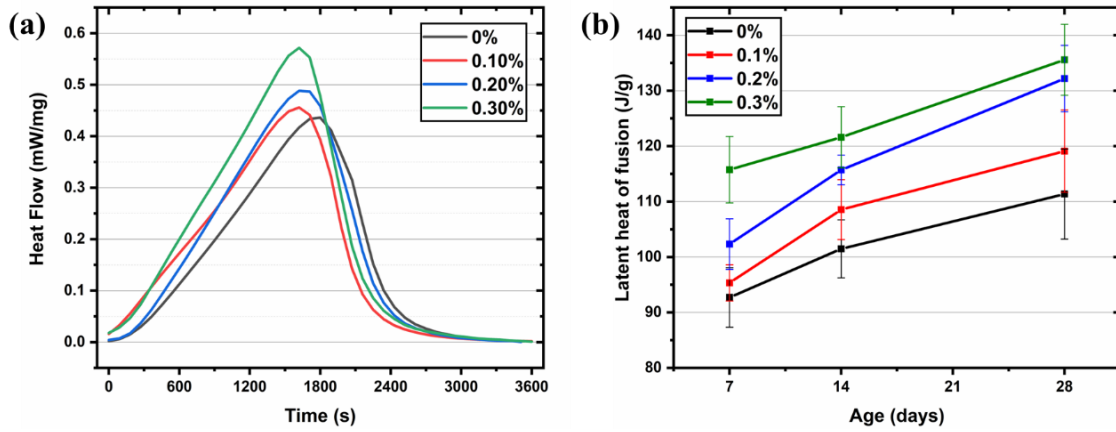


**Fig. 6.** Hydration heat of SMS-cementitious composites  $\text{Ca(OH)}_2$ . (a) effect of SMS on heat flow rate, (b) effect of curing age and SMS on latent heat of flow.

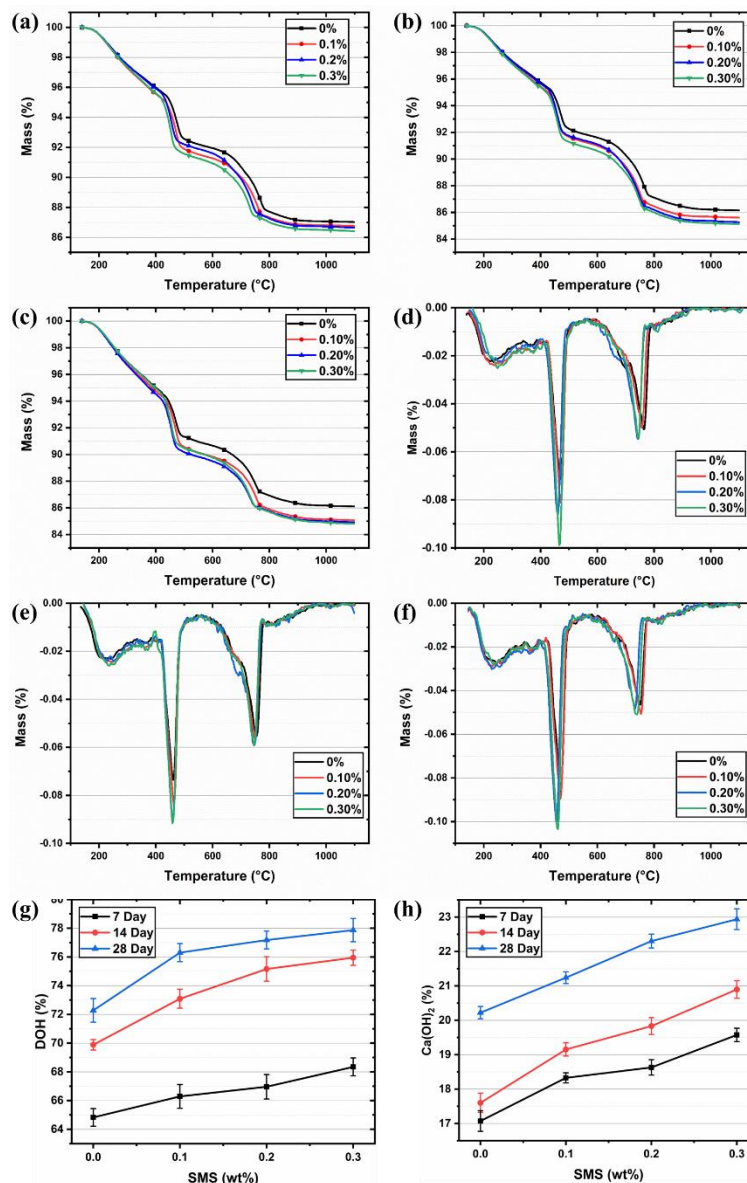


**Fig. 7.** Thermal behaviour of SMS-cementitious composites. (a) TGA curves at 7 days, (b) TGA curves at 14 days, (c) TGA curves at 28 days, (d) DTG curves at 7 days, (e) DTG curves at 14 days, (f) DTG curves at 28 days, (g) DOH content, (h)  $\text{Ca(OH)}_2$  content.

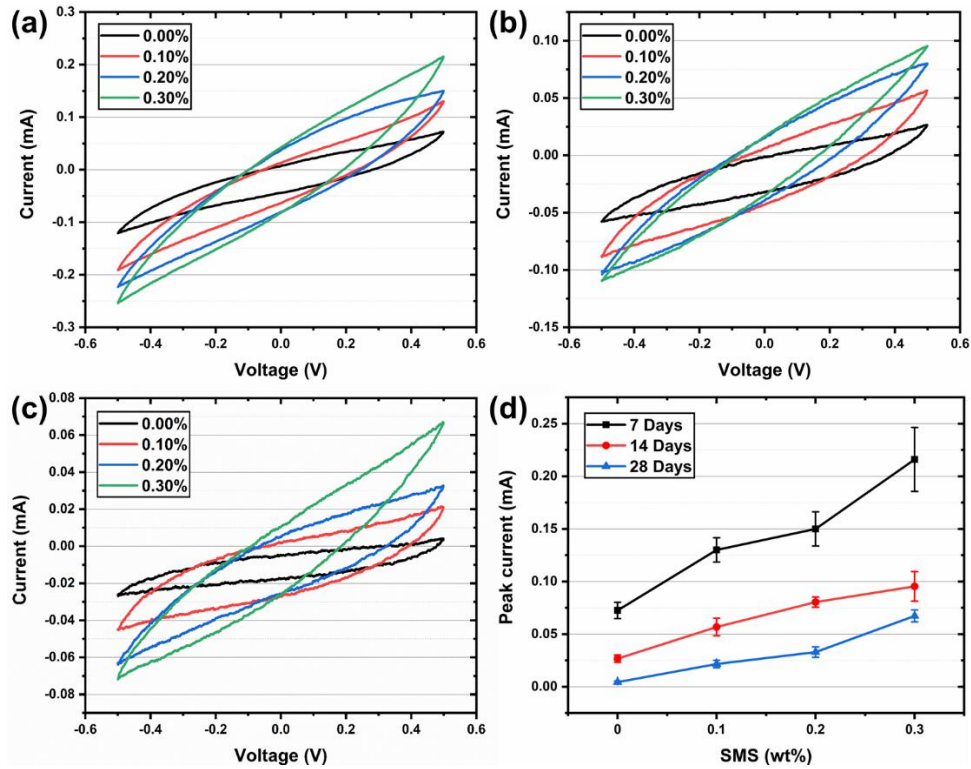


**Fig. 8.** CV-based electrochemical properties of SMS-cementitious composites. (a) CV curves at 7 days, (b) CV curves at 14 days, (c) CV curves at 28 days, (d) Peak current against SMS concentration.

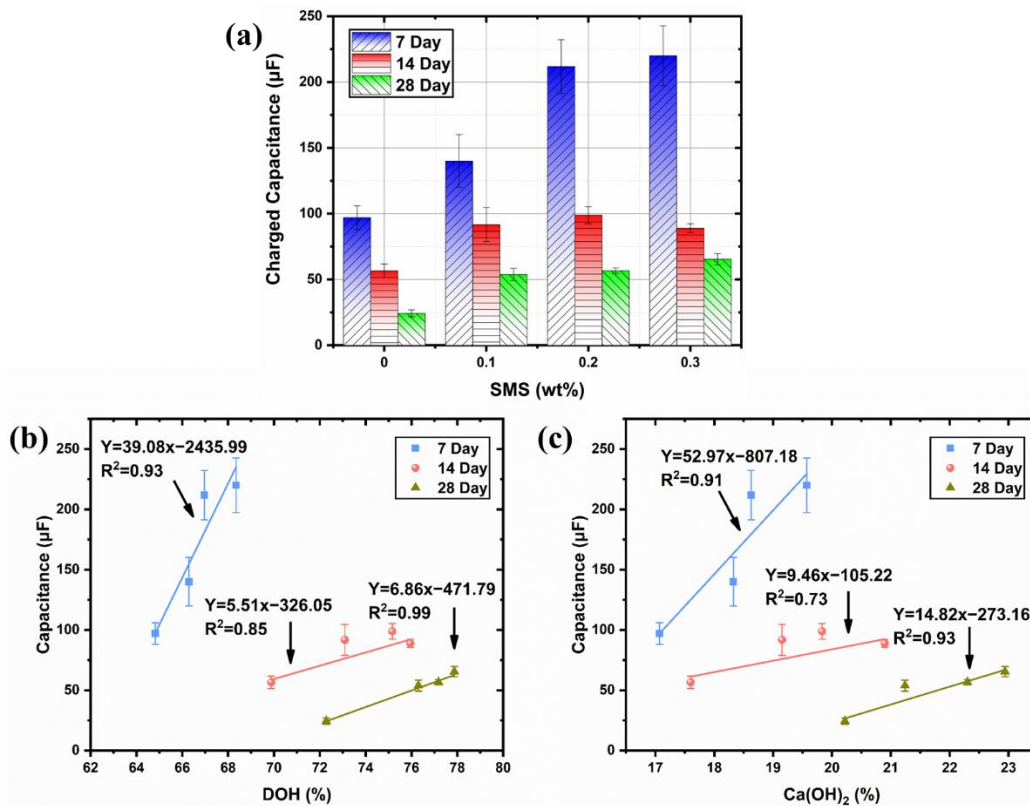


**Fig. 9.** Capacitance of the electrochemical SMS-cementitious composites. (a) capacitance against SMS concentration, (b) capacitance against DOH, (c) capacitance against  $\text{Ca(OH)}_2$  content.

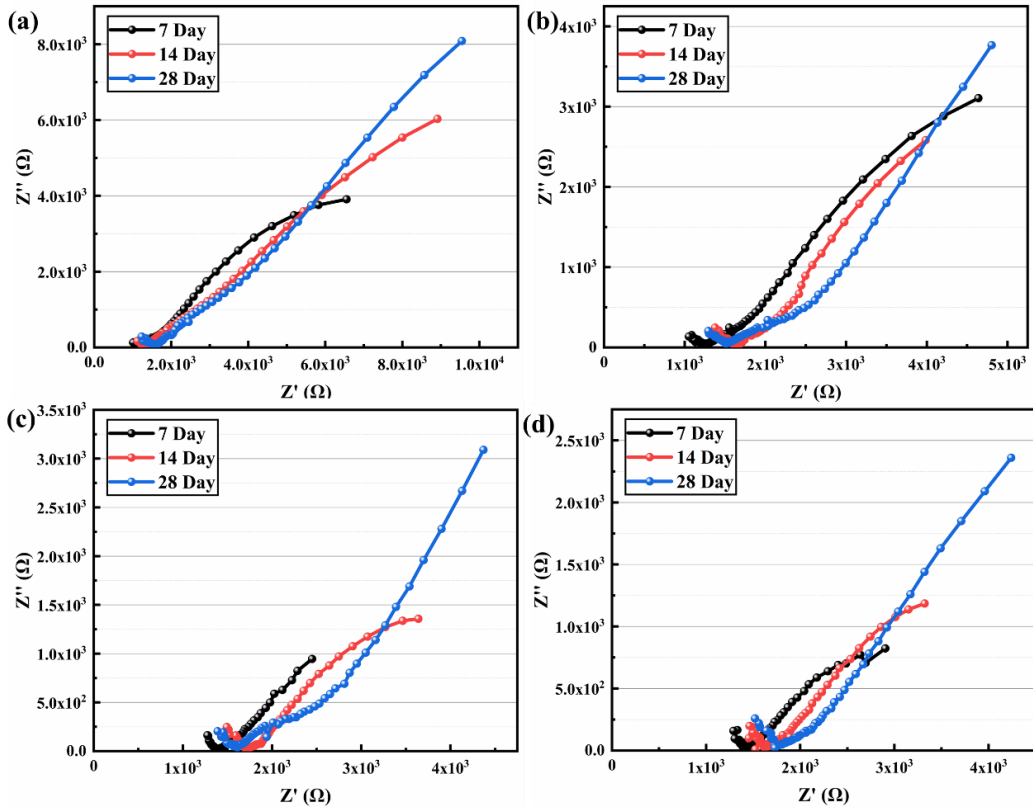


**Fig. 10.** Nyquist plots for the SMS-cementation composites at different curing ages. (a) paste with 0 wt%, (b) paste with 0.1 wt%, (c) paste with 0.2 wt%, (d) 0.3 wt%.

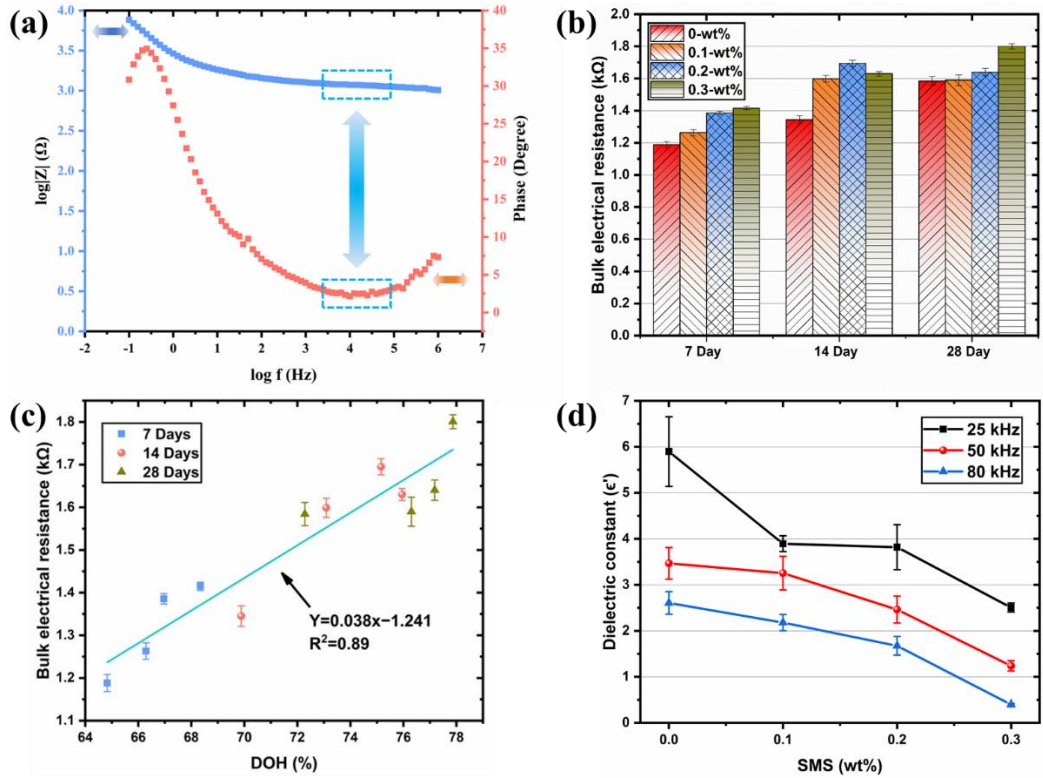


**Fig. 11.** EIS-based electrical properties of SMS-cementitious composites. (a) typical bode plot of impedance and phase for 0.1 wt% at 7 days, (b) bulk electrical resistance against curing age, (c) bulk electrical resistance against DOH at 7, 14 and 28 days, (d) dielectric constant against SMS concentration at 28 days.

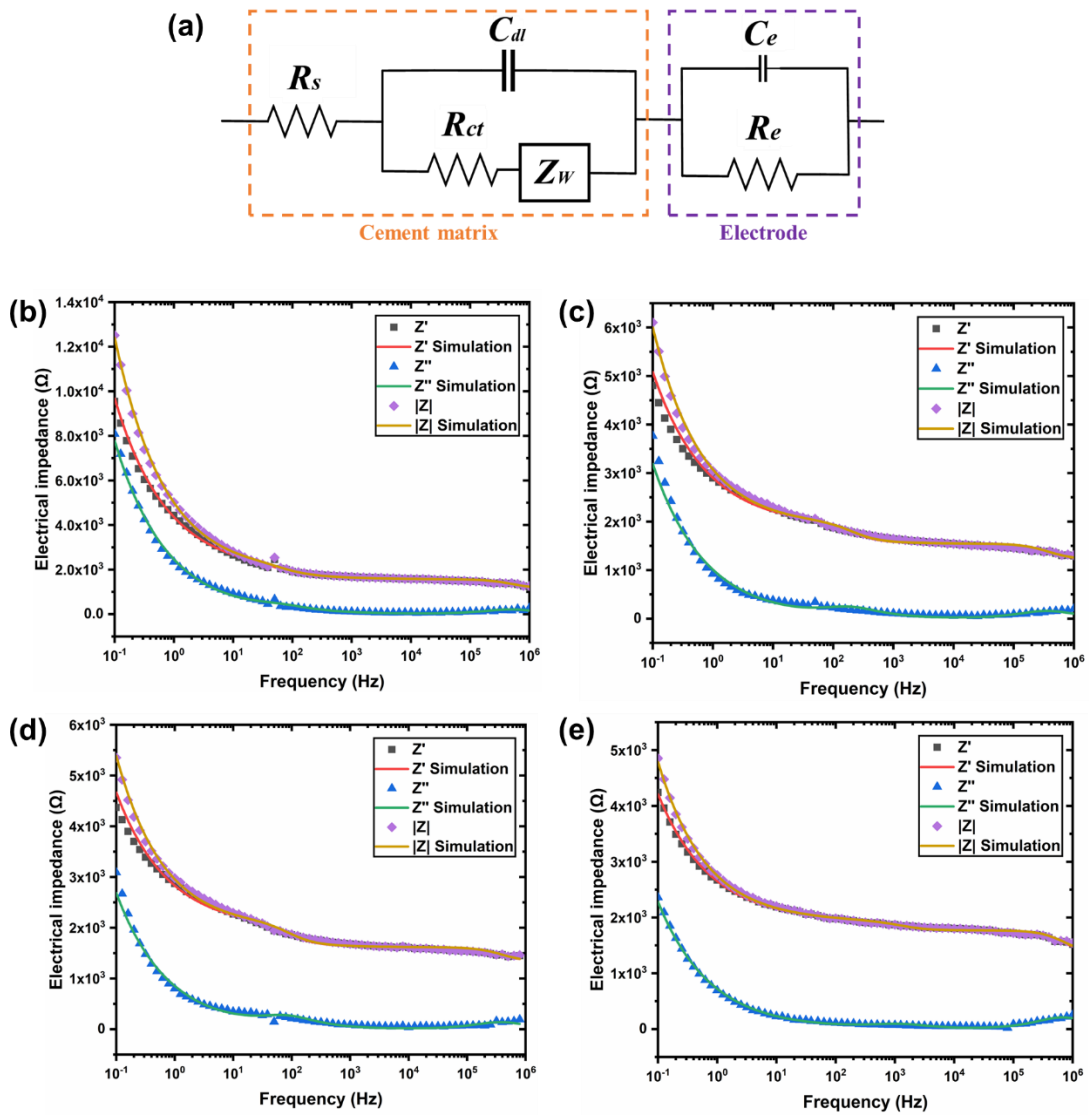


**Fig. 12.** Measured and fitted impedances of the cementitious composites at 28 days. (a) EC model, (b) 0% SMS, (c) 0.1-wt% SMS, (d) 0.2-wt% SMS, (e) 0.3-wt% SMS.

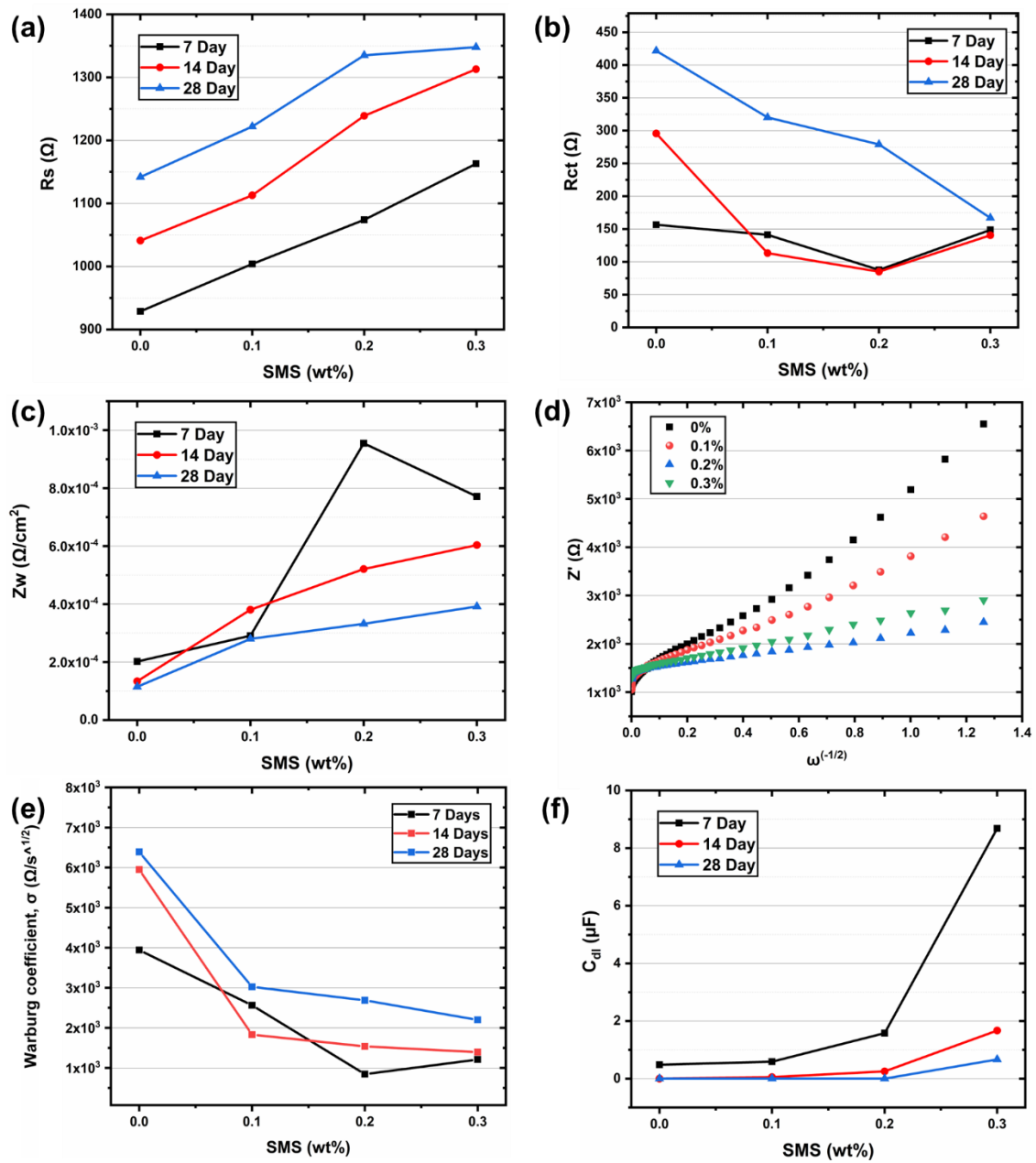


**Fig. 13.** EC parameter of the SMS-cementitious composites. (a) effect of SMS on  $R_s$ , (b) effect of SMS on  $R_{ct}$ , (c) effect of SMS on  $Z_w$ , (d) Warburg plots at 7 days, (e) Warburg coefficient against SMS concentration, (f) effect of SMS on  $C_{dl}$ .

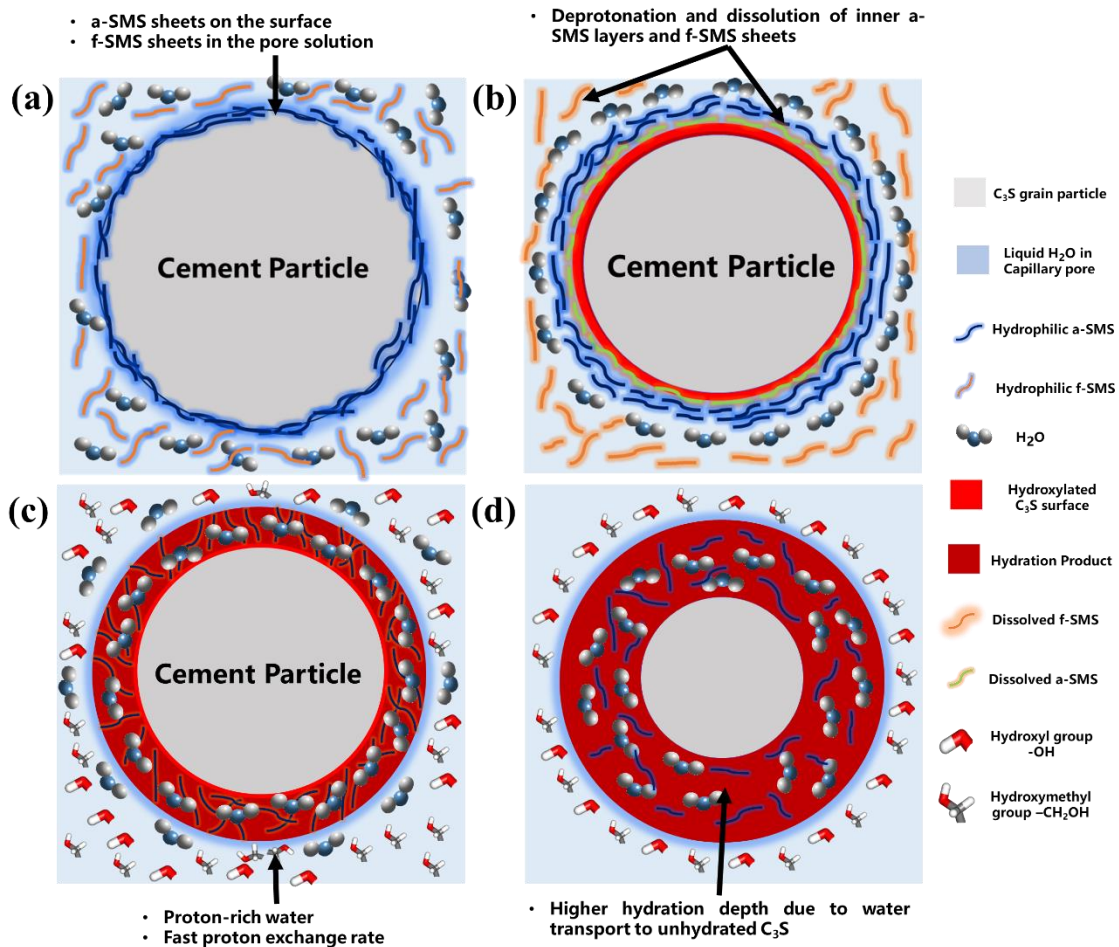


**Fig. 14.** Hydration kinetics of SMS-cementitious composites. (a) cement particle with a-SMS and f-SMS sheets in the pore solution, (b) breakage of H-bonds between (-OH/-CH<sub>2</sub>-OH) functional groups of SMS, and deprotonation and dissolution of the inner a-SMS layers, (c) formation of CH<sub>3</sub>OH and CH<sub>2</sub>H<sub>5</sub>OH, fast proton exchange and dissolution of C<sub>3</sub>S, (d) mechanism of water diffusion into the unhydrated C<sub>3</sub>S core and hydration growth.

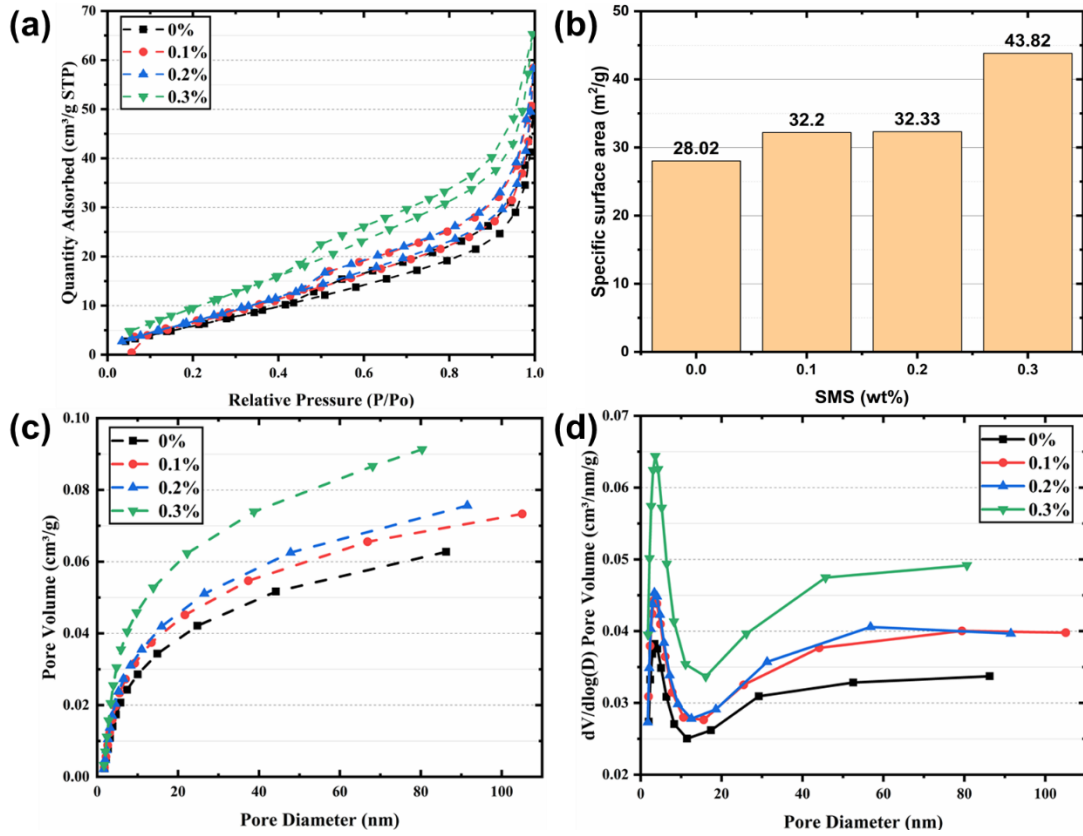


**Fig. 15.** Effect SMS on the porosity of the SMS-cementitious composites at 28 days. (a) BET isotherms, (b) specific surface area against SMS concentration, (c) cumulative pore volume against pore diameter, (d) pore size distribution.

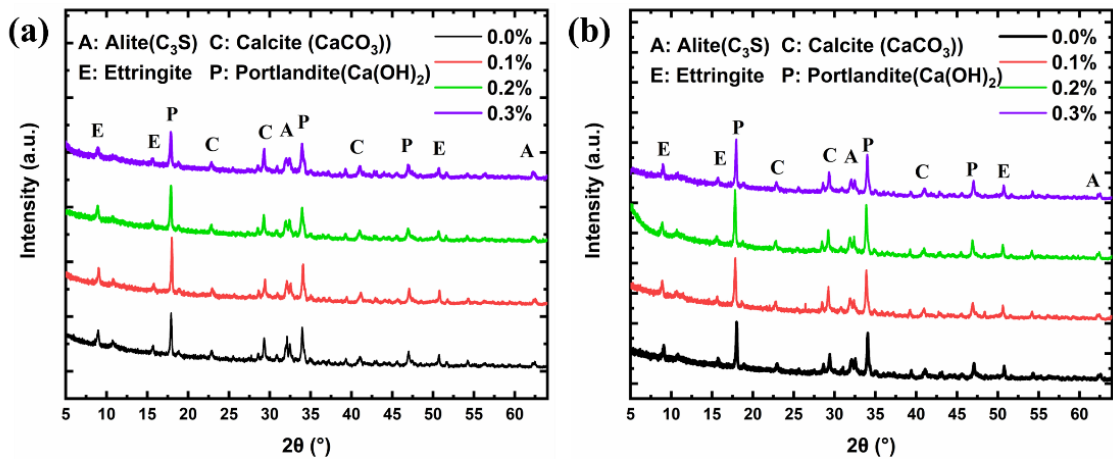


**Fig. 16.** XRD analysis ( $2\theta=5-65^\circ$ ) of cementitious composites with 0%, 0.1, 0.2 and 0.3-wt% amount of SMS at (a) 7 days, (b) 28 days.

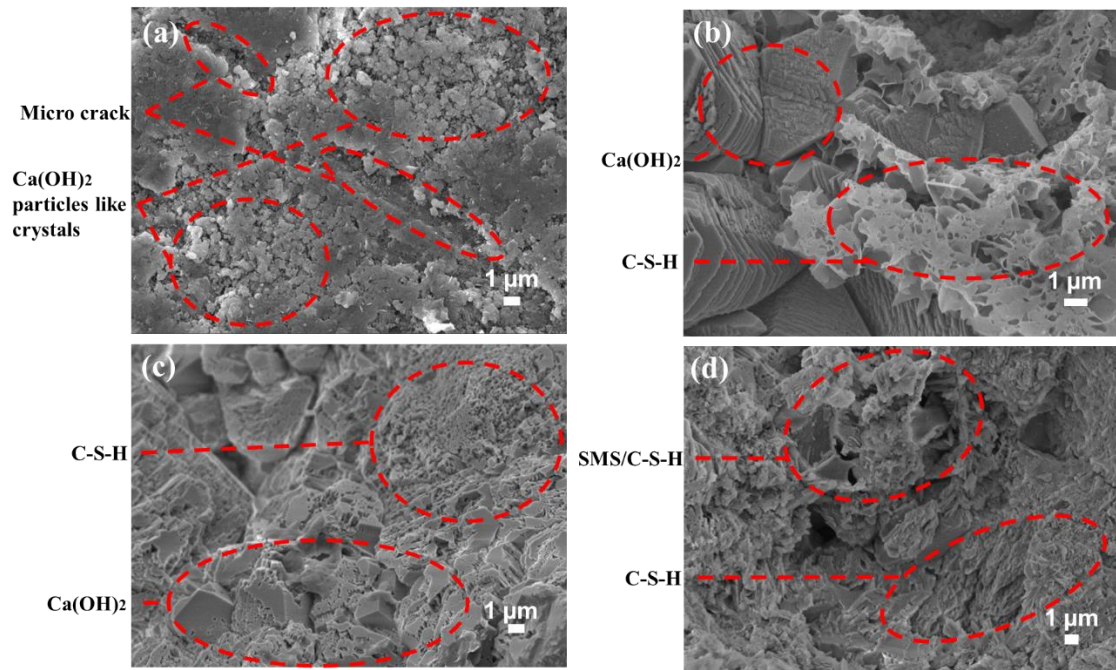


**Fig. 17.** SEM images of the SMS-cementitious composites at of 14 days (a) plain, (b) with 0.1wt%, (c) with 0.2 wt%, (d) with 0.3 wt%.

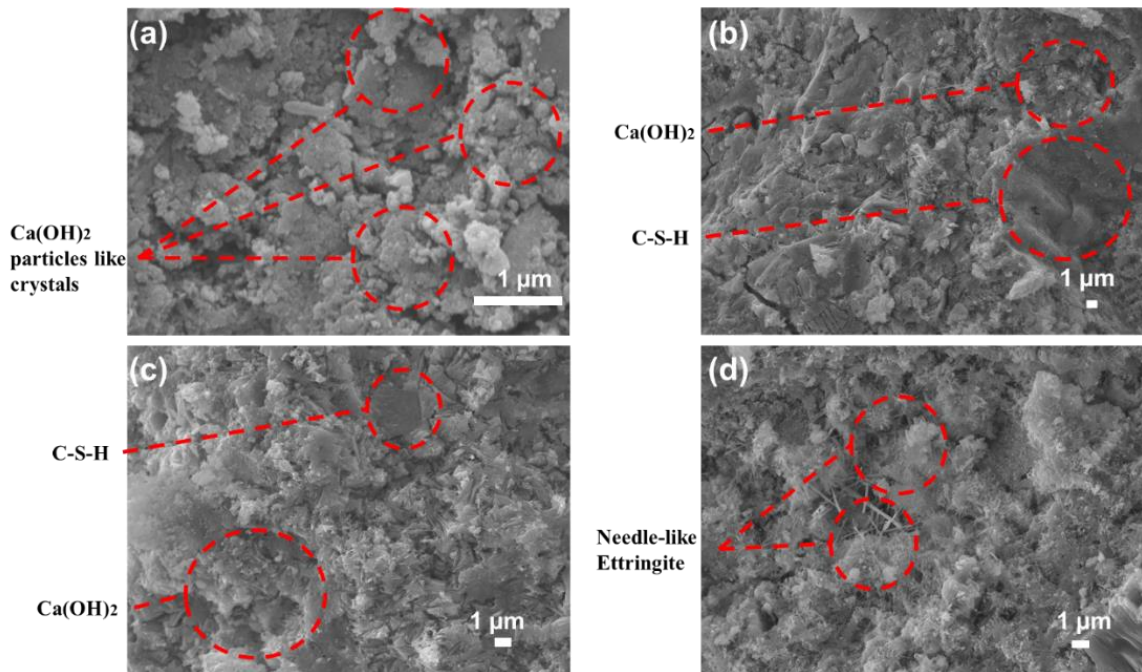


**Fig. 18.** SEM images of the SMS-cementitious composites at 28 days. (a) plain, (b) with 0.1 wt%, (c) with 0.2 wt%, (d) with 0.3 wt%.

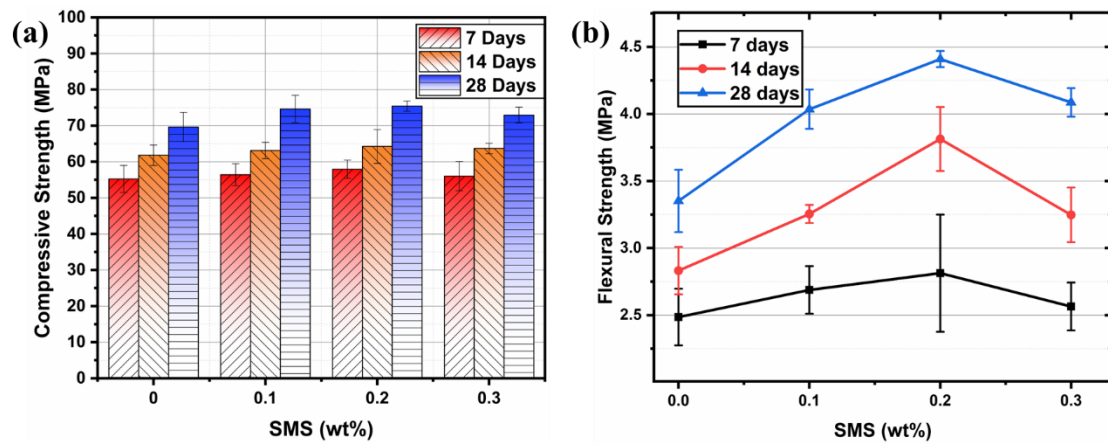


**Fig. 19.** SMS-cementitious composites at 7, 14 and 28 days. (a) Compressive strength, (b) flexural strength.

## Tables

Table 1: Fitting results for different SMS concentrations and curing ages

Day	SMS	$R_s$	$C_{dl}$	$R_{ct}$	$Z_w$	$C_e$	$R_e$
	(wt%)	( $\Omega$ )	( $\mu F$ )	( $\Omega$ )	( $\Omega/cm^2$ )	( $\mu F$ )	( $\Omega$ )
7	0	928.9	4.84E-01	156.5	2.02E-04	1.28E-03	231.6
	0.1	1004	5.92E-01	141.2	2.91E-04	1.58E-03	234.8
	0.2	1074	1.58	87.65	9.55E-04	4.70E-4	298.3
	0.3	1163	8.68	148.6	7.71E-04	7.53E-4	258.7
14	0	1041	1.30E-03	295.7	1.34E-04	7.42	337.4
	0.1	1113	5.39E-02	113.3	3.81E-04	3.22E-4	436.6
	0.2	1239	2.54E-01	84.95	5.21E-04	3.66E-4	439.1
	0.3	1313	1.67	140.5	6.04E-04	7.73E-4	306.9
28	0	1142	7.895E-04	421.7	1.148E-04	7.512	337.3
	0.1	1222	1.40E-03	320.2	2.800E-04	2.30	353.7
	0.2	1335	1.53E-03	279	3.320E-04	5.04	367.8
	0.3	1348	6.68E-01	166.9	3.920E-04	5.58E-4	421.6

## **Influence of sugar beetroot microsheets on the hydration kinetics of cementitious composites: Electrochemical characterization**

Bo Huang<sup>a,c</sup>, Yin Chi<sup>b\*</sup>, Thamer Almotlaq<sup>c,d</sup>, Jianqun Wang<sup>a</sup>, Mohamed Saafi<sup>c\*</sup>, Junjie Ye<sup>e</sup>, Junbo Sun<sup>f</sup>, Yufei Wang<sup>g</sup>, Jianqiao Ye<sup>c</sup>

<sup>a</sup>School of Civil Engineering, Hunan University of Science and Technology, Xiangtan, 411201, China

<sup>b</sup>School of Civil Engineering, Wuhan University, 430072, China

<sup>c</sup>School of Engineering, Lancaster University, Lancaster, LA1 4YR, UK

<sup>d</sup>Civil Engineering department, College of Engineering, Jouf University, Sakaka 72388, Saudi Arabia.

<sup>e</sup>Research Center for Applied Mechanics, Key Laboratory of Ministry of Education for Electronic Equipment Structure Design, Xidian University, Xi'an 710071, China

<sup>f</sup>Institute for Smart City of Chongqing University In Liyang, Chongqing University, Jiangsu, 213300, China

<sup>g</sup>School of Design and the Built Environment, Curtin University, Perth, WA, 6102, Australia

### **Abstract**

This paper examines the influence of novel sugar beetroot-based micro sheets (SMSs) on the hydration of cement. The SMS material was added to cement pastes in different concentrations and the hydration kinetics of the cementitious composites were studied via cyclic voltammetry (CV) and electrochemical impedance spectroscopy (EIS). The effect of SMS on the hydration development of cement, change in the pore size distribution and microstructural evolution were also quantified. The CV and EIS results revealed that the synergetic effect of the reactive SMS surface functional groups and tricalcium silicate (C<sub>3</sub>S) increased the ionic strength of the pore solution, ion diffusion rate and charge transport properties within the cementitious pastes. The CV and EIS measurements correlated well with the two main indicators of the cement hydration rate: the degree of hydration (DOH) and the calcium hydroxide (Ca(OH)<sub>2</sub>) content. The delineated hydration kinetics suggested that the SMS sheets accelerate the dissolution of C<sub>3</sub>S and increase the

---

\* Corresponding author. E-mail address. [m.saafi@lancaster.ac.uk](mailto:m.saafi@lancaster.ac.uk) (Mohamed Saafi)

[yin.chi@whu.edu.cn](mailto:yin.chi@whu.edu.cn) (Yin Chi)

hydration depth by channelling water from the pore solution to the unhydrated cement core thereby amplifying the growth of the hydration phases. As a result, the mechanical properties of the SMS doped cementitious composites were improved. The proposed SMS sheets are a potential sustainable and renewable biomaterial for improving the performance and reducing the carbon footprint of cementitious materials.

**Keywords:** Cementitious composites, sugar beetroot, microsheets, degree of hydration, cyclic voltammetry, electrochemical impedance spectroscopy.

## 1. Introduction

The consumption of ordinary Portland cement (OPC)-based materials is increasing at a rapid pace to meet an ever-grown demand for concrete infrastructure systems. This is of great concern as the production OPC leads to CO<sub>2</sub> emissions which is about 8% of the global CO<sub>2</sub> emissions. One potential way to lower the environmental impacts of cement is to improve the performance and the longevity of cement-based materials [1–6], as early removal and replacement of concrete infrastructure systems from service with new concrete infrastructure systems increases CO<sub>2</sub> emissions and demand for raw materials [7]. It has been shown that if the performance and longevity of cement-based materials is increased by 50%, the demand for cement, aggregates and water will be reduced by 15%, 2.9 to 7.6 Gt and 0.28 to 0.83 Gt, respectively [8]. And it will also reduce energy consumption by 10<sup>6</sup> to 2.3 x 10<sup>6</sup> TJ and CO<sub>2</sub> emissions by 0.4 to 0.7 Gt of CO<sub>2</sub>-eq [8]. This suggests that increasing the longevity of in-use of concrete infrastructure systems by enhancing the performance of OPC-based materials could be a critical means to reducing their environmental impacts.

The strength performance of OPC-based materials depends on the amount of their hydration products, especially the calcium-silicate-hydrate (C-S-H) phases, the principal binding agents in concretes [9]. Higher content of C-S-H phases increases the

engineering properties and improves the durability of OPC-based materials. This allows concrete infrastructure systems to have much longer service life with limited maintenance, thus lower carbon footprint.

Several approaches have been examined with the objective of increasing the hydration phases of cementitious composites. For example, the use of one-dimensional (1D) nanomaterials in cementitious composites have been shown to enhance the engineering properties of the cementitious nanocomposites and ultimately their longevity and sustainability. It was found that the addition of carbon nanotubes (CNTs) and carbon nanofibers (CNFs) to cementitious materials increases the strength and stiffness of the cementitious nanocomposites [10–12]. CNTs and CNFs can control the nanoscale properties of cementitious nanocomposites such as hydration, matrix cracks from shrinkage and mechanical stresses. Previous studies demonstrated that CNTs and CNFs can improve the hydration kinetics of cement pastes, leading to improved growth of the hydration products [11,13–16]. Because of their large specific surface area, 2D nanomaterials such as graphene (G), graphene oxide (GO) and boron nitride (BN) outperform CNTs and CNFs in improving the hydration kinetics of cementitious composites and creating stronger and crack resistant cementitious composites [17–19].

However, due to high costs and energy consumption, and process-derived CO<sub>2</sub> emissions from their production, G, GO, BN, CNTs and CNFs have not been used on an industrial-scale manufacturing of cement-based products.

Cellulosic nanomaterials have emerged as promising low-cost and abundant bio-derived materials that can improve the performance of cement-based materials. One-dimensional (1D) cellulose nanocrystals (CNCs) were used to fuse cementitious composites with the objective of improving the engineering properties of cementitious composites by increasing their hydration products [20–23]. However, due do their small

size and low-specific area, CNCs slightly improved the hydration kinetics of cement, resulting in a moderate enhancement of mechanical properties [24].

Electrochemical techniques such as polarization methods, cyclic voltammetry, AC impedance spectroscopy, and the new time-resolved methods are increasingly being used to characterize materials [25–29]. Recently, electrochemical impedance spectroscopy (EIS) has emerged as a powerful method for characterizing the hydration behaviour of cementitious composites, enabling a comprehensive understanding of the hydration kinetics [30]. In this method, a cementitious composite is treated as an electrochemical cell and its electrochemical impedance  $Z$  is measured by applying an AC voltage  $V$  over a wide range of frequencies, then measuring the current  $I$  across the cell. The electrochemical impedance  $Z$  is calculated as  $Z = V/I$  [31]. The impedance measurements are typically plotted in the form of Nyquist plots where their shape is used to extract crucial information about the cementitious composite characteristics during hydration such as changes in the chemical, electrical and microstructure features [32]. The impedance measurements are also used to model the cement composite using equivalent circuit (EC) elements to uncover the effect of the cement paste ingredients on the hydration kinetics [32]. The impedance measurements are often complemented by the cyclic voltammetry (CV) measurements. CV measurements are commonly used to analyze chemical reactions and ion diffusion in cells such as energy systems [33]. CV involves measuring the current while sweeping a voltage across the cell. The measured current is affected by the electron transfer between the chemical species within the cell and the electrodes, and ion diffusion and migration within the cell solution [33]. Even though, it has not yet been used in cementitious materials extensively, CV can shed light on the electrochemical processes in cementitious materials

by quantifying the dissolution of the cement particles and the change in the pore solution, and the subsequent formation of the hydration phases.

Recently, we have successfully synthesized novel microsheets from sugar beet pulp (SMS) recovered from solid waste of the sugar industry for use in cementitious materials [34]. Unlike current 2D nanomaterials, the developed SMS microsheets have larger specific area and contain a larger number of hydroxyl groups on their surfaces, thus more easily dispersed in water. The SMS microsheets are renewable and much cheaper (around \$10/kg) than existing 2D nanomaterials, thus making them suitable for large applications in the construction industry to improve the performance and reduce the carbon footprint of construction materials. Recently, we have demonstrated through computation that SMS significantly increases the engineering properties of cementitious composites. Indeed, our molecular dynamics simulations have shown that this improvement is attributed to the ability of SMS to both strengthen the hydration product particles and improve the hydration kinetics of cement [35–37].

The effect of the newly developed SMS on the hydration kinetics of OPC is quite complex and is not thoroughly understood, and the interaction mechanisms between the SMS and the OPC particles during hydration are still not experimentally established. Therefore, deep understanding of the hydration behaviour of these new SMS-cementitious composites through experimentation is deemed necessary for the design and optimization of their engineering properties. This will accelerate the adoption of these low-carbon materials in the construction industry.

In this paper, for the first time, we combine cyclic volumetric (CV) and the electrical impedance spectroscopy (EIS) techniques to uncover new hydration functions of SMS in cementitious materials and elucidate the main hydration kinetics of the SMS-cementitious composites. The interaction between the SMS sheets and the cement

particles in their fresh state was firstly determined through centrifugation tests. Then, the influence of SMS on the hydration mechanism of the cement pastes was probed using EIS and CV. An equivalent circuit model for the cementitious composites was developed to ascertain the role of the SMS sheets in the cement hydration kinetics. In addition, BET, TGA, DSC, SEM and TEM analytical tools were used to characterize the SMS sheets and quantify their effect on the formation of the hydration products and the evolution of the microstructure of the cementitious composites. And the quantified  $\text{Ca(OH)}_2$  content and DOH were correlated with the two main CV and EIS parameters: capacitance and electrical impedance.

## **2. Experimental program**

### *2.1. Preparation of the SMS material*

The SMS manufacturing process is shown in Fig. 1 and discussed in detail in [34,37]. The first step of the manufacturing process involved diluting sugar beetroot pulp with a solid content of 1.0% by weight. The pH of the mixture was then raised and kept constant at 14 by adding a 0.5M sodium hydroxide (NaOH) solution. Subsequently, the amounts of hemicellulose and pectin were extracted from the mixture. The mixture was then homogenized at a temperature of 90°C for 5 hours using a stirring blade with a rotation speed of 11m/s. The homogenized solution was filtered to remove the dissolved material, resulting in an SMS paste with a solid content of 8% and an average SMS sheet size of 50 $\mu\text{m}$  x 50 $\mu\text{m}$  in lateral size and 0.25 $\mu\text{m}$  thickness. The manufacturing process consumes low power and is interfaceable with renewable electricity, enough to operate all sub-processes in the SMS making.

The environmentally friendly SMS are formed by linked  $\beta$ -1-4 glycosidic (C-O-C) bonds. The chemical functional groups on the SMS backbone tetrahydropyran ring

include hydroxymethyl group (-CH<sub>2</sub>OH), hydroxy group (-OH) and hydrocarbon methine group (-H) (Fig. 1). Compared to GO, the high content of hydroxyl and hydroxymethyl groups makes SMS more efficiently and evenly dispersed in aqueous solutions.

## *2.2. Preparation of the cement pastes*

Ordinary Portland Cement (OPC) type CEM I 52.5 N with a water-cement ratio of 0.35 was used to prepare the cement pastes. A commercially available superplasticizer (Glenium 51) was used at a concentration of 1-wt% to enhance the workability of the cement pastes. Solutions with concentrations of 0, 0.1, 0.2 and 0.3-wt% of SMS were prepared and added to the cement pastes. To keep the water/cement ratio of 0.35 constant throughout the experimental program, the required amount of mixing water was adjusted to take into consideration the water that is already available in the SMS paste. The solutions were prepared by sonicating the required amounts of SMS, water and superplasticizer for a period of 30 minutes using a tip sonicator (S-450A Branson Ultrasonics<sup>TM</sup> Sonifier<sup>TM</sup>) under 50% duty cycles. The SMS suspensions were mixed with cement for 7 minutes and the resulting cement pastes were poured into 50 mm x 50 mm x 50 mm and 40 mm × 40 mm × 160 mm plastic moulds.

The mini-slump test was performed to evaluate the influence of SMS on the workability of cementitious composites. The spread diameters formed by the pastes were measured upon lifting a mini-slump cone with top diameter, bottom diameter and height of 70 mm, 100 mm, and 60 mm, respectively [38]. During the test, the paste was carefully poured into the mould and subsequently vibrated. After removing the excess paste from the top surface, the mould was lifted vertically to allow the cement paste to cure for 24 hours, the slump diameter was then determined as the average of two measurements for each SMS dosage [39].

The cube specimens were used to quantify the compressive strength, hydration and microstructure evolution of the cementitious composites using TGA/DSC, SEM, EDS and BET analytical tools. The prisms were used to investigate the flexural strength and hydration mechanism of the SMS-modified cementitious composites using CV and EIS. Stainless steel electrodes were inserted into the prisms with 120 mm apart to enable CV and EIS measurements. The prisms and the cubes were left to cure for 24 hours at room temperature and then cured in water for 7, 14 and 28 days at a temperature of 22°C.

### *2.3. Centrifugation test of cementitious composites*

We hypothesize that the hydration kinetics of the cementitious composites are controlled by the synergetic interaction between the cement particles and the SMS sheets. And this synergetic interaction is governed by the amount of SMS sheets adsorbed (a-SMS) onto the surface of the cement particles. As such, centrifugation tests were carried out following [40] to determine the concentration of a-SMS using a MSE Mistral 2000 centrifuge. Cement pastes with a mass of 200g containing SMS at concentrations of 0, 0.1, 0.2 and 0.3-wt% were centrifuged after mixing. The pastes were placed in centrifugal bottles and centrifuged at 3000 rpm for 20 minutes. Subsequently, the centrifuged supernatants were collected and filtered through Cole-Parmer Sterile Cell strainers (40 µm) to remove the cement particles. The filtrates were then oven dried at 45°C for 48 hours to evaporate the water. The dried filtrates obtained from the plain cement pastes contained cement supernatant salt and alkali that are available in the pore solution [41]. And the dried filtrates obtained from the SMS infused cement pastes contained free SMS (f-SMS), and cement supernatant salt and alkali that are in the pore solution. The amount of f-SMS was obtained by subtracting the weight of the dried filtrates obtained from the plain paste from the weight of the dried filtrate obtained from the paste infused with SMS.

The amount of a-SMS was obtained by subtracting the weight of f-SMS from the weight of SMS added to the paste as outlined in [40].

#### *2.4. Electrochemical characterization of the cementitious composites*

The electrochemical behaviour of the cement pastes was investigated with cyclic voltammetry (CV) and electrochemical impedance spectroscopy (EIS) to elucidate the influence of SMS on the evolution of the hydration kinetics of the cementitious composites at 7, 14 and 28 days, using the cement pastes as electrochemical cells. Potentiostat (Gamry Interface 1000) was employed to obtain the CV characteristics of the cementitious composites using the two-probe method as shown in Fig. 2. During this test, an electrical current was passed through the cementitious composite as the voltage is swept between -0.5 V and 0.5 V using a scan rate of 0.2V/s for 10 cycles. Gamry software<sup>TM</sup> was used to produce current vs voltage spectra to extract qualitative hydration kinetics of the cementitious composites.

The EIS measurements were carried out using frequencies between 0.1 Hz and 1 MHz and a sinusoidal voltage of 10 mV. Gamry software<sup>TM</sup> was employed to analyse the EIS results and obtain the equivalent circuit for the cementitious composites.

#### *2.5. Thermal analysis of cementitious composites*

Thermal analysis of SMS and cement pastes was carried out via the thermogravimetric analysis (TGA) and differential scanning calorimetry (DSC) analysis methods using STA 449 F3 Jupiter instrument. This was done to characterize the thermal behaviour of the SMS sheets and cement pastes, and quantify the degree of hydration (DOH) and the change in the calcium hydroxide ( $\text{Ca}(\text{OH})_2$ ) content in the cementitious composites. Air dried SMS samples were transferred into  $\text{Al}_2\text{O}_3$  crucibles for heating. During heating, the apparatus chamber temperature was gradually increased from 20°C to 1100°C at a rate of 10°C/min. Cementitious samples obtained by crushing cement

cubes were grounded into powder to carry out the thermal analysis of the cementitious composites at 7, 14 and 28 days. The powdered cementitious samples were placed in  $\text{Al}_2\text{O}_3$  crucibles for heating. During heating, the chamber temperature was first raised from 20°C to 140°C at a heating rate of 10°C/ min. Then, the temperature was held at 140°C for 30 minutes to remove evaporable water [42]. Finally, the samples were subjected to heat from 140°C to 1100°C at a heating rate of 10°C/min. The TGA and DSC experiments were conducted under nitrogen with a flow rate of 25.00 ml/min and were repeated three times.

#### *2.6. Microstructure characterization of the cementitious composites*

The morphology of the SMS sheets and SMS-infused cement pastes was examined using scanning electron microscopy (SEM) (JEOL JSM-7800F) fitted with X-Max50 Silicon Drift Detector (SDD) of an area of 50 mm<sup>2</sup>. After coating with gold, SEM micro images of the air-dried SMS sheets and the fractured surface of the cement samples (prepared at 7, 14 and 28 days) were produced at a voltage of 2-15 kV and room temperature. JEM-1010 transmission electron microscope (TEM) was used to determine the morphology of the SMS sheets. A 0.2-wt% SMS suspension was first diluted and ultrasonicated for 30 minutes. The solution was then deposited onto carbon-coated TEM grids. The excess liquid was removed with a filter paper and the samples were air-dried at room temperature. The TEM images were produced at an accelerating voltage of 80 kV voltage.

XRD analysis was performed using an Agilent SuperNova single-crystal X-ray diffractometer. Cementitious composite samples containing SMS were prepared in a powdered form at 7 and 28 days to facilitate the XRD examination. The XRD patterns were obtained by scanning from 5° to 65° (2 $\theta$ ) with Cu K $\alpha$  radiation ( $\lambda = 1.5418\text{\AA}$ ) at a scanning rate of 2°/minute, under ambient conditions. The X-ray diffractometer operated

at a voltage of 40kV using a filament current of 40mA and a step size of 0.02°. The pore size, pore volume and specific surface area of the SMS sheets and cementitious composites were quantified by the Brunauer–Emmet–Teller (BET) method using a nitrogen adsorption instrument (MICROACTIVE 3FLEX 3500, Micromeritics, Germany). Prior to testing, The SMS samples were dehydrated in the vacuum and dried at 40°C for 120 minutes under a pressure  $10^{-6}$  Pa and the cementitious composite powder samples (sieved less than 1 mm) were dehydrated in the vacuum and dried at 100°C for 180 minutes under a pressure of  $10^{-6}$  Pa.

### *2.7. Mechanical characterization of the cementitious composites*

The influence of SMS on the compressive strength of the cementitious composites was evaluated using an universal testing machine (UTM) (Instron 8802J5219, 250KN) according to ASTM C 109 [43], at a loading rate of 0.5 MPa/s. The compressive strength of the cubes (50 mm x 50 mm x 50 mm) were determined at 7, 14 and 28 days. The prisms were tested on an ASTM Zwick Roell Z020 machine (C090204019, 20KN, Germany). The flexural strength of the cementitious composites was evaluated using a four-point bending test at 7, 14, and 28 days in accordance with ASTM C78 [44]. Prisms (40 mm x 40 mm x 160 mm) were tested using a displacement control at a constant loading rate of 0.01 mm/min.

## **3. Results and discussion**

### *3.1. Morphology, thermal behaviour and pore structure of SMS*

Fig. 3a-b shows SEM images of the SMS sheets. As can be seen, the morphology of the SMS sheets consists of rippled and wrinkled surface textures. Fig. 3b shows a typical SEM image of the SMS sample with a total thickness of about 0.25 mm. From this figure, we can see that the sample is composed of stacked and overlapped sheets. The

SMS sheets have a thickness of about 0.25  $\mu\text{m}$  (Fig.3b). The TEM images in Fig. 3c-d indicate that the SMS are consisting of randomly oriented and stacked nanofibers with diameters in the 5-8 nm range. The average lateral size of the SMS sheet is about 50  $\mu\text{m}$ .

The thermal stability of the SMS sheets is an important parameter as it indicates whether the SMS sheets can resist the action of heat generated during cement hydration. The thermal behaviour of the SMS sheets is shown in Fig. 3e. From this figure we can see that the thermal decomposition process of SMS is mainly divided into two stages: slow pyrolysis in the temperature range of 20°C to 200°C and rapid pyrolysis in the temperature range of 200°C to 600°C. The slow pyrolysis is the mass loss of the hydrophilic bound water by evaporation whereas, the rapid pyrolysis is the sharp mass loss of the functional groups after SMS dehydration. This is due to the thermal degradation of both the functional group of SMS in the temperature range of 200°C to 380°C and the tetrahydropyran ring backbone structure of SMS in the temperature range of 440°C to 580°C. The DTG peaks indicate that the maximum temperature depolymerization of the SMS functional groups is 329°C and the depolymerization temperature of the tetrahydropyran ring of SMS is around 518°C. The mass loss of SMS remains unchanged between 580°C and 1100°C with a residual mass weight of 20%.

Fig. 3f shows the DSC thermogram and its derivative for the SMS sheets in the temperature range of 20°C to 1000°C. From the derivative of the DSC curve, we can see that the first endothermic broad peak between 20°C and 200°C corresponds to the rearrangement of the molecular chains of SMS caused by the evaporation of bound water. The second endothermic peak between 200°C and 380°C is attributed to the colloidal bond cleavage. The third endothermic transition between 440°C and 580°C corresponds to the depolymerization of cellulose based SMS. The occurrence of the endothermic hump and the first peak phenomena are similar to amorphous cellulose [45]. It is worth noting

that conventional cellulose typically completes its depolymerization over a temperature range of 200°C to 400°C [46,47], whereas the depolymerization of the tetrahydropyran ring backbone of the SMS material is completed over a temperature range of 200-580°C. This indicates, the SMS material has higher thermal resistance than conventional cellulose [46] and can resist the cement hydration temperature which is about 70°C.

The N<sub>2</sub> adsorption-desorption isotherms of the SMS sheets are shown in Fig. 4a. This figure shows that the SMS sheets have a BET specific surface area of 68.35 m<sup>2</sup>/g. The pore size distribution and total pore volume of SMS calculated according to BJH theory are shown in Fig. 4b. As can be seen, the average pore diameter and the pore volume of SMS are 8.19 nm and 0.14 cm<sup>3</sup>/g, respectively. Fig. 4b indicates that the pore size distribution of SMS is a bimodal pore size distribution in the 0-10 nm range with a small number of pores in the 40-80nm range. It is worth mentioning that in comparison to SMS, GO exhibits lower specific surface area [48]. This means SMS outperforms GO for boosting the hydration of cement particles due their higher reactive surface area.

### *3.2. Interaction of SMS sheets with cement particles*

Fig. 5a illustrates the change in the workability as a function of SMS dosage. As shown, the addition of 0.1, 0.2 and 0.3-wt% SMS did not affect the workability of the cement pastes. However, the workability decreased significantly at SMS dosages higher than 0.3-wt%. The addition of 0.40-wt%, 0.50-wt%, and 0.60-wt% SMS decreased the diameter of the pastes by 86.59%, 90.75%, and 96.05%, respectively. This can be attributed to the high specific surface area of SMS and its dominant hydrophilic functional groups which tend to absorb and consume most of the free water in the cement pastes. This results in increased friction between the cement particles which in return decreases the workability of the cement pastes [49].

The effectiveness of the SMS sheets in promoting the dissolution of  $C_3S$  compound during hydration is governed by the direct chemical interaction of  $C_3S$  with the SMS sheets adhered to the surface of the cement particles. The higher the amount of the adhered SMS sheets, the higher the surface hydroxylation rate of  $C_3S$ . As such, the experimental results obtained from the centrifugation experiments were used to determine the amount of a-SMS adhered to the surface of the cement particles. Fig. 5b shows the change in the mass of a-SMS per gram of cement as a function of SMS concentration, whereas Fig. 5c shows the change in the percentage of a-SMS (i.e.,  $a\text{-SMS}/(a\text{-SMS}+f\text{-SMS})$ ) as a function of SMS concentration. As shown in Fig. 5c, the mass of a-SMS is directly proportional to the SMS concentration, where about 92% of SMS are adhered to the surface of the cement particles. The interaction mechanism of SMS with a cement particle is illustrated in Fig. 5d. As depicted, the large surface area and the chemical functional groups enable the SMS sheets to cling to the surface of the cement particle. The large negatively hydroxymethyl ( $-\text{CH}_2\text{OH}$ ) hydroxyl ( $-\text{OH}$ ) groups on the surface of SMS are attracted to the main positively charged  $\text{Ca}^{2+}$ , leading to an electrostatic self-assembly mechanism and the cement particles become wrapped around by the SMS sheets. Here, we believe that the f-SMS sheets (8% of total SMS) remain in the pore solution. The following sections elucidate the effect of the SMS sheets on the hydration kinetics of the cementitious composites.

### *3.3. Thermal analysis of the cementitious composites*

The influence of SMS on the hydration of the cement pastes can be quantified by simply analysing the heat flow and heat of fusion obtained from the DSC measurements. Fig. 6a depicts the effect of SMS on the heat flow first peak at 7 days. The first peak which is known as the dissolution peak is associated with the dissolution of calcium silicate phases and the initial precipitation of ettringite [50]. As shown, the intensity of

the dissolution peak increases as the SMS concentration increases. This can be attributed to the fact that the SMS sheets with high specific area accelerate the hydration of cement and provide additional surface for nucleation and growth of the hydration phases [51]. As such, the more SMS is used, the more heat is generated. Fig. 6a also shows that the dissolution peak shifts to the left due to the addition of SMS. This means that SMS increases the dissolution rate of the cement phases. This can be confirmed by the change in the latent heat of fusion of the cementitious composites as shown in Fig. 6b. As can be seen, the latent heat fusion of the cementitious composites increases with both curing age and SMS concentration due to the increase of the hydration products.

The influence of SMS on the formation of the hydration phases can also be quantified from the thermal degradation of the hydrated cement pastes. Fig. 7a-c displays the effect of SMS on the thermal decomposition of the cementitious composites at 7, 14 and 28 days where amount of the mass loss gradually increases with SMS concentration. Fig. 7a-c show that the thermal decomposition of the cement pastes goes through three main weight loss stages. The weight loss of the cement pastes due to the gradual loss of the bound water takes place in the first stage, between 140 and 300°C. In the second stage, the thermal dehydration of  $\text{Ca(OH)}_2$  occurs in the temperature range 420 to 480°C. Finally, in the third stage, the decomposition of calcium carbonate ( $\text{CaCO}_3$ ) takes place between 600 and 780 °C [40,52]. As can be seen in Fig. 7c, the final weight loss of the cement pastes at 28 days increases with SMS concentration due to more evaporation of the chemically bound water (CBW) from the thermally decomposed hydration products.

Fig. 7d-f show the derivative thermogravimetry (DTG) curves of the cement pastes at 7, 14 and 28 days. The DTG peaks in this figure indicate that the cementitious composites lost their CBW or decomposed at a specific temperature range, regardless the SMS content. The range of pyrolysis peaks shown in Fig. 7d-f confirm that the weight

loss of C-S-H (140-300°C), Ca(OH)<sub>2</sub> (420-480°C) and Ca(CO<sub>3</sub>) (600-780°C) phases occurs in different temperature ranges. The increase in the intensity of the DTG peaks due to the addition of SMS is an indicative of more hydration products being decomposed. Furthermore, the decomposition peak of Ca(CO<sub>3</sub>) phase gradually shifts towards the left (decomposition temperature decreased around 10°C) when the SMS content increases. This is due to the decomposition of SMS/Ca(CO<sub>3</sub>) composites which takes place slightly prior to the plain Ca(CO<sub>3</sub>) phase. The DTG results further demonstrate that the addition of SMS amplifies the formation of the hydration phases.

The thermal mass loss of the cementitious composites is related to DOH. Hence, the DOH was calculated according to the method described in [42].

$$DOH(TGA) = \frac{\frac{m(cbw)}{m(remain)}}{0.23} \quad (1)$$

Where  $m(cbw)$  is the mass of chemically bound water and  $m(remain)$  is the mass of samples remaining in the crucible.

Fig. 7g shows the calculated DOH at 7, 14 and 28 days. As shown, the DOH increases with SMS content. At a SMS content of 0.3-wt%, the DOH increased by 3.5%, 6.1% and 5.6% at 7, 14 and 28 days, respectively. Fig. 7h shows the effect of SMS on the amount of Ca(OH)<sub>2</sub>. The amount of Ca(OH)<sub>2</sub> in the cementitious composites was calculated according to [34]. As can be seen, the trend of Ca(OH)<sub>2</sub> increasing with SMS concentration is similar to that of DOH. At a SMS content of 0.3 wt% increased the amount of Ca(OH)<sub>2</sub> by 5.04%, 10.29% and 13.45% at 7, 14 and 28 days, respectively. The increase of Ca(OH)<sub>2</sub> is indicative of the increase of the other hydration products such as C-S-H as a result of the addition of SMS.

### 3.4. Electrochemical response of SMS cementitious composites using voltammetry

The hydration kinetics behind the observed increase in DOH and  $\text{Ca(OH)}_2$  are uncovered by examining the electrochemical response of the cementitious composites. As such, the influence of the SMS sheets on the electrochemical behaviour of the cement pastes during hydration was investigated using CV where the electrochemical cement paste cells were charged and discharged between -0.5 V and 0.5 V. Fig. 8a-c show the CV curves at different SMS concentrations and curing ages. CV plots the amount of the electrical current flowing through the electrochemical cement cell when the voltage is varied between -0.5 V to 0.5 V. As shown, the CV curves exhibit elliptical and symmetrical shapes, indicating that the cementitious composites are behaving like electric capacitors [53]. From the CV curves, the peak current is estimated at a potential of 0.5 V and plotted against SMS concentration at different curing ages as shown in Fig. 8d. As it can be observed, the intensity of the current flowing through the cement pastes during hydration increases with SMS concentration and decreases with increasing curing age. This means the SMS sheets facilitate the movement of electrons towards the electrodes while the curing age diminishes the movement of electrons towards the electrodes. This electrochemical reaction mechanism can be ascertained by examining the influence of the SMS sheets on the capacitance of the electrochemical cement pastes.

The capacitance  $C$  of the electrochemical cement paste cells was calculated using the following equation [54]:

$$C = \frac{\int IdV}{2\nu\Delta V} \quad (2)$$

Where  $\int IdV$  is the integrated area of the CV curve,  $\Delta V$  is the potential voltage window and  $\nu$  is the scan rate (V/s). The influence of SMS on the capacitance of the cement pastes at 7, 14 and 28 days is shown in Fig. 9a. As illustrated, at a specific curing age, the

capacitance of the cementitious composites increases with increasing SMS concentration. This increase however is predominant in the first 7 days of hydration. The a-SMS sheets increases the ionic strength (i.e., increased ion concentration) of the pore solution, as a consequence of their direct interaction with  $C_3S$ . The chemical functional groups such as hydroxymethyl ( $-CH_2OH$ ), hydroxy ( $-OH$ ) and hydrocarbon methine group ( $-H$ ) allow for dissolution catalysis to occur due to the interaction of the a-SMS sheets with the highly reactive  $C_3S$ . This increases the density of ions, mainly  $Ca^{2+}$  and  $OH^-$ , which in return increases the ionic strength of the pore solution. This increase could also be attributed in part to the accumulation of the released ions (i.e.,  $Ca^{2+}$ ,  $OH^-$ ) into the porous a-SMS sheets. As the hydration progresses the ions in the pore solution are consumed and amount of the hydration phases are increased. This dampens the diffusion and electric mobility of ions which results in reduction of the capacitance of the cement pastes when the curing age increases.

The influence of DOH and  $Ca(OH)_2$  on the capacitance of the cementitious composites is shown in Fig. 9b-c at the three SMS concentrations. The increase in DOH and  $Ca(OH)_2$  is a good indicator of the evolution of the other hydration phases such as C-S-H products. As shown, the capacitance is proportional to both DOH and  $Ca(OH)_2$ . The rate of change of the capacitance with respect to DOH and  $Ca(OH)_2$  is more predominant at 7 days due to higher ionic strength of the cementitious composites. The lower rate of change of the capacitance at 14 and 28 days of curing is due to lower ionic conductivity of the cementitious composites due to the consumption of ions in the pore solution. The positive change in the capacitance of the cement pastes reflects the increase in the hydration phases resulting from the inclusion of SMS. As such, the cyclic voltammetry method presents a good tool to understand and monitor the hydration of cementitious composites containing reactive additives.

### 3.5. Electrochemical response of SMS cementitious composites using EIS

EIS characterization was used to complement the CV analysis of the hydration kinetics of the cementitious composites. Fig. 10 shows the Nyquist plots for the cementitious composites at 7, 14 and 28 days. As illustrated, each Nyquist plot is composed of a depressed capacitive arc in the high frequency region and somewhat a straight line representing the Warburg impedance in the low frequency region. The depressed capacitive arc represents the charge transfer at the electrode-ionic solution interface and the straight line represents the diffusion of ions into the electrodes. It is worth noting that in the middle-frequency range, the impedance of the cementitious composites somewhat decreases with the curing age. This is probably due to the effect of the porosity of the hydration phases. Previous studies have shown that Nyquist plots in the medium-frequency region describe the effect of porosity of materials on the ionic conductivity [55]. C-S-H phases are porous and considered as ionic materials due to their good ionic conductivity [56]. Hence, we hypothesize that the observed change in the impedance in the medium-frequency range is due to the fact that as the hydration continues, more C-S-H phases are produced thereby facilitating ion diffusion through their pores which in return decreases the electrical resistance of the matrix.

The EIS data was further analysed to delineate effect of SMS on the change in the hydration products of the cementitious composites. This was done by examining the change in the bulk resistance and dielectric constant of the cementitious composites. The bulk electrical resistance was calculated from the bode plot of the impedance modulus  $\log|Z|$  and phase as depicted in Fig. 11a. In this figure, a cementitious composite with 0.1wt% SMS is used as an example to show how the bulk electrical resistance was calculated. As shown in Fig. 11a, the blue dashed rectangles show the phase plateauing near zero in the high frequency range of  $5 \times 10^3$  to  $5 \times 10^4$  Hz and the  $\log|Z|$  values in this

frequency range where the phase is plateauing near zero. In this frequency range, the cementitious composite exhibits a resistive behaviour, and its bulk electrical resistance can be calculated from the average  $\log|Z|$  values as  $R (\Omega) = 10^{\log|Z|}$ .

The bulk resistance values are given in Fig. 11b at 7, 14 and 28 days for different SMS concentrations. This figure indicates that there is a trend of increasing bulk resistance with increasing SMS concentration due to enhanced growth of the hydration products. This can be demonstrated in the plot of the bulk electrical resistance versus the degree of hydration (Fig. 11c), obtained from the thermal analysis of the cementitious composites. Fig. 11c shows that the bulk electrical resistance increases with increasing DOH. This is because the formation of the hydration phases consumes the highly conductive ions in the pore solution thereby increasing the bulk electrical resistance of the cementitious composites [57]. This implies that EIS is a useful tool for both interpreting the hydration processes of cement and real time monitoring of DOH.

The change in the dielectric constant ( $\epsilon'$ ) of the cementitious composites at 28 days is shown in Fig. 11d. The dielectric constant ( $\epsilon'$ ) was calculated using the following equation:

$$\epsilon' = \frac{dZ''}{2\pi Z^2 \epsilon_0 A} \quad (3)$$

where  $d$  is the distance between the electrodes,  $Z''$  is the imaginary impedance,  $Z$  is the total impedance,  $\epsilon_0$  is the vacuum dielectric constant and  $A$  is the contact area of the electrodes. Fig. 11d shows that the dielectric constant of cementitious composites decreases with frequency. This is due to the reduction of space charge polarization effect. During the hydration of the plain cement paste, the primary  $\text{Ca}^{2+}$  and  $\text{OH}^-$  ions are leached from  $\text{C}_3\text{S}$ . These unbound charged ions polarize in response to the applied electric field

which is responsible for the measured dielectric constant of the cement paste. As the hydration kinetics progress,  $\text{Ca}(\text{OH})_2$ , C-S-H and ettringite hydration phases begin to form which in return hinders the polarization of the charged ions thereby reducing the initial dielectric constant [58,59]. Fig. 11d also shows that at a fixed frequency, the dielectric constant of the cementitious composites decreases with increasing SMS concentration. This decrease is attributed to the effect of SMS on the hydration kinetics of cement. The addition of SMS increases the release of the primary  $\text{Ca}^{2+}$  and  $\text{OH}^-$  ions into the pore solution, resulting in higher ionic conductivity (i.e., higher ionic strength of the pore solution). This amplifies the growth of the hydration phases. These hydration phases along with the porous SMS sheets hamper the polarization of the charged ions, resulting in a further decrease in the dielectric constant. This means, the more SMS sheets in the cement paste, the lower the dielectric constant, as shown in Fig. 11d.

### *3.6. Equivalent circuit model for the SMS cementitious composites*

To further understand the hydration process of the cementitious composites and delineate the main mechanisms by which the SMS sheets accelerate the hydration rate of cement, an equivalent circuit (EC) model was developed and the effect of the addition of SMS on its electrical components was characterized. The two in-series-components of the EC model for the cementitious composites are shown in Fig. 12a. Bode plots showing the fit of the EC model to the measured impedances at 28 days are given in Fig. 12b-e. This figure indicates that the EC model fits adequately the measured impedances.

In the EC model, the cement paste is represented by its pore solution resistance ( $R_s$ ), double layer capacitance ( $C_{dl}$ ), charge transfer resistance ( $R_{ct}$ ) and Warburg impedance ( $Z_w$ ) and the electrodes are represented by their capacitance ( $C_e$ ) and resistance ( $R_e$ ).

The Warburg element ( $Z_W$ ), represents the ion diffusion in the cement paste. The Warburg element is generally described by its parameters in the following equivalent impedance equation.

$$Z_W = \sigma \omega^{-\frac{1}{2}}(1 - j) \quad (4)$$

$$\omega = 2\pi f \quad (5)$$

where  $\sigma$  is a Warburg diffusion coefficient and  $f$  is the operating frequency.

The values of the EC components were determined for each SMS concentration and curing age by fitting the experimental impedances using Gamry Echem Analyst program version 6.25. The fitted values of the EC model components and their errors are given in Table 1.

The total impedance  $Z$  of the equivalent circuit model shown in Fig. 12a can be expressed as:

$$Z = R_s + \frac{R_{ct} + \sigma \omega^{-\frac{1}{2}}(1 - j)}{1 + j\omega R_{ct} C_{dl} + j\omega Z_W C_{dl}} + \frac{R_e}{1 + j\omega R_e C_e} \quad (6)$$

The real part  $Z'$  is given by:

$$Z' = R_s + \frac{R_{ct} + \sigma \omega^{-\frac{1}{2}}}{\left(1 + \omega^{\frac{1}{2}} \sigma C_{dl}\right)^2 + \omega^2 C_{dl}^2 \left(R_{ct} + \sigma \omega^{-\frac{1}{2}}\right)^2} + \frac{R_e}{1 + (\omega R_e C_e)^2} \quad (7)$$

The influence of SMS on the hydration of the cement pastes can be elucidated by examining the change in the main cement paste parameters  $R_s$ ,  $R_{ct}$ ,  $C_{dl}$  and  $Z_W$  of the real parts of the impedance (Eqs. 7). Fig. 13a shows the effect of SMS on the resistance of the pore solution ( $R_s$ ) at different curing ages. As shown, the resistance of the pore solution increases with increasing SMS concentration. This can be attributed to the fact that the

ions and the free water are consumed immediately after the dissolution of the cement particles to produce hydration products which in return increases the resistance of the pore solution. Due to their high electrical resistance and surface area, the SMS sheets fill the capillary pores in the cement pastes thereby increasing their overall electrical resistance. Fig. 13a also shows that the electrical resistance of the pore solution increases with curing age due to the formation of the hydration gels in the capillary pores.

The influence of SMS on the charge transfer resistance ( $R_{ct}$ ) of the cement pastes at the at 7, 14 and 28 days is depicted in Fig. 13b. The charge transfer resistance represents the resistance against the process of electron movement between the cement paste and the electrodes resulting from the electrochemical reaction during hydration. The charge transfer in materials can be described by the following equation [60]:

$$R_{ct} = \frac{RT}{n^2 F^2 A C_0 K_{et}} \quad (8)$$

where  $R$  is gas constant,  $T$  is temperature,  $n$  is the number of electrons involved in the charge transfer process,  $F$  is Faraday's constant,  $A$  is the electrode surface area,  $C_0$  is the concentration of ions at the electrode surface and  $K_{et}$  is the electron transfer rate.

As shown in Fig. 13b, the overall trend of the charge transfer resistance decreasing with increasing SMS concentration and increasing with curing age supports the cyclic CV results. As previously highlighted, the interaction of the a-SMS sheets with  $C_3S$  increases the concentration of ions which results in higher number of electrons moving between the cement paste and the electrodes with a higher electron transfer rate. This reduces the charge transfer resistance. However, the charge transfer resistance somewhat increases with increasing curing age due to the formation of the hydration phases which reduces the diffusion of ions in the cement paste as shown in Fig. 13c.

Fig. 13c depicts the change in the Warburg impedance ( $Z_w$ ) as a function of SMS concentration. The Warburg impedance represents the bulk resistance to the ionic mass

transfer (i.e., diffusion mechanism of ions) in the cement paste. The Warburg impedance is associated with the Warburg coefficient  $\sigma$  (see Eq. 4), which represents the diffusion of ions in the cement paste. The higher the value of  $\sigma$ , the less the diffusion of ions in the cement paste. The Warburg coefficient  $\sigma$  is given by the following equation [61]:

$$\sigma = \frac{RT}{\sqrt{2}n^2F^2AC_0D^{1/2}} \quad (9)$$

Where  $D$  is the diffusion coefficient of ions in the cement paste.

The Warburg coefficient  $\sigma$  can be determined from the experimental real impedance data. Fig. 13d plots the experimental real impedance against the angular frequency ( $\omega^{1/2}$ ) (known as Warburg plot) for different SMS concentrations. The slope of the Warburg plot presents the Warburg coefficient  $\sigma$ . The effect of SMS concentration on the Warburg coefficient  $\sigma$  is shown in Fig. 13e. As can be seen from this figure, the Warburg coefficient  $\sigma$  decreases with increasing SMS concentration. This implies that the inclusion of SMS increases the diffusion coefficient of ions ( $D$  in Eq. (9)) during hydration. The C-S-H nanopores typically form the dominant pathways for ion diffusion and water transport in cementitious materials [62,63]. Higher ionic diffusion coefficients are typically associated with higher growth of C-S-H phases. Diffusion coefficient  $D$  of ions is typically larger in cement pastes with higher of C-S-H products than that in cement pastes with lower of C-S-H products [64]. Fig. 13e also shows that the Warburg coefficient  $\sigma$  increases with increasing curing age. As the hydration of the cement pastes progresses, water and ions in the pore solution are depleted and the amount of hydration phases is increased, resulting in less diffusion of ions.

Fig. 13f shows the effect of SMS concentration on the double-layer capacitance ( $C_{dl}$ ) of the electrode/cement paste interface at different curing ages. As depicted in Fig.

13f, at 7 days of curing, the double-layer capacitance increases with SMS concentration. The addition of SMS increases the accumulation of ions at the electrode-cement interface due to rapid dissolution of  $C_3S$ . This increases the double-layer capacitance of the cementitious composites.

The CV and EIS results support the notion that the hydration of cement is controlled by the kinetics of a-SMS/ $C_3S$  interfacial chemical interactions. The f-SMS sheets in the pore solution also contribute to the rapid dissolution of  $C_3S$ . The findings of the CV and EIS tests were leveraged to uncover the main hydration kinetics of the cementitious composites, taking into consideration the SMS surface functional groups that are the driving forces for the dissolution of  $C_3S$  and the growth of the hydration phases.

### *3.7. Elucidation of the hydration kinetics of cementitious composites*

The centrifugation, EIS and CV results were used to identify the main chemical processes involved in the hydration of the cementitious composites and delineate the role of the SMS surface functional groups in the dissolution of  $C_3S$ . The EIS and CV results revealed that the change in the electrochemical properties of the cementitious composites during hydration is governed by the ionic strength of the pore solution. This ionic strength is highly dependent on the concentration and the electric mobility (i.e., diffusion) of ions produced during the dissolution of  $C_3S$  and increases with SMS content.

The centrifugation test results revealed that most of SMS sheets tend to deposit on the surface of the cement particles (i.e., a-SMS sheets) (Fig. 14a) and a small amount of SMS sheets remain in the pore solution (i.e., f-SMS sheets). As such, we hypothesize that the dissolution kinetics of the cement particles are driven by both the a-SMS and f-SMS sheets. Based on this, we believe that the SMS material has unique two hydration functions in cementitious materials that had not been seen with other nanomaterials.

Fig. 14 describes these two hydration functions. The first function is the rapid hydroxylation of  $C_3S$  and the subsequent formation of the hydration phases as shown in Fig. 14b. In this case, the inner a-SMS layers directly in contact with the cement particle (Fig. 14b) undergo interfacial chemical reactions with  $C_3S$  in the presence of water. During this chemical process, the highly reactive  $C_3S$  breaks the inter- and intramolecular H-bonds between the hydroxyl/hydroxymethyl ( $-OH/-CH_2-OH$ ) functional groups of SMS which leads to deprotonation and the subsequent dissolution of the inner a-SMS layers (Fig. 14b). Consequently, a proton-rich environment is produced, and a fast proton exchange rate is enabled which results in a fast dissolution rate of  $C_3S$  (Fig. 14b). This process increases the ionic strength of the pore solution due to increased concentration of  $Ca^{2+}$  and  $OH^-$  ions which in return amplifies the formation of the hydration phases. The disruption of the inter- and intramolecular H-bonds between the hydroxyl/hydroxymethyl functional groups of the SMS layers also produces methanol ( $CH_3OH$ ) and ethanol ( $CH_2H_5OH$ ) organic chemical compounds (Fig. 14c) in the pore solution which boosts the mobility of protons. This further accelerates the hydroxylation of  $C_3S$  and increases the ionic strength of the pore solution, thereby intensifying the formation of the hydration phases.

The second function is channeling water molecules from the pore solution to the unhydrated cement core. The outer undissolved a-SMS layers (Fig. 14c-d) remain embedded in the hydration phases and facilitate the transport of water from the pore solution to the unhydrated  $C_3S$ . Unlike existing nanomaterials, the large specific surface area the number of functional groups allow SMS to diffuse water deep into the unhydrated  $C_3S$  core thereby increasing the hydration depth of the cement particle (Fig. 14d). Similar to the inner a-SMS layers, the f-SMS sheets in the pore solution chemically interact with  $Ca^{2+}$  and  $OH^-$  ions and undergo deprotonation due to the breakage of H-bonds between

their functional groups (Fig. 14b). This increases the density of protons involved in the ion exchange mechanism which accelerates the dissolution of  $C_3S$  and the subsequent release of  $Ca^{2+}$  and  $OH^-$  ions into the pore solution. This further amplifies the formation of the hydration phases.

### *3.8. Effect of SMS on the microstructure of the cementitious composites*

#### *3.8.1. Pore structure of SMS-cementitious composites*

The CV and EIS results elucidated the origin of the chemical reactions responsible for the enhanced hydration of cement when the SMS sheets are present. The effect of SMS on the microstructure of the cementitious composites was examined to confirm the CV and EIS experimental results. Fig. 15a shows the BET adsorption isotherms for the cementitious composites at 28 days. As shown in this figure, the isotherms are IUPAC classification type IV isotherms with H3 hysteresis loop. This indicates that the cementitious composites are marked by a very wide pore size distribution and contain mesopores [65,66]. Fig. 15a also shows that the hysteresis curves are quite narrow, and the adsorption and desorption branches are almost vertical and nearly parallel when the relative pressure is above 0.96, indicating the presence of slit-shaped pores in the cementitious composites [67].

The BET specific surface area (SSA) of the cementitious composites is given in Fig. 15b. As depicted, the SSA of the cementitious composites increases with increasing SMS concentration, and a maximum increase of 56.38% was obtained at a SMS concentration of 0.3 wt%. This demonstrates that the SMS increases the SSA of the hydration phases which is in line with previous studies on cementitious composites containing carbonaceous 2D nanomaterials such as GO and graphene [17,68,69].

The cumulative pore volume and its derivative (i.e., pore size distribution) as a function of the pore size are plotted in Fig. 15c-d. These figures show that the pore volume

increases with increasing SMS concentration. This is attributed to an increased amount of the C-S-H hydration products [70]. Fig. 15d indicates that the bulk of the pores is centred 5-8 nm.

### *3.8.2. Evolution of the microstructure of SMS-cementitious composites*

The XRD patterns of the cementitious composites with SMS at 7 and 28 days are depicted in Fig. 16. As shown, all cementitious composites exhibited the same hydration products. However, the intensity of the crystal diffraction peaks were influenced by SMS. From Fig. 16, we can see that at 7 and 28 days, the intensity of the ettringite, calcium hydroxide, and calcium carbonate peaks increased with increasing SMS concentration. This is more apparent at 28 days. The increase in the peak intensities is an indication of increased amount of the hydration phases resulting from the addition of SMS [71]. This is reflected in the increase of the mechanical properties of the cementitious composites containing SMS.

The evolution of the microstructure of the cementitious composites at 14 days is shown in Fig. 17. The microstructure of the plain cement matrix (Fig. 17a) is of highly heterogenous nature and is marked by a high content of  $\text{Ca(OH)}_2$  particles with different sizes, pores, and unreacted cement particles. The addition of SMS renders the microstructure of the cementitious composites denser and somewhat homogenous. The microstructure of the cement matrix with 0.1-wt% contains stacked  $\text{Ca(OH)}_2$  particles intermixed with C-S-H gel (Fig. 17b). At higher SMS concentrations, the microstructure of the cementitious composites shows a compact microstructure with smaller  $\text{Ca(OH)}_2$  particles embedded in C-S-H gels as shown in Fig. 17c-d.

The effect of SMS on the microstructure of the cementitious composites at 28 days is shown in Fig. 18. As shown, the plain cementitious composite is mainly composed of agglomerated  $\text{Ca(OH)}_2$  particles. The cementitious composites containing SMS show

better packing density due to the increased  $\text{Ca}(\text{OH})_2$  and C-S-H hydration phases. Ettringite needles embedded in C-S-H are observed in the cementitious composite containing 0.30 wt%. The observed changes in the microstructure of the cementitious composites further confirm the results of CV and EIS characterization, that the addition of SMS leads to larger amount of hydration phases and better microstructural packing.

### *3.9. Effect of SMS on the compressive and flexural strength of the cementitious composites*

Fig. 19a depicts the effect of SMS on the compressive strength of the cementitious composites at 7, 14 and 28 days. As shown, the compressive strength of all cementitious composites increases with curing age. It can also be seen that the addition of SMS resulted in a slight increase in the compressive strength. For a given curing age, the compressive strength somewhat plateaued between 0.1 and 0.3-wt% SMS, leading to an increase of 4.89%, 3.93%, and 8.33% at 7, 14 and 28 days, respectively. These low compressive strength gains are in line with other studies that showed GO is more effective in improving the flexural strength of cementitious composites than the compressive strength [72,73]. It was found that the crack-bridging mechanism induced by GO increased the flexural strength more than the compressive strength [74].

Fig. 19b depicts the variation of the flexural strength of the cementitious composites as a function of SMS concentration at 7, 14, and 28 days. As shown, the 0.20-wt% concentration produced the highest flexural strength. At this concentration, the flexural strength is improved by 13.16%, 34.63% and 31.56 at 7, 14 and 28 days, respectively. This enhancement in the flexural strength is attributed to the improved hydration kinetics which resulted in more hydration products. The improvement of the flexural strength of the cementitious composites is attributed to the higher hydration degree and the reinforcing and crack-bridging effect provided by the SMSs. Owing to their hydroxyl groups, the SMSs can easily intercalate into the hydration products thus

linking them together to form a denser and packed microstructure. The enhanced SMS-matrix adhesion/interlocking characteristics resulting from the wrinkled SMS sheets also improve the flexural strength of the cementitious composites.

At 0.3-wt% concentration, the effect of SMS on the flexural strength is diminished. This is probably due to the formation of weak zones in the cement matrix created by the agglomeration of the SMS sheets [34]. In addition, recent studies have shown that when microsheets are used in cementitious materials in high concentrations, their high surface area and hydroxyl groups facilitate the agglomeration of the cement particles and the formation of a flocculation structure within the matrix [35,36]. These effects inhibit the efficiency of microsheets in enhancing the performance of cementitious materials.

#### **4. Conclusion**

This research investigated the influence of new SMS sheets on the hydration kinetics of cement using a combination of CV and EIS coupled with analytical characterization tools. The low cost and environmentally friendly SMS material was derived from beet pulp, a by-product of sugar manufacturing. The results revealed that the large specific area and the number of reactive functional groups enable the SMS sheets to perform two hydration functions in cementitious materials that had not been observed before. The first function is the rapid hydroxylation of  $C_3S$  resulting from the dissolution of the SMS inner layers. The second function is the transport of water molecules from the pore solution to the unhydrated cement cores through the SMS layers that remained embedded in the hydration phases. These two hydration functions amplified the degree of hydration of cement and increased the amount of the hydration phases. Furthermore, The CV capacitance and the EIS electrical resistance of the cementitious composites correlated well with the change in the  $Ca(OH)_2$  content and DOH. As a result, the combined CV and EIS can be used to understand complex hydration kinetics of

cementitious materials infused with nano additives and monitor the evolution of their hydration phases.

The workability of the cement pastes was not affected by the addition of SMS when the dosage is between 0.1 and 0.3-wt%. The workability, however, decreased significantly at higher SMS dosages. The maximum percentage decrease was 96.05% at a SMS dosage of 0.6-wt%. This can be attributed to the hydrophilic functional groups on the surfaces of SMS. This reduces the free water in the cement paste which in return reduces its workability. The more SMS is added, the more the free water is reduced.

The mechanical properties of the cementitious composites were improved by the incorporation of SMS. However, this improvement is more pronounced in the flexural strength, indicating that SMS is more effective in improving the flexural strength than the compressive strength. At 28 days, the three SMS dosages produced somewhat similar compressive strength increases, around 8.33%, whereas 0.2-wt% produced the highest flexural strength increase of 31.56%. This is attributed to the higher degree of hydration and the improved strengthening effect resulting from the good SMS/matrix chemical bonding and mechanical interlocking, and crack-bridging mechanisms. The characteristics of the SMS-cementitious composites presented in this paper will help design concretes with improved engineering properties and lower carbon footprint for sustainable construction of infrastructure.

### **Acknowledgments**

This research work is financially supported by the Scientific Research Found of Hunan Provincial Education Department of China (22B0473), the European Commission Horizon 2020 Marie Skłodowska-Curie Research Grant (B-SMART 799658).

## Reference

- [1] G. Habert, D. Arribe, T. Dehove, L. Espinasse, R. Le Roy, Reducing environmental impact by increasing the strength of concrete: Quantification of the improvement to concrete bridges, *J. Clean. Prod.* 35 (2012) 250–262. <https://doi.org/10.1016/j.jclepro.2012.05.028>.
- [2] X. Wang, M.-Z. Guo, T.-C. Ling, Review on CO<sub>2</sub> curing of non-hydraulic calcium silicates cements: Mechanism, carbonation and performance, *Cem. Concr. Compos.* 133 (2022) 104641. <https://doi.org/10.1016/j.cemconcomp.2022.104641>.
- [3] S. Fang, L. Li, Z. Luo, Z. Fang, D. Huang, F. Liu, H. Wang, Z. Xiong, Novel FRP interlocking multi-spiral reinforced-seawater sea-sand concrete square columns with longitudinal hybrid FRP–steel bars: Monotonic and cyclic axial compressive behaviours, *Compos. Struct.* 305 (2023) 116487.
- [4] C. Zhou, J. Wang, X. Shao, L. Li, J. Sun, X. Wang, The feasibility of using ultra-high performance concrete (UHPC) to strengthen RC beams in torsion, *J. Mater. Res. Technol.* 24 (2023) 9961–9983. <https://doi.org/10.1016/j.jmrt.2023.05.185>.
- [5] Z. Xiong, L. Lin, S. Qiao, L. Li, Y. Li, S. He, Z. Li, F. Liu, Y. Chen, Axial performance of seawater sea-sand concrete columns reinforced with basalt fibre-reinforced polymer bars under concentric compressive load, *J. Build. Eng.* 47 (2022) 103828. <https://doi.org/10.1016/j.jobbe.2021.103828>.
- [6] C. Zhou, J. Wang, W. Jia, Z. Fang, Torsional behavior of ultra-high performance concrete (UHPC) rectangular beams without steel reinforcement: Experimental investigation and theoretical analysis, *Compos. Struct.* 299 (2022) 116022. <https://doi.org/10.1016/j.compstruct.2022.116022>.
- [7] K.A. Ali, M.I. Ahmad, Y. Yusup, Issues, impacts, and mitigations of carbon dioxide emissions in the building sector, *Sustain.* 12 (2020). <https://doi.org/10.3390/SU12187427>.
- [8] S.A. Miller, The role of cement service-life on the efficient use of resources, *Environ. Res. Lett.* 15 (2020). <https://doi.org/10.1088/1748-9326/ab639d>.
- [9] Z. Xiong, W. Wei, S. He, F. Liu, H. Luo, L. Li, Dynamic bond behaviour of fibre-wrapped basalt fibre-reinforced polymer bars embedded in sea sand and recycled aggregate concrete under high-strain rate pull-out tests, *Constr. Build. Mater.* 276 (2021) 122195. <https://doi.org/10.1016/j.conbuildmat.2020.122195>.
- [10] F. Torabian Isfahani, W. Li, E. Redaelli, Dispersion of multi-walled carbon nanotubes and its effects on the properties of cement composites, *Cem. Concr. Compos.* 74 (2016) 154–163. <https://doi.org/10.1016/j.cemconcomp.2016.09.007>.
- [11] W. Meng, K.H. Khayat, Effect of graphite nanoplatelets and carbon nanofibers on rheology, hydration, shrinkage, mechanical properties, and microstructure of UHPC, *Cem. Concr. Res.* 105 (2018) 64–71. <https://doi.org/10.1016/j.cemconres.2018.01.001>.
- [12] Z.S. Metaxa, M.S. Konsta-Gdoutos, S.P. Shah, Carbon nanofiber cementitious composites: Effect of debulking procedure on dispersion and reinforcing

- efficiency, *Cem. Concr. Compos.* 36 (2013) 25–32.  
<https://doi.org/10.1016/j.cemconcomp.2012.10.009>.
- [13] M. Tafesse, H.-K. Kim, The role of carbon nanotube on hydration kinetics and shrinkage of cement composite, *Compos. Part B Eng.* 169 (2019) 55–64.
- [14] Y. Sargam, K. Wang, Hydration kinetics and activation energy of cement pastes containing various nanoparticles, *Compos. Part B Eng.* 216 (2021) 108836.  
<https://doi.org/10.1016/j.compositesb.2021.108836>.
- [15] A.J.N. MacLeod, F.G. Collins, W. Duan, Effects of carbon nanotubes on the early-age hydration kinetics of Portland cement using isothermal calorimetry, *Cem. Concr. Compos.* 119 (2021) 103994.  
<https://doi.org/10.1016/j.cemconcomp.2021.103994>.
- [16] M.I. Haque, W. Ashraf, R.I. Khan, S. Shah, A comparative investigation on the effects of nanocellulose from bacteria and plant-based sources for cementitious composites, *Cem. Concr. Compos.* 125 (2022) 104316.  
<https://doi.org/10.1016/j.cemconcomp.2021.104316>.
- [17] Z. Pan, L. He, L. Qiu, A.H. Korayem, G. Li, J.W. Zhu, F. Collins, D. Li, W.H. Duan, M.C. Wang, Mechanical properties and microstructure of a graphene oxide-cement composite, *Cem. Concr. Compos.* 58 (2015) 140–147.  
<https://doi.org/10.1016/j.cemconcomp.2015.02.001>.
- [18] M. Krystek, D. Pakulski, V. Patroniak, M. Górski, L. Szojda, A. Ciesielski, P. Samorì, High-Performance Graphene-Based Cementitious Composites, *Adv. Sci.* (2019). <https://doi.org/10.1002/advs.201801195>.
- [19] M.A. Rafiee, T.N. Narayanan, D.P. Hashim, N. Sakhavand, R. Shahsavari, R. Vajtai, P.M. Ajayan, Hexagonal boron nitride and graphite oxide reinforced multifunctional porous cement composites, *Adv. Funct. Mater.* 23 (2013) 5624–5630. <https://doi.org/10.1002/adfm.201203866>.
- [20] T. Fu, F. Montes, P. Suraneni, J. Youngblood, J. Weiss, The influence of cellulose nanocrystals on the hydration and flexural strength of Portland cement pastes, *Polymers (Basel)*. 9 (2017). <https://doi.org/10.3390/polym9090424>.
- [21] S.A. Ghahari, L.N. Assi, A. Alsalman, K.E. Alyamaç, Fracture properties evaluation of cellulose nanocrystals cement paste, *Materials (Basel)*. 13 (2020). <https://doi.org/10.3390/ma13112507>.
- [22] Y. Cao, P. Zavattieri, J. Youngblood, R. Moon, J. Weiss, The relationship between cellulose nanocrystal dispersion and strength, *Constr. Build. Mater.* 119 (2016) 71–79. <https://doi.org/10.1016/j.conbuildmat.2016.03.077>.
- [23] E.G. Deze, E. Cuenca, A.M.L. Násner, M. Iakovlev, S. Sideri, A. Sapolidis, R.P. Borg, L. Ferrara, Nanocellulose enriched mortars: Evaluation of nanocellulose properties affecting microstructure, strength and development of mixing protocols, *Mater. Today Proc.* 54 (2021) 50–56.  
<https://doi.org/10.1016/j.matpr.2021.09.511>.
- [24] G. Long, Y. Li, C. Ma, Y. Xie, Y. Shi, Hydration kinetics of cement incorporating different nanoparticles at elevated temperatures, *Thermochim. Acta.* 664 (2018) 108–117. <https://doi.org/10.1016/j.tca.2018.04.017>.

- [25] K. Mei, Z. He, B. Yi, X. Lin, J. Wang, H. Wang, J. Liu, Study on electrochemical characteristics of reinforced concrete corrosion under the action of carbonation and chloride, *Case Stud. Constr. Mater.* 17 (2022) e01351. <https://doi.org/10.1016/j.cscm.2022.e01351>.
- [26] A. Kruk, D. Madej, A new approach to time-resolved electrochemical impedance spectroscopy using the Impedance Camera to track fast hydration processes in cement-based materials, *Meas. J. Int. Meas. Confed.* 205 (2022) 112199. <https://doi.org/10.1016/j.measurement.2022.112199>.
- [27] X.R. Nóvoa, Electrochemical aspects of the steel- concrete system. A review, *J. Solid State Electrochem.* 20 (2016) 2113–2125. <https://doi.org/10.1007/s10008-016-3238-z>.
- [28] R. Wang, F. He, C. Shi, D. Zhang, C. Chen, L. Dai, AC impedance spectroscopy of cement - based materials: measurement and interpretation, *Cem. Concr. Compos.* 131 (2022) 104591. <https://doi.org/10.1016/j.cemconcomp.2022.104591>.
- [29] B. Huang, J. Wang, G. Piukovics, N. Zabihi, J. Ye, M. Saafi, J. Ye, Hybrid cement composite-based sensor for in-situ chloride monitoring in concrete structures, *Sensors Actuators B Chem.* 385 (2023) 133638. <https://doi.org/10.1016/j.snb.2023.133638>.
- [30] Q. Liu, H. Tang, L. Chi, K. Chen, L. Zhang, C. Lu, Evolution of Electrochemical Impedance Spectra Characteristics of Cementitious Materials after Capturing Carbon Dioxide, *Sustainability.* 15 (2023) 2460.
- [31] S. Wang, J. Zhang, O. Gharbi, V. Vivier, M. Gao, M.E. Orazem, Electrochemical impedance spectroscopy, *Nat. Rev. Methods Prim.* 1 (2021). <https://doi.org/10.1038/s43586-021-00039-w>.
- [32] X. Hu, C. Shi, X. Liu, J. Zhang, G. De Schutter, A review on microstructural characterization of cement-based materials by AC impedance spectroscopy, *Cem. Concr. Compos.* 100 (2019) 1–14.
- [33] N. Elgrishi, K.J. Rountree, B.D. McCarthy, E.S. Rountree, T.T. Eisenhart, J.L. Dempsey, A Practical Beginner's Guide to Cyclic Voltammetry, *J. Chem. Educ.* 95 (2018) 197–206. <https://doi.org/10.1021/acs.jchemed.7b00361>.
- [34] H. Hasan, B. Huang, M. Saafi, J. Sun, Y. Chi, E. Whale, D. Hepworth, J. Ye, Novel engineered high performance sugar beetroot 2D nanoplatelet-cementitious composites, *Constr. Build. Mater.* 202 (2019) 546–562. <https://doi.org/10.1016/j.conbuildmat.2019.01.019>.
- [35] Y. Chi, B. Huang, M. Saafi, J. Ye, C. Lambert, Carrot-based covalently bonded saccharides as a new 2D material for healing defective calcium-silicate-hydrate in cement: Integrating atomistic computational simulation with experimental studies, *Compos. Part B Eng.* 199 (2020) 108235.
- [36] Y. Chi, B. Huang, M. Saafi, N. Fullwood, C. Lambert, E. Whale, D. Hepworth, J. Ye, 2D bio-based nanomaterial as a green route to amplify the formation of hydrate phases of cement composites: Atomistic simulations and analytical characterization, *Constr. Build. Mater.* 299 (2021) 123867. <https://doi.org/10.1016/j.conbuildmat.2021.123867>.

- [37] D. Hepworth, E. Whale, Cellulose platelet compositions, methods of preparing cellulose platelet compositions and products comprising same, US 9,834,664 B2, 2017.
- [38] P. Payakaniti, S. Pinitsoontorn, P. Thongbai, V. Amornkitbamrung, P. Chindaprasirt, Electrical conductivity and compressive strength of carbon fiber reinforced fly ash geopolymeric composites, *Constr. Build. Mater.* 135 (2017) 164–176.
- [39] İ. Şanal, N.Ö. Zihnioğlu, A. Hosseini, Particle image velocimetry (PIV) to evaluate fresh and hardened state properties of self compacting fiber-reinforced cementitious composites (SC-FRCCs), *Constr. Build. Mater.* 78 (2015) 450–463.
- [40] Y. Cao, N. Tian, D. Bahr, P.D. Zavattieri, J. Youngblood, R.J. Moon, J. Weiss, The influence of cellulose nanocrystals on the microstructure of cement paste, *Cem. Concr. Compos.* 74 (2016) 164–173. <https://doi.org/10.1016/j.cemconcomp.2016.09.008>.
- [41] F. Rajabipour, G. Sant, J. Weiss, Interactions between shrinkage reducing admixtures (SRA) and cement paste's pore solution, *Cem. Concr. Res.* 38 (2008) 606–615. <https://doi.org/10.1016/j.cemconres.2007.12.005>.
- [42] I. Pane, W. Hansen, Investigation of blended cement hydration by isothermal calorimetry and thermal analysis, *Cem. Concr. Res.* 35 (2005) 1155–1164. <https://doi.org/10.1016/j.cemconres.2004.10.027>.
- [43] A. ASTM, Standard test method for compressive strength of hydraulic cement mortars (using 2-in. or [50-mm] cube specimens), *Annu. B. ASTM Stand. B. ASTM Stand.* 4 (2013) 1–9.
- [44] C. ASTM, Standard test method for flexural strength of concrete (using simple beam with third-point loading), in: *Am. Soc. Test. Mater.*, 2010: pp. 12959–19428.
- [45] D. Ciolacu, F. Ciolacu, V.I. Popa, Amorphous cellulose—structure and characterization, *Cellul. Chem. Technol.* 45 (2011) 13.
- [46] H. Yang, R. Yan, H. Chen, D.H. Lee, C. Zheng, Characteristics of hemicellulose, cellulose and lignin pyrolysis, *Fuel.* 86 (2007) 1781–1788. <https://doi.org/10.1016/j.fuel.2006.12.013>.
- [47] H.M. Ng, L.T. Sin, T.T. Tee, S.T. Bee, D. Hui, C.Y. Low, A.R. Rahmat, Extraction of cellulose nanocrystals from plant sources for application as reinforcing agent in polymers, *Compos. Part B Eng.* 75 (2015) 176–200. <https://doi.org/10.1016/j.compositesb.2015.01.008>.
- [48] C.A. Guerrero-Fajardo, L. Giraldo, J.C. Moreno-Piraján, Preparation and characterization of graphene oxide for Pb(II) and Zn(II) ions adsorption from aqueous solution: Experimental, thermodynamic and kinetic study, *Nanomaterials.* 10 (2020). <https://doi.org/10.3390/nano10061022>.
- [49] A.I. Al-Hadithi, N.N. Hilal, The possibility of enhancing some properties of self-compacting concrete by adding waste plastic fibers, *J. Build. Eng.* 8 (2016) 20–28. <https://doi.org/10.1016/j.jobbe.2016.06.011>.

- [50] A. Alzaza, K. Ohenoja, V. Isteri, T. Hanein, D. Geddes, M. Poikelispää, M. Illikainen, Blending eco-efficient calcium sulfoaluminate belite ferrite cement to enhance the physico-mechanical properties of Portland cement paste cured in refrigerated and natural winter conditions, *Cem. Concr. Compos.* 129 (2022). <https://doi.org/10.1016/j.cemconcomp.2022.104469>.
- [51] F. Wang, X. Kong, L. Jiang, D. Wang, The acceleration mechanism of nano-C-S-H particles on OPC hydration, *Constr. Build. Mater.* 249 (2020) 118734. <https://doi.org/10.1016/j.conbuildmat.2020.118734>.
- [52] L. Yan, B. Kasal, L. Huang, A review of recent research on the use of cellulosic fibres, their fibre fabric reinforced cementitious, geo-polymer and polymer composites in civil engineering, *Compos. Part B Eng.* 92 (2016) 94–132. <https://doi.org/10.1016/j.compositesb.2016.02.002>.
- [53] J. Tao, N. Liu, L. Li, J. Su, Y. Gao, Hierarchical nanostructures of polypyrrole@MnO<sub>2</sub> composite electrodes for high performance solid-state asymmetric supercapacitors, *Nanoscale.* 6 (2014) 2922–2928. <https://doi.org/10.1039/c3nr05845j>.
- [54] R.F. Harrington, Introduction to electromagnetic engineering, Courier Corporation, 2003.
- [55] A. Shodiev, M. Chouchane, M. Gaberscek, O. Arcelus, J. Xu, H. Oularbi, J. Yu, J. Li, M. Morcrette, A.A. Franco, Deconvoluting the benefits of porosity distribution in layered electrodes on the electrochemical performance of Li-ion batteries, *Energy Storage Mater.* 47 (2022) 462–471. <https://doi.org/10.1016/j.ensm.2022.01.058>.
- [56] M. Nagao, K. Kobayashi, Y. Jin, I. Maruyama, T. Hibino, Ionic conductive and photocatalytic properties of cementitious materials: Calcium silicate hydrate and calcium aluminoferrite, *J. Mater. Chem. A.* 8 (2020) 15157–15166. <https://doi.org/10.1039/d0ta04866f>.
- [57] K.A. Snyder, X. Feng, B.D. Keen, T.O. Mason, Estimating the electrical conductivity of cement paste pore solutions from OH<sup>-</sup>, K<sup>+</sup> and Na<sup>+</sup> concentrations, *Cem. Concr. Res.* 33 (2003) 793–798. [https://doi.org/10.1016/S0008-8846\(02\)01068-2](https://doi.org/10.1016/S0008-8846(02)01068-2).
- [58] X. Xi, M. Ozturk, D.D.L. Chung, DC electric polarization of cured cement paste being unexpectedly hindered by free water, *J. Am. Ceram. Soc.* 105 (2022) 1074–1082. <https://doi.org/10.1111/jace.18121>.
- [59] S. Wen, D.D.L. Chung, Effect of admixtures on the dielectric constant of cement paste, *Cem. Concr. Res.* 31 (2001) 673–677. [https://doi.org/10.1016/S0008-8846\(01\)00475-6](https://doi.org/10.1016/S0008-8846(01)00475-6).
- [60] P. Krishnaveni, V. Ganesh, Electron transfer studies of a conventional redox probe in human sweat and saliva bio-mimicking conditions, *Sci. Rep.* 11 (2021) 1–13. <https://doi.org/10.1038/s41598-021-86866-z>.
- [61] E.P. Randviir, C.E. Banks, Electrochemical impedance spectroscopy: An overview of bioanalytical applications, *Anal. Methods.* 5 (2013) 1098–1115. <https://doi.org/10.1039/c3ay26476a>.

- [62] Y. Yang, R.A. Patel, S. V. Churakov, N.I. Prasianakis, G. Kosakowski, M. Wang, Multiscale modeling of ion diffusion in cement paste: electrical double layer effects, *Cem. Concr. Compos.* 96 (2019) 55–65. <https://doi.org/10.1016/j.cemconcomp.2018.11.008>.
- [63] D. Lau, W. Jian, Z. Yu, D. Hui, Nano-engineering of construction materials using molecular dynamics simulations: Prospects and challenges, *Compos. Part B Eng.* 143 (2018) 282–291. <https://doi.org/10.1016/j.compositesb.2018.01.014>.
- [64] H. Deng, Z. He, Interactions of sodium chloride solution and calcium silicate hydrate with different calcium to silicon ratios: A molecular dynamics study, *Constr. Build. Mater.* 268 (2021) 121067. <https://doi.org/10.1016/j.conbuildmat.2020.121067>.
- [65] W. Wang, P. Liu, M. Zhang, J. Hu, F. Xing, The Pore Structure of Phosphoaluminate Cement, *Open J. Compos. Mater.* 02 (2012) 104–112. <https://doi.org/10.4236/ojcm.2012.23012>.
- [66] J. Qin, F. Dai, H. Ma, X. Dai, Z. Li, X. Jia, J. Qian, Development and characterization of magnesium phosphate cement based ultra-high performance concrete, *Compos. Part B Eng.* 234 (2022) 109694. <https://doi.org/10.1016/j.compositesb.2022.109694>.
- [67] S. Wacharasindhu, S. Likitmaskul, L. Punnakanta, K. Chaichanwatanakul, K. Angsusingha, C. Tuchinda, REPORTING PHYSISORPTION DATA FOR GAS/SOLID SYSTEMS with Special Reference to the Determination of Surface Area and Porosity, *J. Med. Assoc. Thai.* 81 (1998) 420–430.
- [68] A. Anwar, B.S. Mohammed, M.A. Wahab, M.S. Liew, Enhanced properties of cementitious composite tailored with graphene oxide nanomaterial - A review, *Dev. Built Environ.* 1 (2020) 100002. <https://doi.org/10.1016/j.dibe.2019.100002>.
- [69] J. Tang, T. Yang, C. Yu, D. Hou, J. Liu, Precipitated calcium hydroxide morphology in nanoparticle suspensions: An experimental and molecular dynamics study, *Cem. Concr. Compos.* 94 (2018) 201–214. <https://doi.org/10.1016/j.cemconcomp.2018.09.004>.
- [70] I. Ismail, S.A. Bernal, J.L. Provis, S. Hamdan, J.S.J. Van Deventer, Drying-induced changes in the structure of alkali-activated pastes, *J. Mater. Sci.* 48 (2013) 3566–3577. <https://doi.org/10.1007/s10853-013-7152-9>.
- [71] D. Jansen, F. Goetz-Neunhoeffler, C. Stabler, J. Neubauer, A remastered external standard method applied to the quantification of early OPC hydration, *Cem. Concr. Res.* 41 (2011) 602–608. <https://doi.org/10.1016/j.cemconres.2011.03.004>.
- [72] S. Lv, Y. Ma, C. Qiu, T. Sun, J. Liu, Q. Zhou, Effect of graphene oxide nanosheets of microstructure and mechanical properties of cement composites, *Constr. Build. Mater.* 49 (2013) 121–127. <https://doi.org/10.1016/j.conbuildmat.2013.08.022>.
- [73] Q. Luo, Y.Y. Wu, W. Qiu, H. Huang, S. Pei, P. Lambert, D. Hui, Improving flexural strength of UHPC with sustainably synthesized graphene oxide, *Nanotechnol. Rev.* 10 (2021) 754–767. <https://doi.org/10.1515/ntrev-2021-0050>.

- [74] D. Hou, Z. Lu, X. Li, H. Ma, Z. Li, Reactive molecular dynamics and experimental study of graphene-cement composites: Structure, dynamics and reinforcement mechanisms, *Carbon N. Y.* 115 (2017) 188–208.

## Figure Captions

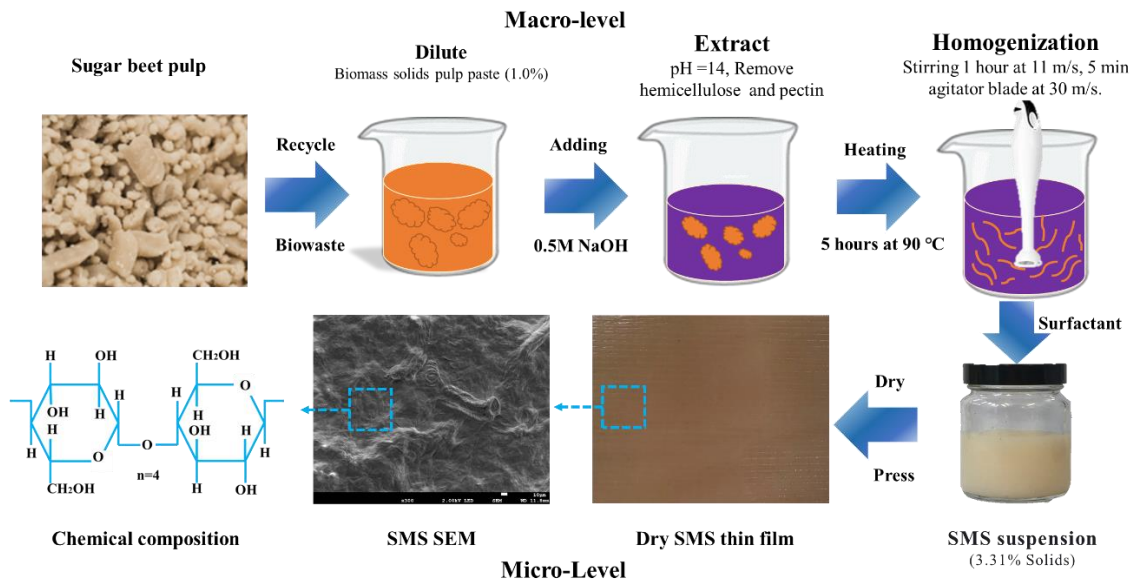


**Fig. 1.** Manufacturing process of the SMS sheets.

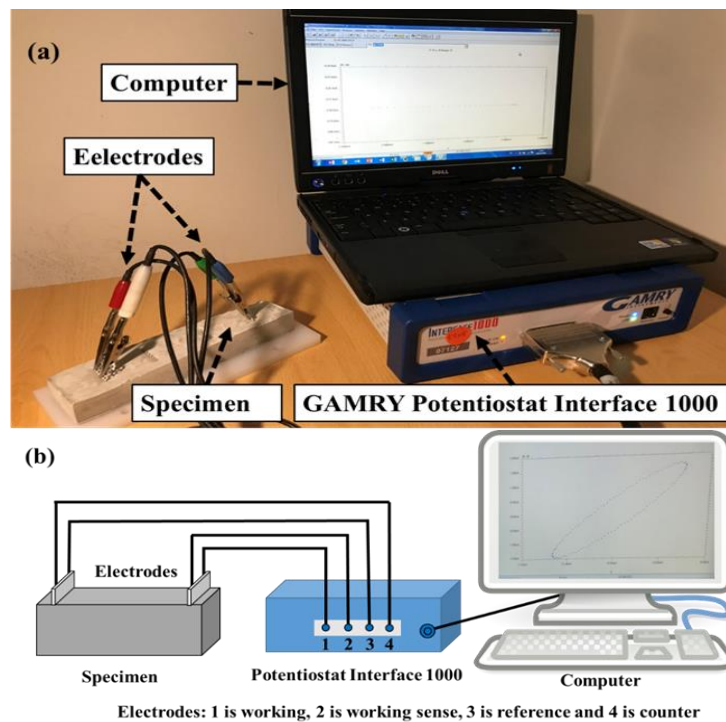


**Fig. 2.** Cyclic voltammetry and electrochemical impedance spectroscopy characterization.

(a) experiment setup, (b) schematic view of the setup.

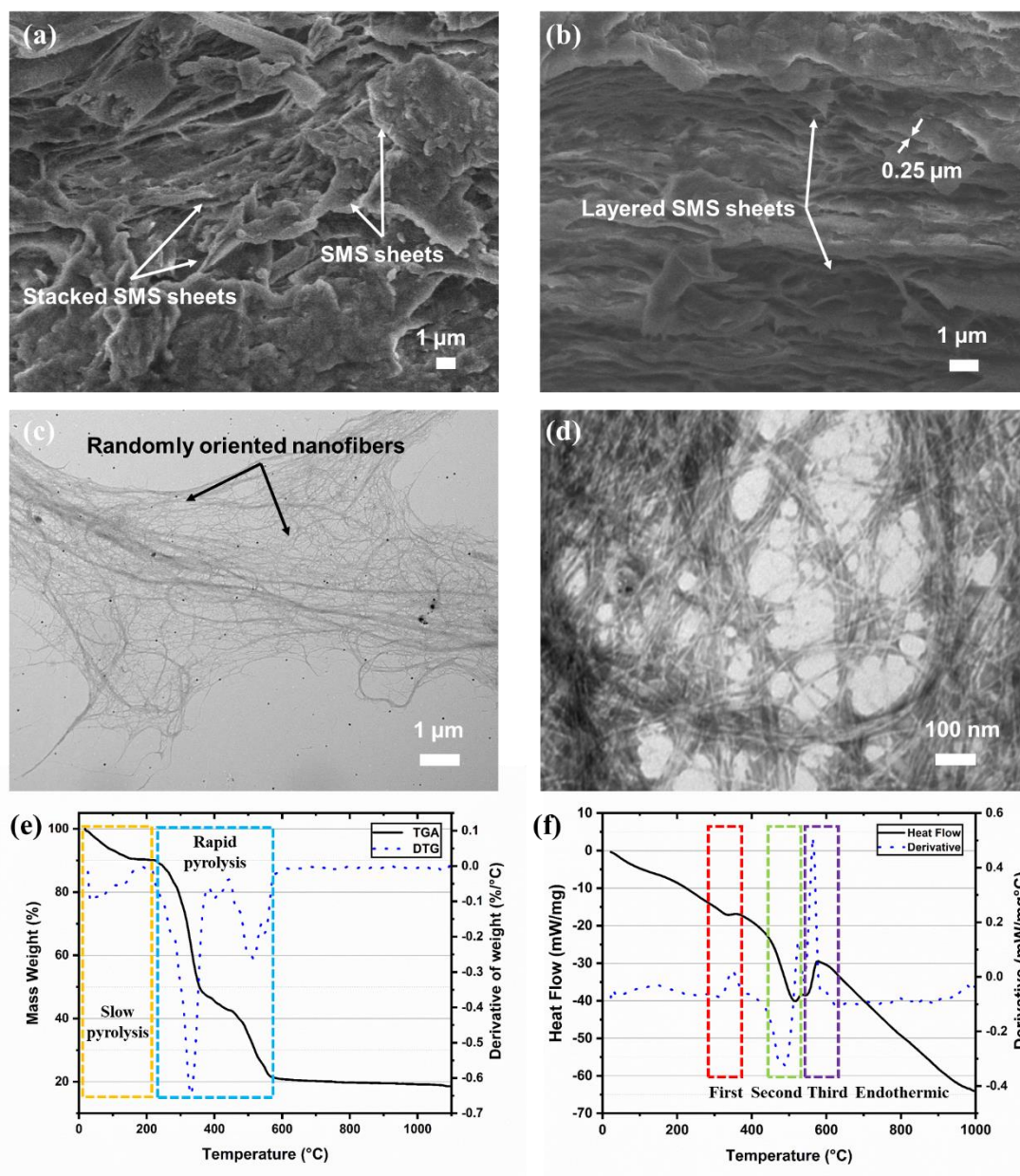


**Fig. 3.** Morphology and thermal properties of the SMS sheets. (a) surface morphology, (b) cross-section morphology, (c-d) TEM images, (e) TGA curve and its derivative, (f) DSC curve and its derivative.

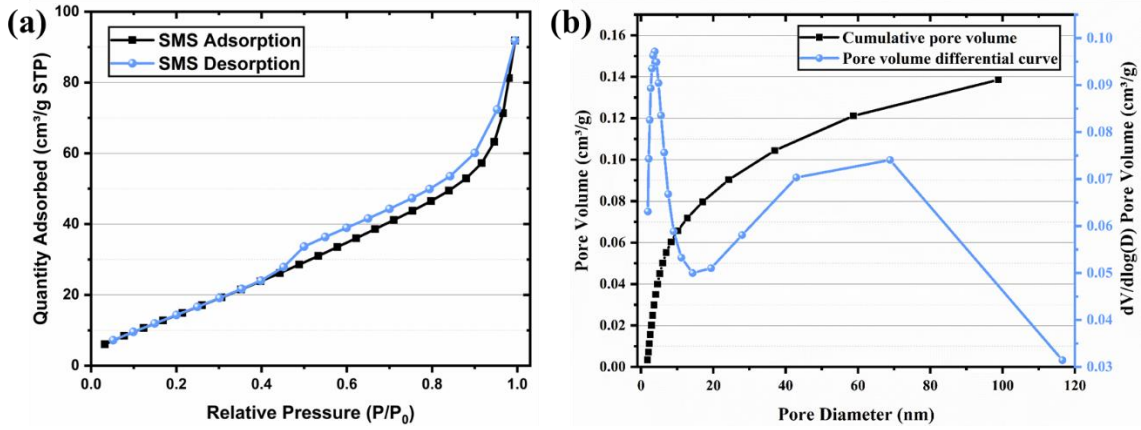


**Fig. 4.** Pore structure of SMS. (a) nitrogen sorption isotherm curves, (b) cumulative pore volume and pore distribution.

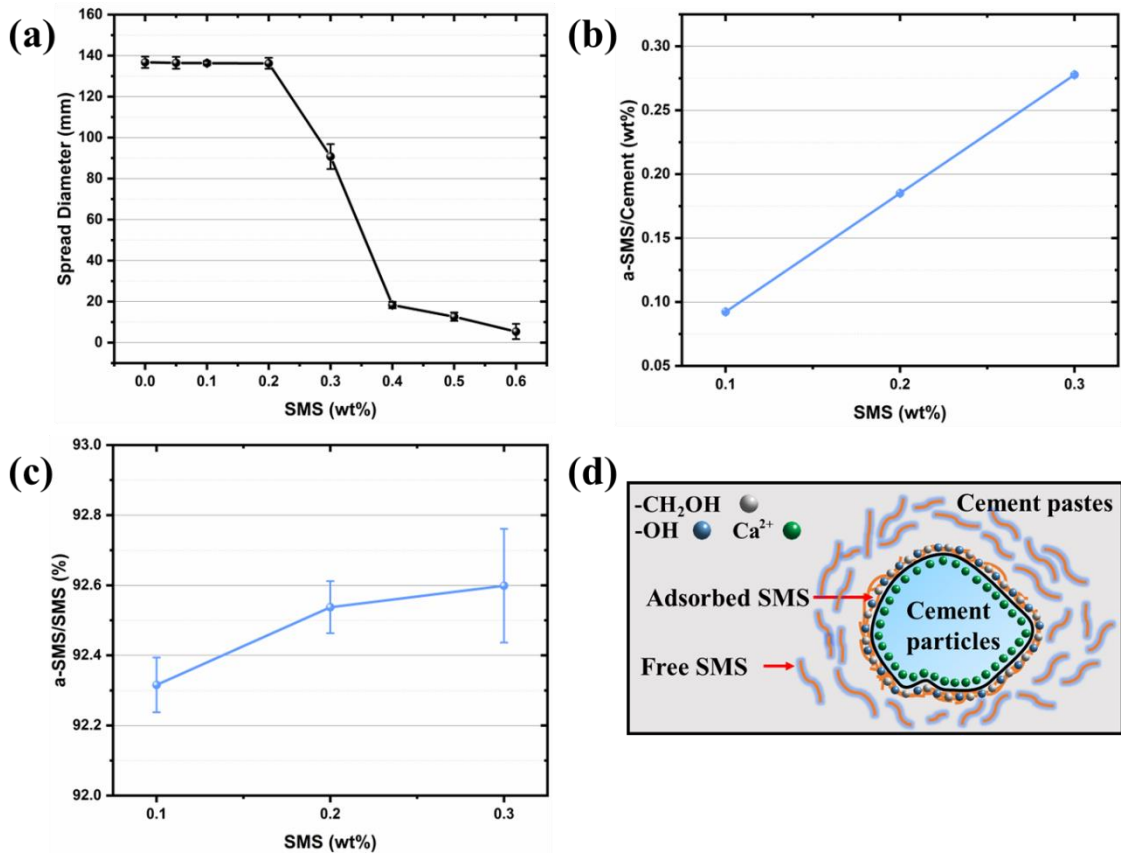


**Fig. 5.** Interaction of SMS with cement particles. (a) Mini-slump workability results, (b) per gram mass of a-SMS percentage out of cement, (c) per gram mass of a-SMS percentage out of SMS, (d) schematic of a-SMS and f-SMS in cement paste.

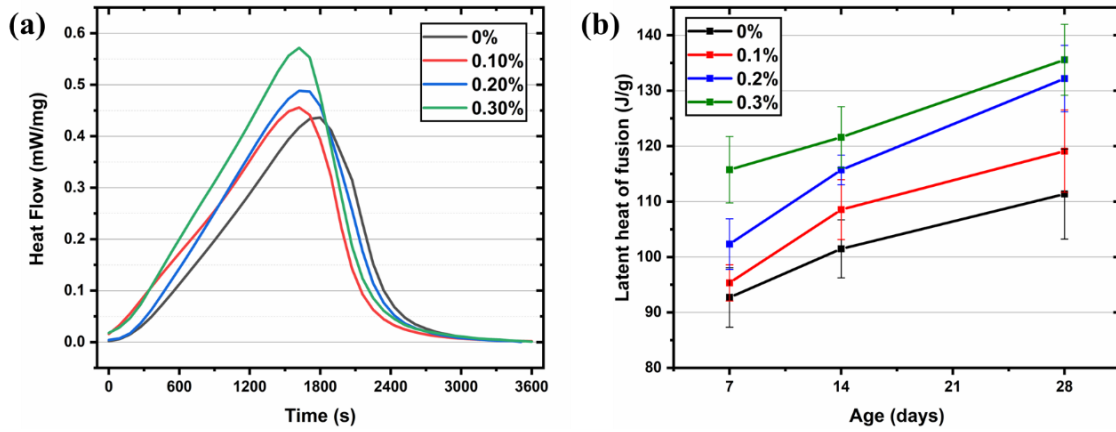


**Fig. 6.** Hydration heat of SMS-cementitious composites  $\text{Ca(OH)}_2$ . (a) effect of SMS on heat flow rate, (b) effect of curing age and SMS on latent heat of flow.

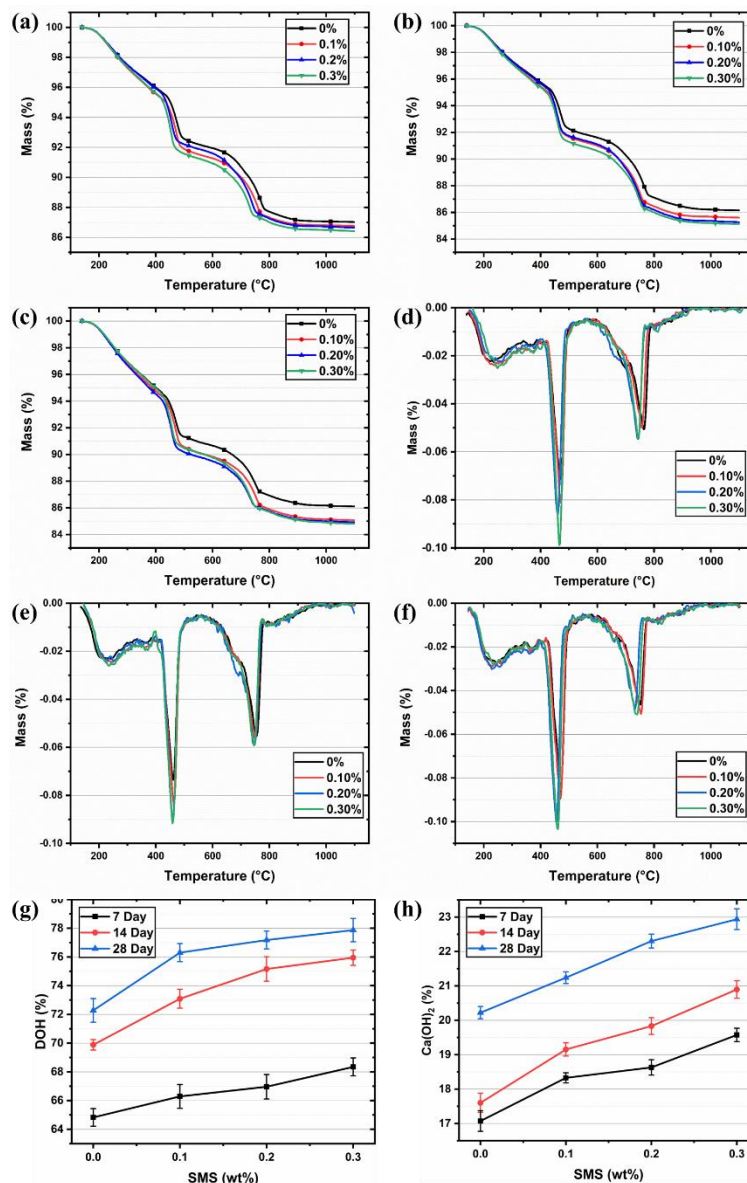


**Fig. 7.** Thermal behaviour of SMS-cementitious composites. (a) TGA curves at 7 days, (b) TGA curves at 14 days, (c) TGA curves at 28 days, (d) DTG curves at 7 days, (e) DTG curves at 14 days, (f) DTG curves at 28 days, (g) DOH content, (h)  $\text{Ca(OH)}_2$  content.

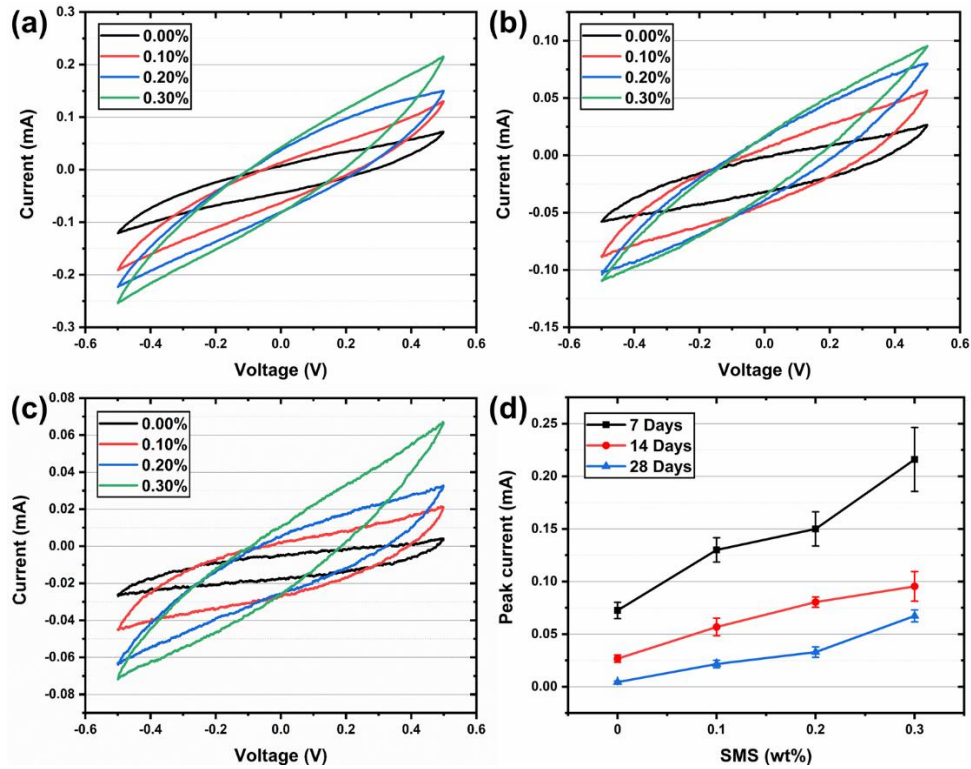


**Fig. 8.** CV-based electrochemical properties of SMS-cementitious composites. (a) CV curves at 7 days, (b) CV curves at 14 days, (c) CV curves at 28 days, (d) Peak current against SMS concentration.

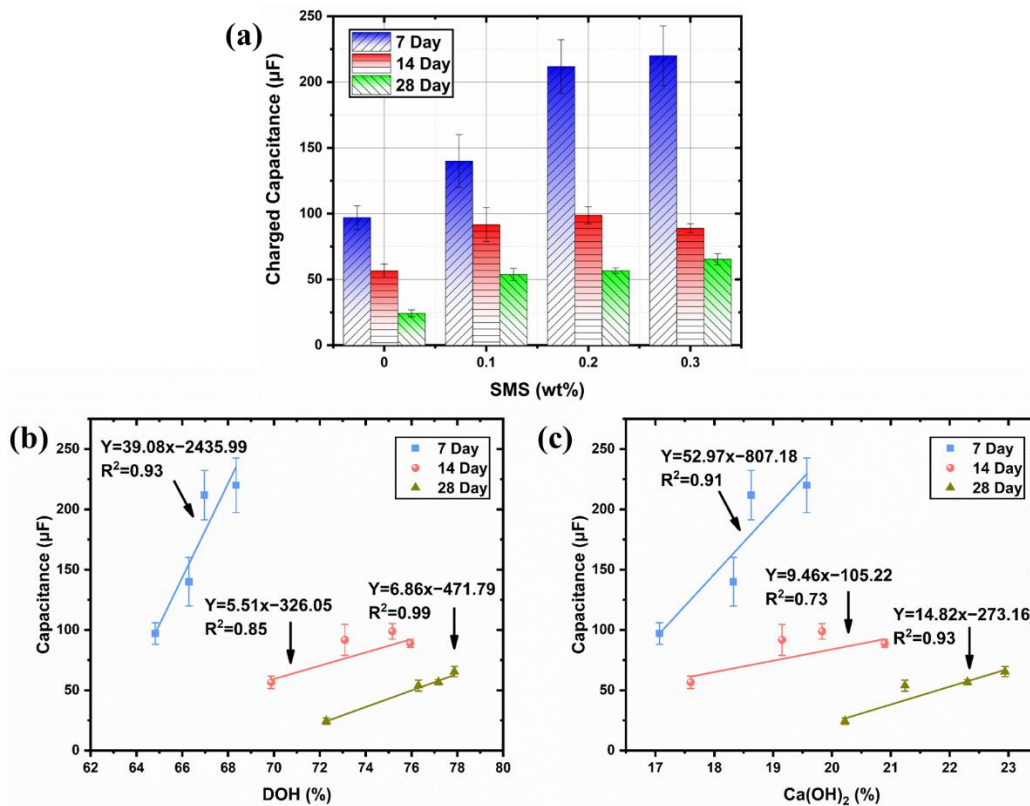


**Fig. 9.** Capacitance of the electrochemical SMS-cementitious composites. (a) capacitance against SMS concentration, (b) capacitance against DOH, (c) capacitance against  $\text{Ca(OH)}_2$  content.

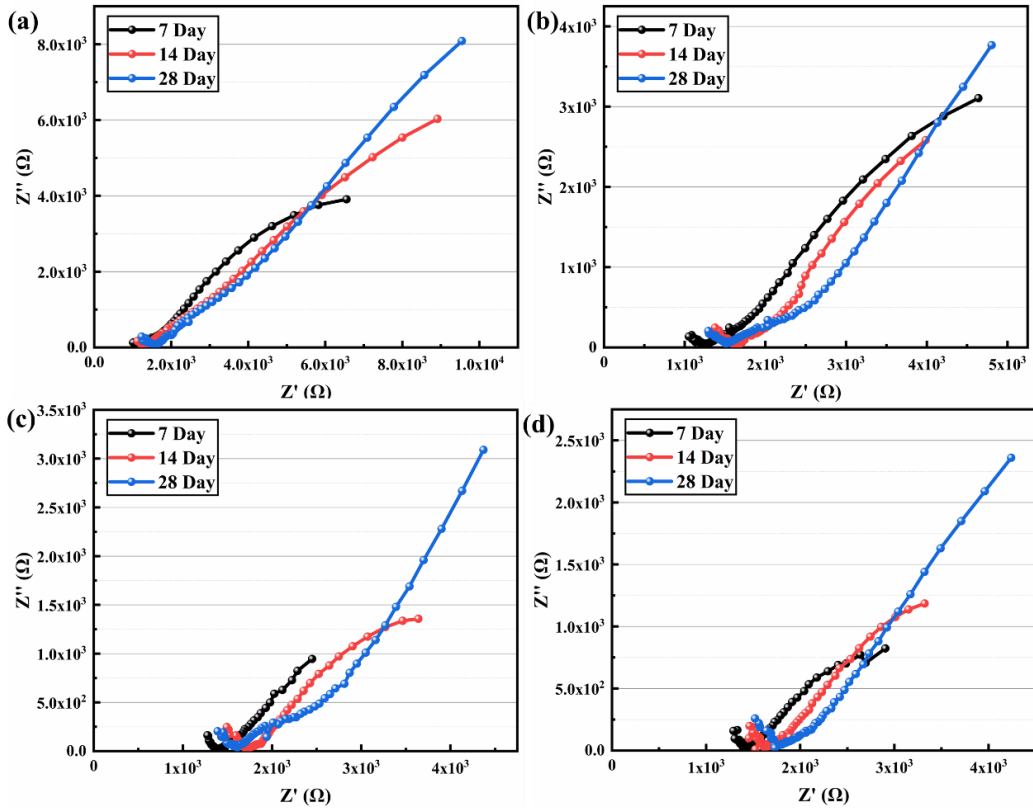


**Fig. 10.** Nyquist plots for the SMS-cementation composites at different curing ages. (a) paste with 0 wt%, (b) paste with 0.1 wt%, (c) paste with 0.2 wt%, (d) 0.3 wt%.

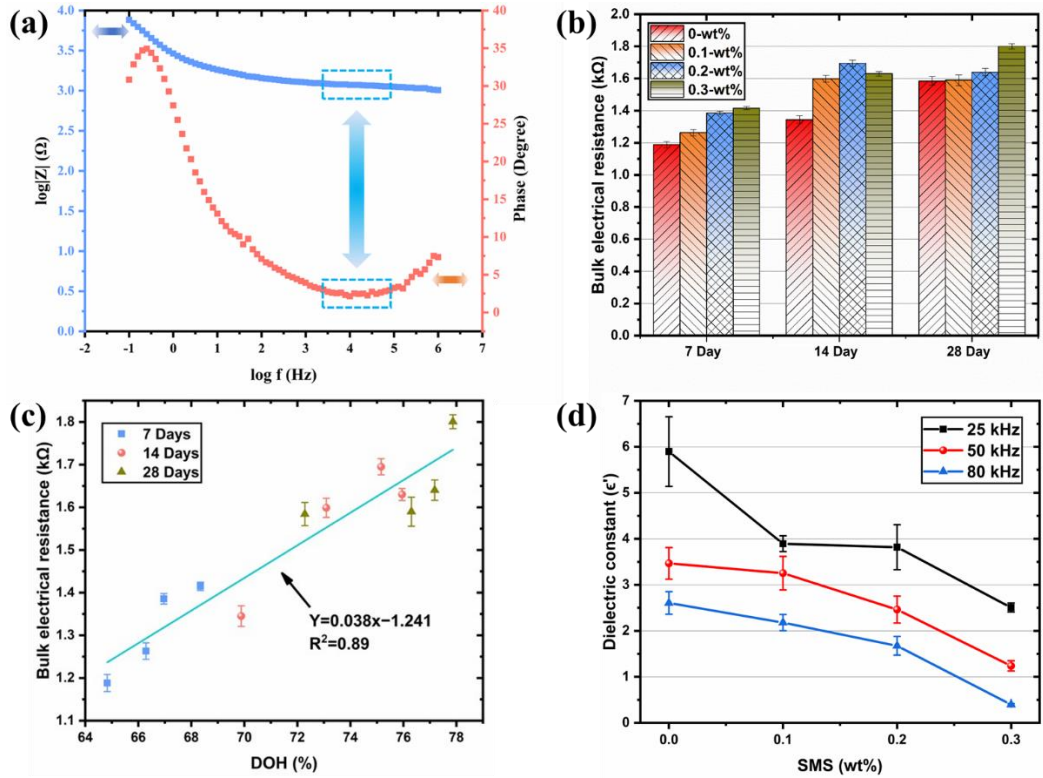


**Fig. 11.** EIS-based electrical properties of SMS-cementitious composites. (a) typical bode plot of impedance and phase for 0.1 wt% at 7 days, (b) bulk electrical resistance against curing age, (c) bulk electrical resistance against DOH at 7, 14 and 28 days, (d) dielectric constant against SMS concentration at 28 days.

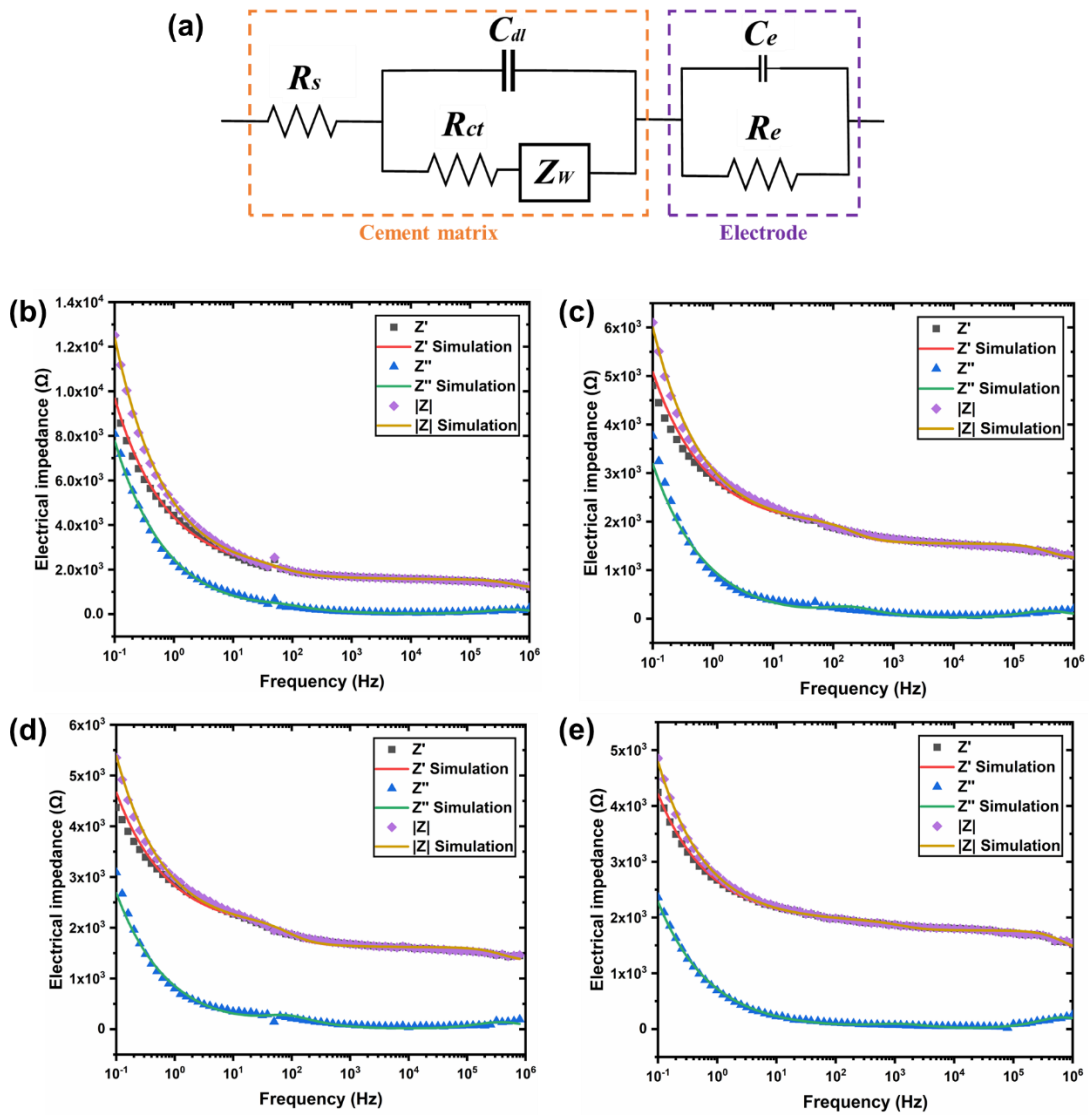


**Fig. 12.** Measured and fitted impedances of the cementitious composites at 28 days. (a) EC model, (b) 0% SMS, (c) 0.1-wt% SMS, (d) 0.2-wt% SMS, (e) 0.3-wt% SMS.

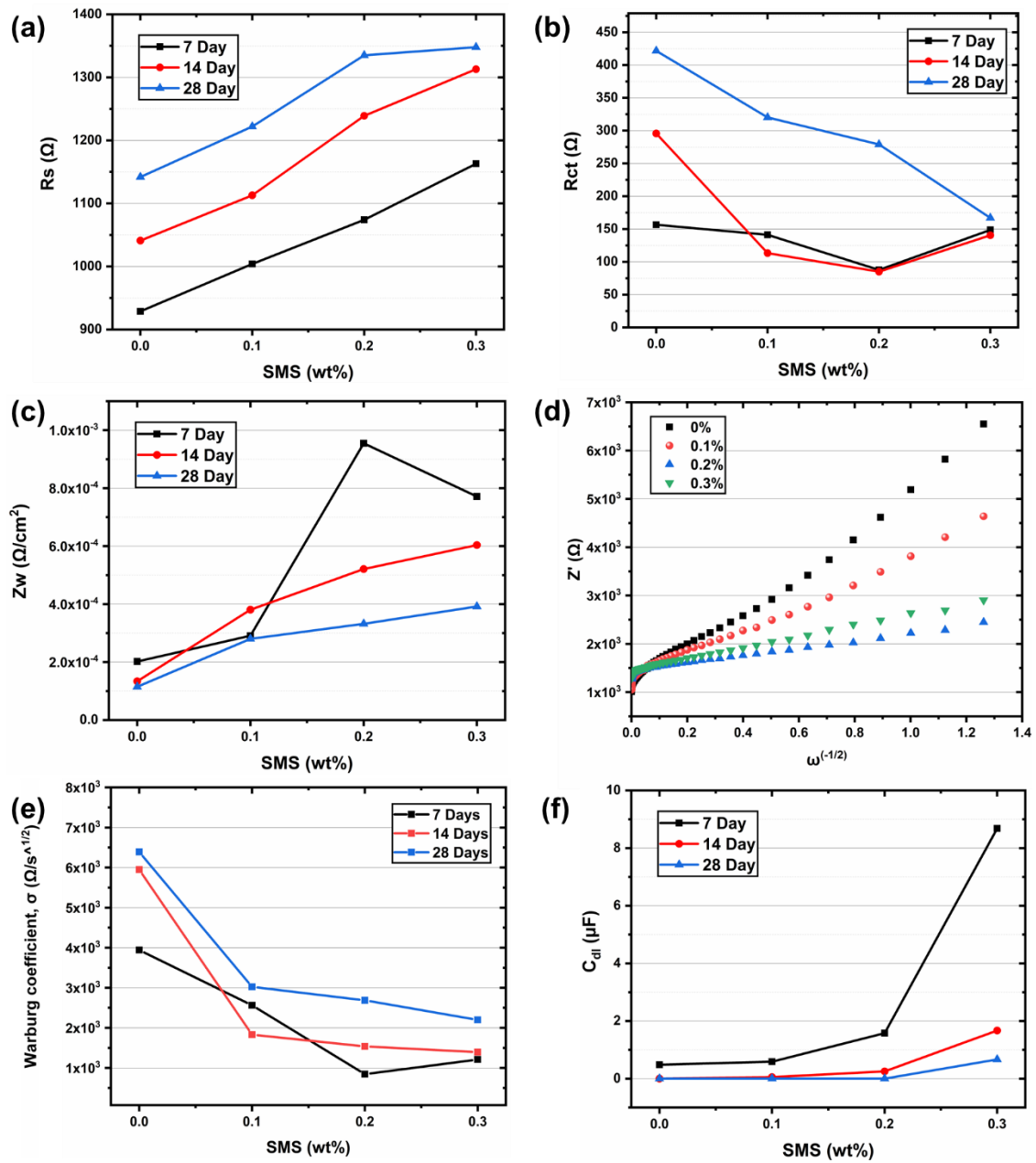


**Fig. 13.** EC parameter of the SMS-cementitious composites. (a) effect of SMS on  $R_s$ , (b) effect of SMS on  $R_{ct}$ , (c) effect of SMS on  $Z_w$ , (d) Warburg plots at 7 days, (e) Warburg coefficient against SMS concentration, (f) effect of SMS on  $C_{dl}$ .

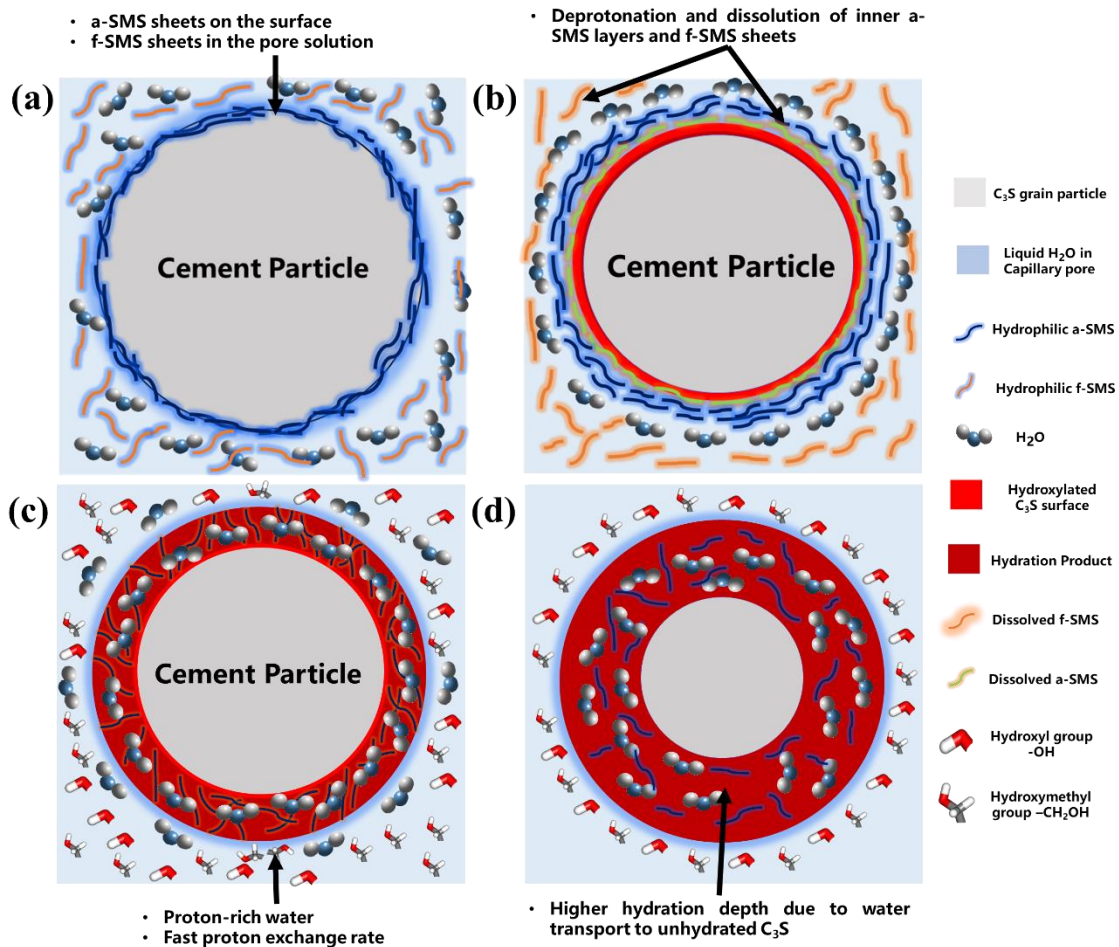


**Fig. 14.** Hydration kinetics of SMS-cementitious composites. (a) cement particle with a-SMS and f-SMS sheets in the pore solution, (b) breakage of H-bonds between (-OH/-CH<sub>2</sub>-OH) functional groups of SMS, and deprotonation and dissolution of the inner a-SMS layers, (c) formation of CH<sub>3</sub>OH and CH<sub>2</sub>H<sub>5</sub>OH, fast proton exchange and dissolution of C<sub>3</sub>S, (d) mechanism of water diffusion into the unhydrated C<sub>3</sub>S core and hydration growth.

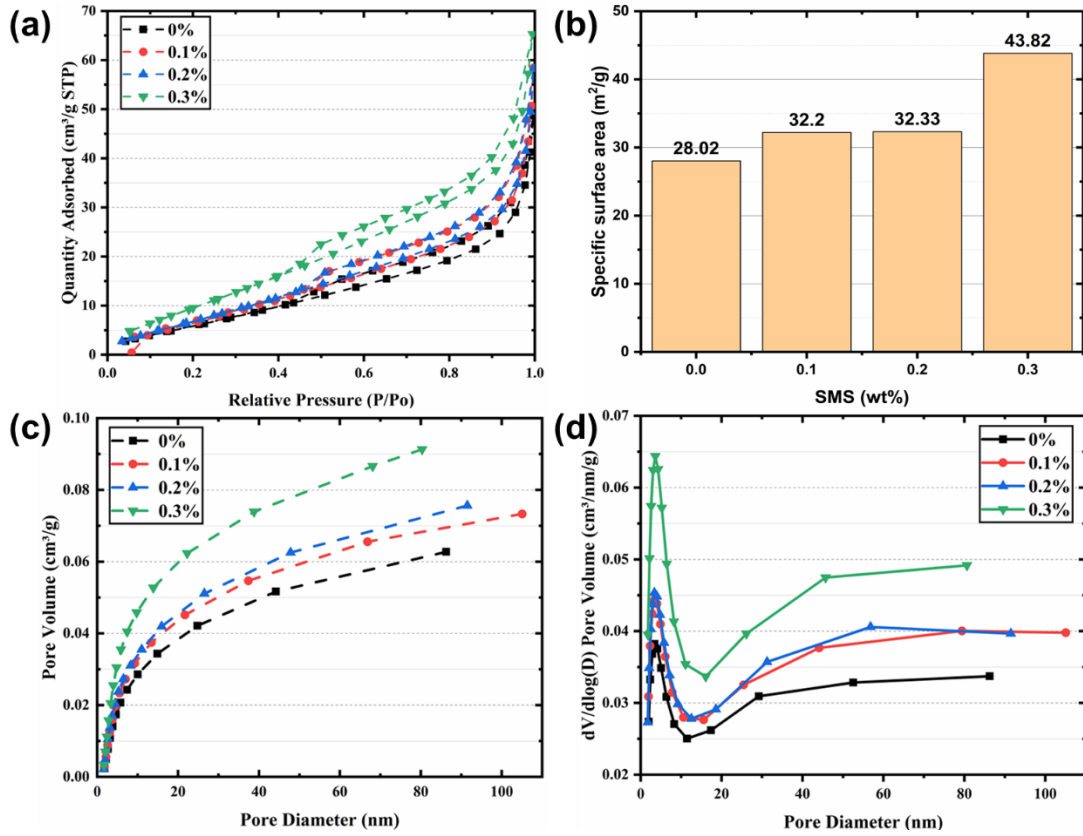


**Fig. 15.** Effect SMS on the porosity of the SMS-cementitious composites at 28 days. (a) BET isotherms, (b) specific surface area against SMS concentration, (c) cumulative pore volume against pore diameter, (d) pore size distribution.

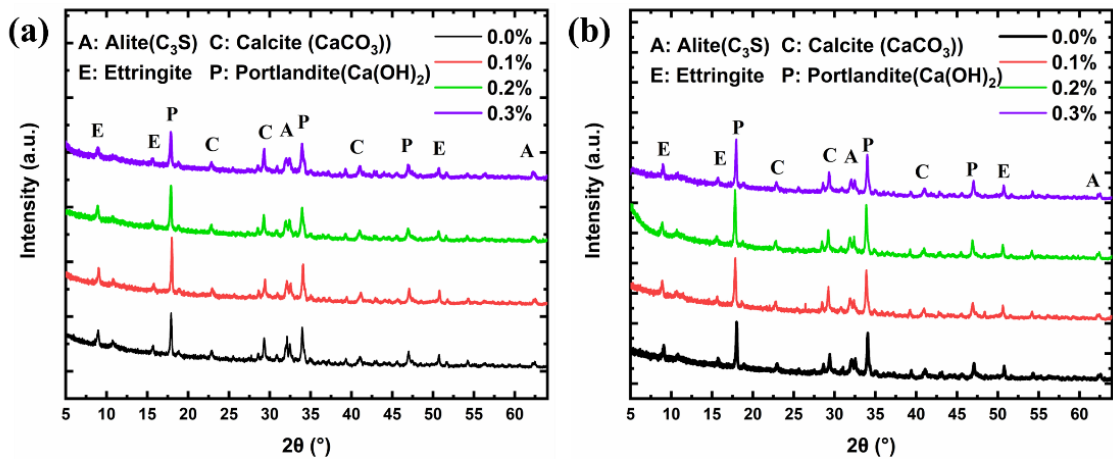


**Fig. 16.** XRD analysis ( $2\theta=5-65^\circ$ ) of cementitious composites with 0%, 0.1, 0.2 and 0.3-wt% amount of SMS at (a) 7 days, (b) 28 days.

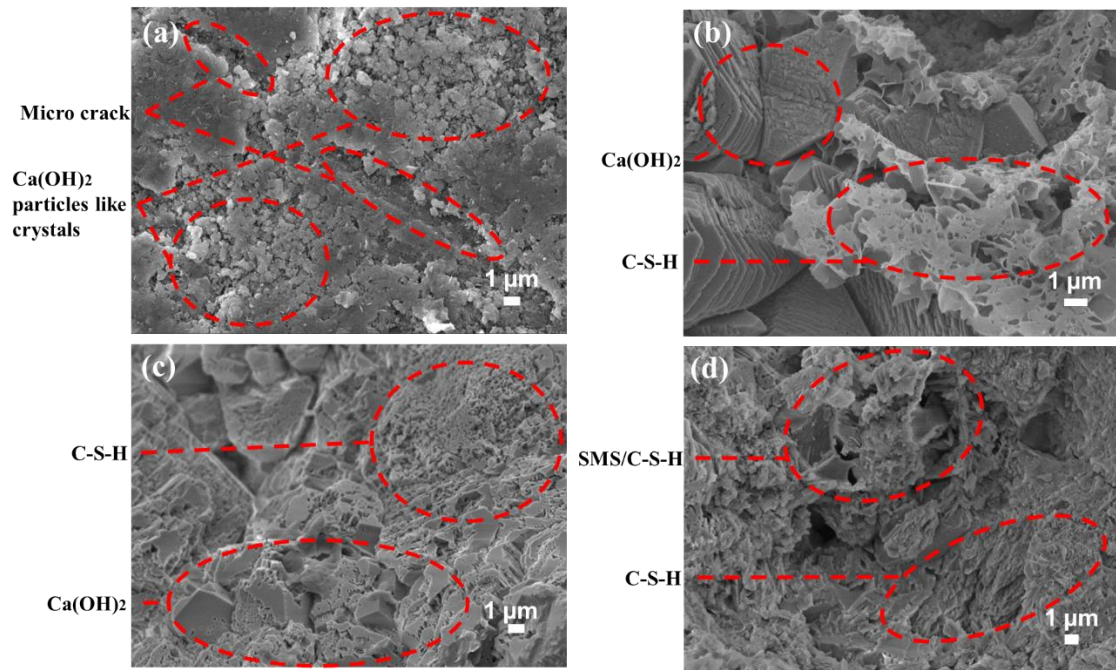


**Fig. 17.** SEM images of the SMS-cementitious composites at of 14 days (a) plain, (b) with 0.1wt%, (c) with 0.2 wt%, (d) with 0.3 wt%.

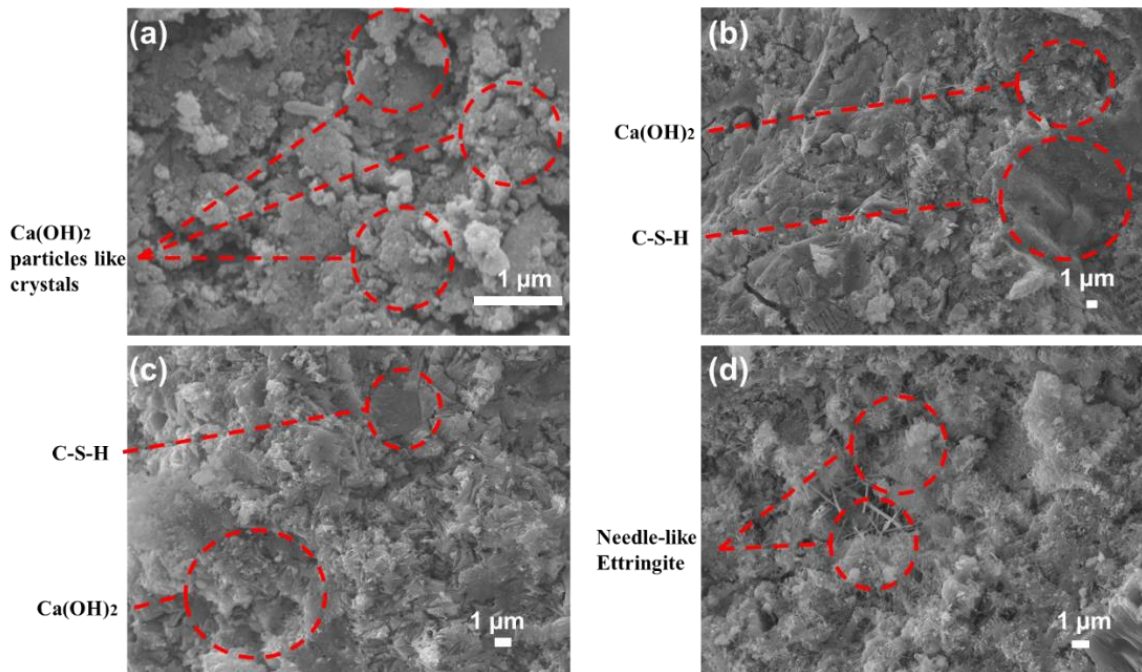


**Fig. 18.** SEM images of the SMS-cementitious composites at 28 days. (a) plain, (b) with 0.1 wt%, (c) with 0.2 wt%, (d) with 0.3 wt%.

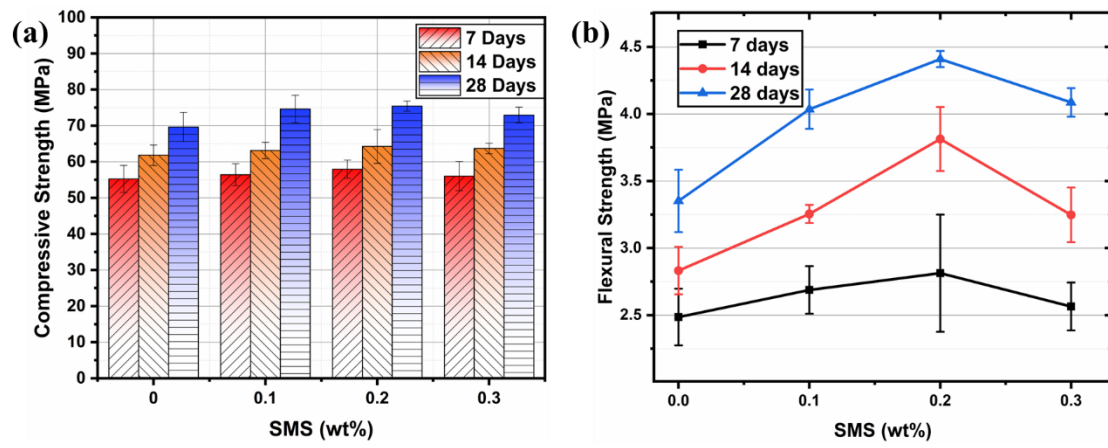


**Fig. 19.** SMS-cementitious composites at 7, 14 and 28 days. (a) Compressive strength, (b) flexural strength.

## Tables

Table 1: Fitting results for different SMS concentrations and curing ages

Day	SMS	$R_s$	$C_{dl}$	$R_{ct}$	$Z_w$	$C_e$	$R_e$
	(wt%)	( $\Omega$ )	( $\mu F$ )	( $\Omega$ )	( $\Omega/cm^2$ )	( $\mu F$ )	( $\Omega$ )
7	0	928.9	4.84E-01	156.5	2.02E-04	1.28E-03	231.6
	0.1	1004	5.92E-01	141.2	2.91E-04	1.58E-03	234.8
	0.2	1074	1.58	87.65	9.55E-04	4.70E-4	298.3
	0.3	1163	8.68	148.6	7.71E-04	7.53E-4	258.7
14	0	1041	1.30E-03	295.7	1.34E-04	7.42	337.4
	0.1	1113	5.39E-02	113.3	3.81E-04	3.22E-4	436.6
	0.2	1239	2.54E-01	84.95	5.21E-04	3.66E-4	439.1
	0.3	1313	1.67	140.5	6.04E-04	7.73E-4	306.9
28	0	1142	7.895E-04	421.7	1.148E-04	7.512	337.3
	0.1	1222	1.40E-03	320.2	2.800E-04	2.30	353.7
	0.2	1335	1.53E-03	279	3.320E-04	5.04	367.8
	0.3	1348	6.68E-01	166.9	3.920E-04	5.58E-4	421.6

**Declaration of interests**

The authors declare that they have no known competing financial interests or personal relationships that could have appeared to influence the work reported in this paper.

The authors declare the following financial interests/personal relationships which may be considered as potential competing interests: